

The Pennsylvania State University
The Graduate School

ARTIFICIAL MAGNETIC SYSTEMS IN 2 AND 3 DIMENSIONS

A Dissertation in
Physics
by
Susan Elizabeth Kempinger

© 2019 Susan Elizabeth Kempinger

Submitted in Partial Fulfillment
of the Requirements
for the Degree of

Doctor of Philosophy

August 2019

The dissertation of Susan Elizabeth Kempinger was reviewed and approved* by the following:

Nitin Samarth
Professor of Physics
Dissertation Advisor, Chair of Committee
George A. and Margaret M. Downsbrough Department Head

Vincent H. Crespi
Distinguished Professor of Physics, Materials Science and Engineering, and
Chemistry

Roman Engel-Herbert
Associate Professor of Materials Science and Engineering and Physics

Zhiqiang Mao
Professor of Physics

*Signatures are on file in the Graduate School.

Abstract

Artificial magnetic materials are powerful platforms for investigating properties of magnetic systems, in addition to having potential applications of their own. These types of systems can be designed with control and understanding over the interaction strength, disorder, and other properties that is difficult in naturally occurring materials. There are many ways to probe the behavior of artificial magnetic systems, including magneto-optical measurements for systems based on two-dimensional films and bulk magnetometry measurements for more complex three-dimensional structures. In this dissertation, we present a collection of studies on artificial magnetic materials.

First, we consider magnetic thin films patterned in the mesoscopic size regime from Pt/Co multilayers. We investigate the transition in these structures from continuous films that undergo domain wall nucleation and propagation to small dots that switch via seemingly instantaneous rotation. We find that as the feature size is decreased, so is the effective pinning field in the system. Qualitatively, the switching tends to increasingly favor the sample edges as the features are made smaller. The transition to single domain switching has an onset size of $2 \mu\text{m}$ and is complete by 500 nm .

Next, we consider arrays of perpendicular artificial spin ice designed from Pt/Co multilayers patterned into the single domain regime. These arrays can be patterned with or without frustration, in a number of lattice spacings to tune the interaction strength. We pattern multiple physical samples with different levels of disorder and find that to understand the correlation in the arrays we must take into account both the interaction strength and disorder present. We also find that while the macrostate is reproducible from run to run on the same lattice, the microstate is stochastic. We believe this might be due to thermal fluctuations in the lattice. These studies were carried out on arrays in a weakly interacting regime. We then increase the coupling between islands using a soft magnetic underlayer and observe the effect this has on the correlations in demagnetized and hysteretic states. We find that the soft underlayer approximately doubles the interaction strength, but in hysteresis measurements on frustrated arrays this effect is somewhat dampened.

Finally, we study a three dimensional artificial magnetic material called a magnetic metalattice. We first fabricate these systems from Ni and show that they are indeed nanoscale and fully interconnected magnetic systems. By annealing the samples we observe an exchange bias effect. We then fabricate similar systems from Pt and Pd. The nanoscale size regime of the samples leads to induced magnetism in the Pt and Pd. For Pt and some Pd samples, the observed effect is ferromagnetic. For other Pd samples, we also observe a superparamagnetic contribution to the magnetic signal. This could be due to incomplete infiltration or some more exotic effect.

Table of Contents

List of Figures	viii
List of Tables	xvii
Acknowledgments	xviii
Chapter 1	
Introduction	1
1.1 Motivation	1
1.1.1 Materials by Design	2
1.1.2 Artificial Magnetic Systems	4
1.1.3 Beyond Artificial Spin Ice	8
1.2 Magnetism	11
1.2.1 Paramagnetism	12
1.2.2 Ferromagnetism	12
1.2.3 Superparamagnetism	18
1.3 Materials	20
1.3.1 Pt/Co Multilayers	20
1.3.2 Permalloy	22
1.3.3 Nickel	23
1.3.4 Platinum and Palladium	25
Chapter 2	
Experimental Techniques	28
2.1 Sample Fabrication	28
2.1.1 Lithography	29
2.1.2 Thin Film Deposition	32
2.1.3 Metalattice Fabrication	33
2.2 Sample Characterization and Measurement	34
2.2.1 Scanning Electron Microscopy	34

2.2.2	Magnetometry Measurements	34
2.2.3	Magneto-Optical Microscopy	39
2.3	Computational Methods	45
2.3.1	Mesosopic Features	45
2.3.2	Find Locations and Datastreams	47
2.3.3	Adjustments for Py Underlayers	48
2.3.4	Hysteresis Analysis	49
2.3.5	Demagnetized Array Analysis	51
Chapter 3		
	Transition to Single Domain Structures	55
3.1	Introduction	55
3.2	Hysteresis	58
3.3	Domain Wall Propagation	61
Chapter 4		
	Perpendicular Artificial Spin Ice	67
4.1	Introduction	67
4.2	Stochasticity and Correlations in Hysteresis	67
4.2.1	Macroscopic degeneracy	69
4.2.2	Microstructure variation	77
4.3	Increasing the Interaction Strength	82
4.3.1	Magnetization in Py Layers	83
4.3.2	Demagnetized States	87
4.3.3	Quasi-Dynamic Data	96
Chapter 5		
	Magnetic Metalattices	100
5.1	Introduction	100
5.2	Nickel Metalattices	100
5.2.1	Hysteresis	102
5.2.2	Temperature Dependence	106
5.2.3	Exchange Bias	107
5.3	Platinum Metalattices	109
5.4	Palladium Metalattices	113
Appendix A		
	Details of Fabrication	121
A.1	Introduction	121
A.2	Lithography	121

A.3	Evaporation	126
A.4	Sputtering	127
Appendix B		
	Computational Documentation	128
B.1	Introduction	128
B.2	Location Finding and Datastream Generation	129
B.3	Hysteresis	131
B.4	Demag	134
B.5	Micromagnetics	134
	Bibliography	140

List of Figures

1.1	A flowchart showing the general approach to data-driven discovery and design of materials. Large databases of experimental materials properties with information on both microscopic quantities and relevant emergent properties are used to theoretically search for new materials that might display desired properties. Worthy targets for experimental work are identified. Then new experiments are carried out and experimental data are added to existing databases. Image reproduced from [2]	3
1.2	Left panel shows a representative figure of one possible ground state arrangement of water ice. White circles represent oxygen atoms and black circles represent hydrogen atoms, with short and long bonds colored in red and blue respectively. Right panel is an equivalent arrangement of spins in spin ice, with short bonds translated to inward pointing spins and long bonds translated to outward pointing spins. Based on figures from [16]	5
1.3	a) Schematic (left) and MFM image (right) of a square artificial spin ice array. The arrows in the schematic show the direction of the magnetization in the islands. In the MFM image, the magnetization of each island is visible as a pair of bright and dark spots, with the magnetization pointing from bright to dark. b) Schematic (left) and MFM (right) of a kagome artificial spin ice array. Figure reproduced from [18]	6

1.4	Left: Schematic of frustration in perpendicular system, with frustrated lattices designed based on these basic triangles. Right: Images of four different perpendicular geometries. The Hexagonal and Kagome geometries are imaged using MFM while the Square and Triangular geometries are imaged using MOKE. Square and Hexagonal geometries are not frustrated, while Triangular and Kagome are. One of the base triangles used to design these geometries is highlighted in red in each of the frustrated geometries presented. Image partially reproduced from [8]	8
1.5	Left: 3D rendering of the geometry of magnetic material infiltrated into a metalattice, with example tetrahedral sites (meta-atoms) and necks (meta-bonds) highlighted. Reproduced from [38]. Right: Cross-sectional view of an infiltrated metalattice, showing the sphere template in green, the infiltrated metal in grey, and the silica substrate in black. There is usually a thick layer of metal on top of the infiltrated template at the end of the infiltration process that is removed later. Figure is not to scale.	10
1.6	Magnetization showing curled domains in large periodicity samples and ordered domains in small periodicity samples, along with corresponding simulated hysteresis loops at different orientations and periodicities. Reproduced from [40]	11
1.7	Simplified schematic of the d band splitting near the Fermi level in Ni. Figure reproduced based on [39]	15
1.8	Example of hysteresis in a magnetic material. This data was taken on a Pt/Co multilayer film and is displayed with the magnetization normalized to the saturation magnetization.	16
1.9	SQUID measurement of magnetization vs. magnetic field in various Pt/Co multilayer samples. Solid lines are measured with the field perpendicular to the film plane. Dashed lines are measured with the field parallel to the film plane.	21
1.10	SQUID measurement of magnetization vs. magnetic field in a Py film. The dashed line was measured with the field oriented in the plane of the sample, and the solid line was measured with the field oriented perpendicular to the sample.	23
1.11	Left panel: I , $D(E_F)$, and $ID(E_F)$ for the first 50 elements, showing only Fe, Co, and Ni fulfill the Stoner criterion. Right: The density of states in Fe, Co, and Ni showing that each has a peak in the density of states at the Fermi Level. Graphic partially reproduced from [46] and [47]	24

1.12	Shape anisotropy in oblong nanoparticles. Analogous to the shape anisotropy that occurs in the more complicated metalattice geometry.	25
1.13	Periodic table with Ni, Pd, and Pt highlighted to show they have the same valence structure. Graphic taken from Wikipedia	25
1.14	The density of states in Pd, with the Fermi level highlighted in red, showing that the peak in the density of states is slightly removed from the Fermi Level. Graphic reproduced from [49] with emphasis added.	26
1.15	Top Left: Table showing values of magnetic moment as a function of lattice spacing. Reproduced from [50] Top Right: TEM image of a Pd nanoparticle showing a twin boundary, highlighted with the white line. Bottom: Hysteresis loops showing magnetism in Pt (left) and Pd (right) nanoparticles containing twin boundaries. Reproduced from [52] and [53]	27
2.1	A schematic of the lithography process used to fabricate patterned magnetic thin films. This procedure features a bilayer of (PMMA/P-MGI) as the resist, exposed using e-beam lithography, and developed with an undercut to prevent sidewall deposition. Produced based on figures from [55, 57]	31
2.2	Left panel: Schematic representation of film deposition using sputtering. Ar^+ ions are accelerated toward the target, freeing some atoms to deposit on to the substrate as a film. Right panel: Schematic representation of film deposition using evaporation. The material in the crucible is heated above the boiling point using an electron beam, and evaporated material redeposits on the substrate as a film.	33
2.3	Left: Second order gradiometer configuration of the MPMS detection coils. Right: Voltage response of SQUID detector when an ideal sample is moved through the detection coils. Reproduced from [60]	36
2.4	Left: Illustration of a sample mounted for measurement of magnetic response perpendicular to the film surface. Right: Illustration of a sample mounted for measurement of magnetic response parallel to the film surface.	38
2.5	A simplified schematic representation of the optical set up used for MOKE microscopy.	41
2.6	Photograph of the initial optical path of our microscopy set up. The yellow arrows show the path of the beam from the light source through the optics used to initialize the beam. The right image shows a clearer picture of the apertures and lens pairs used to reduce and collimate the beam.	42

2.7	Photograph of the MOKE microscopy set up after the initial polarizer. Image includes the objective lens, analyzing polarizer, CCD camera, and projected field magnet.	44
2.8	The first panel shows a background subtracted image of an isolated feature in a multi-domain state. The second panel shows the equivalent binary image, and the third shows the locations of the domain walls extracted from the binary image and overlaid on the original image.	46
2.9	Top panel: Hysteresis loops for target (blue) and comparison (red) islands offset so that the intensity at zero field is zero. Middle panel: Derivatives of the difference between the target and comparison islands, with one curve highlighted in blue for visual clarity. Bottom panel: The sum of the absolute value of the curves in the middle panel. This data was taken on an 800 nm spacing square array . . .	51
2.10	Normalized intensity as a function of field step for islands experiencing an oscillating demagnetization protocol. 100 islands out of an 800 nm lattice spacing square array are included in this graph. .	52
2.11	Histogram showing the averaged intensity of populations of up (red) and down (blue) islands in a demagnetized state of a square array. .	53
3.1	SEM images showing the lift-off quality and edge roughness profile of patterns square features with sizes of a) 10 μm b) 5 μm c) 3.75 μm d) 2 μm e) 1 μm and f) 0.5 μm	58
3.2	The change in the hysteresis of an ensemble of square magnetic features of different sizes a) 10 μm b) 5 μm c) 2 μm d) .5 μm for both the isolated features in each set (red) and the average of the entire field of view (blue). e) The magnetic switching behavior for arrays of different size features ranging from $s = 10 \mu\text{m}$ to 400 nm. f) Parameters from fitting the derivatives of the data shown in a-d to a Gaussian distribution.	60
3.3	The composite filling data at 25%, 50%, and 75% switched over a total of 50 runs for 2 μm , 3.75 μm , 5 μm and 10 μm features. White areas switched every run and black areas switched no runs, with blue scale between.	62

3.4	a) The instantaneous domain wall propagation information for $s = 10 \mu\text{m}$, $5 \mu\text{m}$, $3.75 \mu\text{m}$, and $2 \mu\text{m}$ features, at 30% filling and 70% filling, colored by feature size. b) The same data, artificially offset to show the difference in slope between the four sizes, and the similarity in slope within a particular size. c) The instantaneous domain wall propagation for the $10 \mu\text{m}$ sample, colored by area switched at the moment the velocity was calculated. The arrow represents the progression of increasing filling percent. d) The average effective pinning potential from linear fits to the velocity of different-sized features plotted against the reciprocal feature size	64
3.5	The average amount of the edge that has switched as a function of how much of the area has switched, for four different sizes of features. The arrow indicates the trend in edge switching as with decreasing feature size	65
4.1	SQUID measurement of magnetization vs. magnetic field for out-of-plane (solid lines) and in-plane (dashed lines) orientations for the samples presented in this dissertation	69
4.2	Top panel shows MOKE images recorded at 380 G in an increasing the field sweep, near the coercive field, for 500 nm lattice spacing square (left) and triangular (right) arrays from sample 2. The bottom panel shows normalized hysteresis loops recorded using imaging MOKE for these arrays with intensity averaged over the entire array area.	70
4.3	SEM images of samples 2 (left) and 5(right) showing the different edge profiles that might contribute to the different levels of disorder in these two samples.	71
4.4	a) Switching field distribution and associated Gaussian fits, with switching fields calculated by removing dipolar effects from 0 (as measured) to 5 nearest neighbors for a 500 nm square array (Sample 2). Width of the Gaussian fits for b) hexagonal, c) kagome, d) square, and e) triangular as a function of lattice spacing taking into account increasing numbers of neighbors. Fits to Eqn. 4.1 are shown as red lines, and disorder values from these fits are shown as black dashed lines. The inset images show a cartoon of the lattice geometry colored by target island (red) and neighbor number to match the colors on the graphs. A full set of neighbors is shown up to third nearest neighbor, along with a partial set of fourth and fifth nearest neighbors.	73

4.5	Top: The blue curve is a correction term for expected alignment at non-zero magnetization, and the red curve is the nearest neighbor alignment term for a 500 nm Squ array from sample 2. Dashed curve is a reflection of the solid red curve to show the asymmetry. Bottom: The subtraction of these two curves (C_S)	74
4.6	Plots of $C_S(\langle S \rangle)$ for various lattice spacings of a) square, and b) triangular arrays from sample 2, for increasing values of applied field. The dashed line in panel a shows $C_S(\langle S \rangle)$ as the field is decreased to more clearly illustrate the asymmetry. Panel c) shows the maximum value of correlation as a function of the dipolar field of an island on its nearest neighbor (i.e. the interaction strength) for samples 1 – 5. Panel d) shows the same data as a function of the dipolar field scaled by the measured disorder in the system.	75
4.7	Left: Correlation curve and associated functional fit from one run of a Squ 500 array. Right: Calculated derivatives for multiple lattice spacings of triangular arrays from sample 3.	76
4.8	Offsets calculated using the zeroes of the derivatives for left: unfrustrated and right: frustrated arrays from samples 1 – 3.	76
4.9	The switching field as a function of average switching field	78
4.10	Value of σ_h as a function of neighbor field for various lattice types on two samples	79
4.11	a) The covariance of switching fields between multiple runs for all three samples. b) The average overlap at the coercive field between pairs of runs for samples 2 and 3. Overlap is defined as the percent of islands that are in the same state in both states considered. c) The experimentally measured value of $C_S(0)$ (open squares) and the average value of $C_S(0)$ for randomly generated states with the experimentally measured overlap with the experimental state (solid squares), for a 500 nm square array from sample 3. The difference between these two curves is defined to be $\Delta C_S(0)$ d) The average difference in correlation between the experimentally measured state and a state with the experimentally measured average overlap. . . .	80
4.12	SEM of a sample with a Py layer deposited over an array of Pt/Co islands, showing the discontinuity of the Py layer deposited this way.	83
4.13	Percent of aligned bonds, proportional to the energy, in demagnetized patches of Pt/Co islands for a sample on Si, a sample with a Py overlayer, and a sample with a Py underlayer. The vertical dashed line denotes the ground state energy.	84
4.14	Cartoons showing simplified flux channeling between neighboring islands in anti-aligned states, a) without and b) with an external field.	85

4.15	Left: Relaxed states from micromagnetics simulations with islands aligned and anti-aligned with initial Py magnetization in the $-\hat{x}$ direction, for 500 nm (top) 650 nm (middle) and 800 nm (bottom) lattice spacing island pairs. Right: Relaxed states with initial Py magnetization in the $-\hat{y}$ direction.	87
4.16	The field an island experiences from it's nearest neighbor in the dipolar approximation, and in simulations with and without Py underlayers.	88
4.17	Correlation in samples 2 – 5 in demagnetized states showing agreement across all samples when considered as a function of both neighbor field and disorder in the system. Curves with solid lines correspond to unfrustrated geometries, and curves with dashed lines correspond to frustrated geometries. The dashed line at .33 represents the maximum correlation possible for a frustrated array and the solid line at 1 represents the maximum correlation possible for an unfrustrated array.	89
4.18	a) Correlation in 4, 4p, 5 and 5p showing the enhancement in correlation with a py underlayer b) showing agreement assuming a doubling of interaction strength	90
4.19	Image of demagnetized states for 500 nm lattice spacing square arrays from sample 4 (left) and 4p (right).	91
4.20	a) Correlation in 4, 4p, 5 and 5p showing the enhancement in correlation with a py underlayer b) showing agreement assuming a doubling of interaction strength	91
4.21	Image of demagnetized states in 500 nm lattice spacing Tri arrays from samples 4 (left) and 4p (right).	92
4.22	$C_{S,n}$ for $n = 1 - 7$ for square arrays from sample a) 5p and b) 5 and for triangular arrays from sample c) 4p and d) 4.	94
4.23	Left: A demagnetized state of a 500 nm lattice spacing triangular array, with arrows denoting slice directions used for directionally dependent Fourier transforms. Right: Fourier transforms taken in directions separated by 90° , showing a distinct asymmetry in ordering. The box highlights the frequency corresponding to twice the lattice spacing, where we expect a peak with antiferromagnetic ordering. Each curve corresponds to a different demagnetized state, confirming that this asymmetry is consistently present when the system is reinitialized into a new demagnetized state.	95

4.24	Directional Fourier Transforms in unfrustrated arrays (left: hex, right: squ) at 500 nm lattice spacing, for samples without (top) and with (bottom) Py underlayers. Each curve corresponds to a different demagnetized image.	96
4.25	Directional Fourier Transforms in frustrated arrays (left: kag, right: tri) at 500 nm lattice spacing, for samples without (top) and with (bottom) Py underlayers. Each curve corresponds to a different demagnetized image.	97
4.26	Left: Coercive field of arrays from samples 4 and 4p. Right: Width of switching field distributions for arrays from samples 4 and 4p. . .	98
4.27	Left: Maximum correlation during a hysteresis loop for unfrustrated arrays from samples 4, 4p, 5, and 5p. Right: Maximum correlation during a hysteresis loop for frustrated arrays from these samples. . .	98
5.1	TEM image of 30 nm (left) and 100 nm (right) infiltrated Ni metalattices, with yellow EDS highlighting the areas where Ni is present.	101
5.2	SQUID measurements of magnetization v. magnetic field from a) 30 nm and b) 100 nm samples in red and associated templates in blue, showing that the templates do not contribute significantly to the overall observed signal.	103
5.3	SQUID measurements of magnetization vs. magnetic field on Ni film (red, right axis) and metalattices (blue, left axis)	105
5.4	Temperature dependent magnetization after field cooling and zero field cooling a 30 nm Ni metalattice sample.	107
5.5	Left: TEM with EDS before (top) and after (bottom) annealing, showing that oxygen has migrated to be evenly dispersed and Ni oxide peaks appear in the diffraction after annealing. Right: 3 K hysteresis loops after cooling in a positive field before and after annealing.	108
5.6	Hysteresis data for Pt metalattices over a range of periodicities. The 30 nm Capped data is indicative of Pt film behavior, with contributions from the underlying metalattice appearing as low field artifacts in the data. All curves were measured at 3 K in the in-plane orientation.	111

5.7	Temperature dependence for Pt metalattice samples measured both using an FC (solid line) and ZFC (dashed line) initialization. Global offsets are removed such that the ZFC data starts at zero magnetization, and FC curves are offset by the same value. As we did not measure a ZFC curve on the capped 30 nm sample, this data is offset is estimated such that the FC data begins at roughly the same value as the other samples.	112
5.8	Hysteresis data for a 60 nm Pt metalattice sample taken at different temperatures ranging from 3 K to 300 K, showing little to no variation with temperature.	113
5.9	Low temperature hysteresis on Pd metalattices showing two distinct regimes of magnetic behavior. The right plot shows a 60 nm sample and continuous Pd film with behavior matching the Pt samples. The left plot shows various samples with higher squareness and sharper switching in the hysteresis.	115
5.10	Left: Hysteresis of sample 14c measured at a variety of temperatures. Right: Hysteresis of sample 14c at 300 K in red and 60c at 3 K in blue.	116
5.11	Temperature dependent hysteresis curves for 60 nm, 30 nm, and 14 nm metalattice samples. 60 nm and 30 nm samples use a diamagnetic background subtraction, and 14 nm sample uses the 300 K hysteresis as a background subtraction.	117
5.12	FC (red) and ZFC (blue) temperature curves for 60 nm (top), 30 nm (middle), and 14 nm (bottom) Pd metalattice samples.	118
5.13	TR curves for 60 nm (left) and 30 nm (right) Pd metalattice. Red is for the first round of increasing and decreasing temperature, yellow for the second, and so on.	119

List of Tables

4.1	Physical, magnetic, and statistical properties of five different artificial spin ice samples	69
5.1	Magnetic properties of a continuous Ni film, a 100 nm periodicity Ni metalattice, and a 30 nm periodicity Ni metalattice	104
5.2	Magnetic properties of Pt metalattices over a range of periodicities. Film data is measured on a capped 30 nm metalattice sample. All values are taken from data at 3 K.	111
5.3	Magnetic properties of Pd metalattices over a range of periodicities. H_C and M_R/M_S represent the low temperature, temperature dependent portion of the magnetization. $H_C, 2$ and $M_R/M_S, 2$ represent the temperature independent portion of the magnetization, measured at 300 K.	115

Acknowledgments

The work included in this dissertation has been the product of six years of learning and growth, and no such grand undertaking is possible without a wealth of community support and encouragement. It would be impossible to list by name every person who has helped me prepare for and succeed in graduate school. First and foremost I would like to thank my advisor, Prof. Nitin Samarth, for the invaluable guidance he has given me throughout my years at Penn State. He has consistently demonstrated what it means to have quality leadership skills and a deep appreciation for academia, and allowed me the freedom to pursue my scientific interests both in the laboratory and in the broader community. I would also like to thank the other faculty who have assisted in my education and research: Prof. Vin Crespi, Prof. John Badding, and Prof. Peter Schiffer (at Yale). Their experience and enthusiasm made this work possible.

My love for physics began during my undergraduate studies at the University of Nebraska-Lincoln, where I did several years of undergraduate research under the faculty advisement of Prof. Stephen Ducharme and the mentorship of Dr. Kristin Kraemer. They taught me how to work with equipment and set up an experiment, and gave me leeway to pursue my own scientific questions even as an undergraduate student. It was there that I also first became involved in outreach to younger scientists, which has been a central component of my career since then.

During my time at Penn State, I have had many wonderful colleagues. My mentor, Dr. Robbie Fraleigh, taught me how to design an experiment, how to stay positive when that design inevitably falls short, and how to balance a research career with a personal life. Members of my research group including Dr. Anthony Richardella, Dr. Dave Rench, Dr. Eric Kamp, Thomas Flanagan, Timothy Pillsbury and Jeff Rable have been there with encouraging conversations, willingness to exchange ideas, and help with experimental design. My other lab mates, my collaborators in the MRSEC, my collaborators at UIUC and Yale have all provided valuable input over the years. The undergraduate students I worked with through REU programs and through semesters (Alexis Bowers, Raina Crawford, Rosalie Terry and Sarah Abedi) were patient with me as I learned how to teach others to

carry out experiments. Finally, Jeff Rable and Yu-Sheng Huang have spent time and energy learning how to operate the SQUID and the MOKE systems so that experiments can continue.

My support system extends far beyond the physics department. I am grateful to my family, who encouraged my love of science and constant need to be involved in everything. My dear friends, who have consistently been there to remind me that I am human first and a scientist second, and supported me through all of the ups and downs of graduate school. Last but certainly not least, I am eternally grateful to my husband Jayson. He has been with me through it all, and makes me a better person. I can't wait to see where life takes us next.

Chapter 1 | Introduction

Note: sections of this chapter are taken from reference [1].

1.1 Motivation

Physics, as a scientific discipline, is rooted in a desire to understand how the world behaves. While the discipline began as an investigation of the material world as it naturally occurs, modern technology, from fabrication advances to computational techniques, allows us to go beyond nature-given materials. Using existing understanding as a starting point, scientists seek to design new materials with desirable properties. These new materials could be thin films created by strategically altering which atoms are present in existing compounds, novel nanostructured materials synthesized under extreme conditions, artificial systems of interacting elements created using lithography, or any number of other things. These disparate ideas are all connected by the underlying foundation that interesting materials can be designed rather than simply discovered.

We present in this dissertation a collection of studies on nanostructured magnetic materials. We begin with systems of two-dimensional patterned films with perpendicular magnetic anisotropy. It is well understood that small magnetic features will not energetically support domain walls, and can be used as components of artificial spin systems. However, the transition from continuous films to these small features has not been thoroughly experimentally investigated. First, we present a study on how the domain wall motion in perpendicular magnetic anisotropy films is affected by increasing the influence of boundaries by decreasing feature size. Then, we present an artificial spin system constructed of small features in the single

domain regime. We study the quasi-dynamic collective phenomena of this system, in particular seeking to understand the impact of disorder and stochasticity on the correlations in frustrated and non-frustrated arrays. We also present a method of increasing interactions between nanoscale elements, and the impact this increase has on the states achieved. Finally, we consider a three-dimensional nanostructured magnetic material known as a magnetic “metalattice”. Due to spatial confinement, these structures can be designed using natively ferromagnetic metals such as nickel, or metals that become ferromagnetic only in lower dimensions like platinum and palladium. The bulk magnetic response of these systems with respect to both magnetic field and temperature is considered.

1.1.1 Materials by Design

This work, leveraging the concept that interesting materials can be intentionally developed rather than discovered, exists within the field of “Materials by Design.” This field includes designing and synthesizing new materials, creatively combining existing materials, or building artificial systems to study and understand physical properties. To understand the historical and conceptual context of our artificial materials studies, it is beneficial to have an awareness of the materials by design framework. A canonical example of a materials by design project is the Materials Genome Initiative, working toward data-driven discovery and design of new materials. This multi-agency initiative was implemented for the purpose of both accelerating the process of discovering advanced materials, and significantly reducing the costs. The foundational approach of the materials genome initiative is a feedback loop, whereby known properties are used to predict potentially useful materials, those materials are synthesized and tested, and the new properties are added to the database of known properties [2,3]. Due to the amount of information necessary to make informed choices, advanced computational techniques such as machine learning are used to decide what compounds are worth studying (See Fig. 1.1). This process helps researchers make efficient choices about which materials to pursue in the laboratory. For this process to be effective, accurate descriptors are needed. Descriptors are functions connecting microscopic quantities (e.g. magnetic moment or band structure) to macroscopic properties (e.g. mobility or critical temperature). So, to design advanced materials, scientists need to understand the underlying

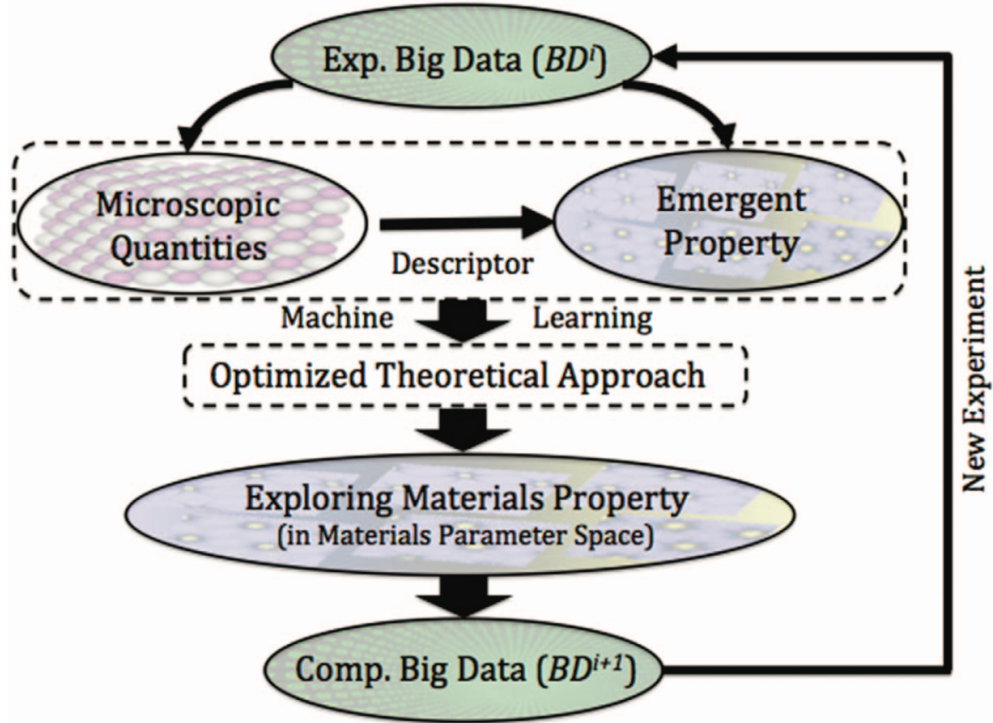


Figure 1.1. A flowchart showing the general approach to data-driven discovery and design of materials. Large databases of experimental materials properties with information on both microscopic quantities and relevant emergent properties are used to theoretically search for new materials that might display desired properties. Worthy targets for experimental work are identified. Then new experiments are carried out and experimental data are added to existing databases. Image reproduced from [2]

causes of emergent properties.

Emergent properties arise not only within a material but also from effects at boundaries [4]. Even at the interface of a material and air, atoms near surfaces have different environments than atoms in the interior. These different surface environments allow structural properties to change as materials are patterned into the nanoscale [3]. Additionally, materials properties can be tuned by placing different materials in contact with one another. To effectively design new materials, scientists need to understand not only the bulk behavior of a system but also the boundary behavior.

There are many potential approaches to the problem of understanding the relationship between microscopic properties and emergent phenomena. Some ap-

proaches center around designing new bulk materials with different microscopic properties to explore these relationships. However, designed materials needn't be constrained to be altered chemical formulas of existing lattices. Artificial metamaterials provide another gateway to understanding underlying causes of emergent phenomena, and can also be designed to be useful in and of themselves. Such artificially structured materials are the focus of the remainder of this dissertation.

1.1.2 Artificial Magnetic Systems

Artificially structured lattices have become increasingly popular platforms for studying complex collective phenomena in condensed matter, as they allow researchers to directly compare microscopic characteristics and associated macroscopic properties. Examples include artificial graphene [5], artificial skyrmion lattices [6], artificial spin ices [7–14].

Artificial spin ice, in particular, was developed to study frustrated systems. Frustration in physics occurs when a system is unable to simultaneously minimize all of its energy constraints. The study of this phenomena began with the investigation of water ice by Linus Pauling [15]. When water freezes into ice, each oxygen atom is surrounded by four hydrogen atoms in a tetrahedral arrangement. Two are covalently bonded to the oxygen with shorter bond lengths, and two are hydrogen bonded with longer bond lengths. There are multiple possible configurations of long and short bonds that are spatially distinct but energetically equivalent.

Magnetic atoms in rare earth pyrochlore lattices also have a tetrahedral arrangement [16]. The preferred states of these magnetic spins is a 2-in, 2-out configuration. Because this configuration is reminiscent of the arrangement of hydrogen atoms in water ice, these materials are referred to as spin ices. Much like water ice, there are multiple possible arrangements that meet the criteria for the lowest energy state in spin ice (See Fig. 1.2).

Spin ice materials are frustrated. For any given magnetic spin, the pairwise interaction energy with any of the other spins in the tetrahedron is minimized when the spins point oppositely (an “in” pointing spin favors “out” pointing neighbors and vice versa). However, because there are multiple pairwise interactions to be considered, the lowest overall energy is achieved when each tetrahedron has a 2-in, 2-out configuration, giving each spin two neighbors in the favorable state and one in

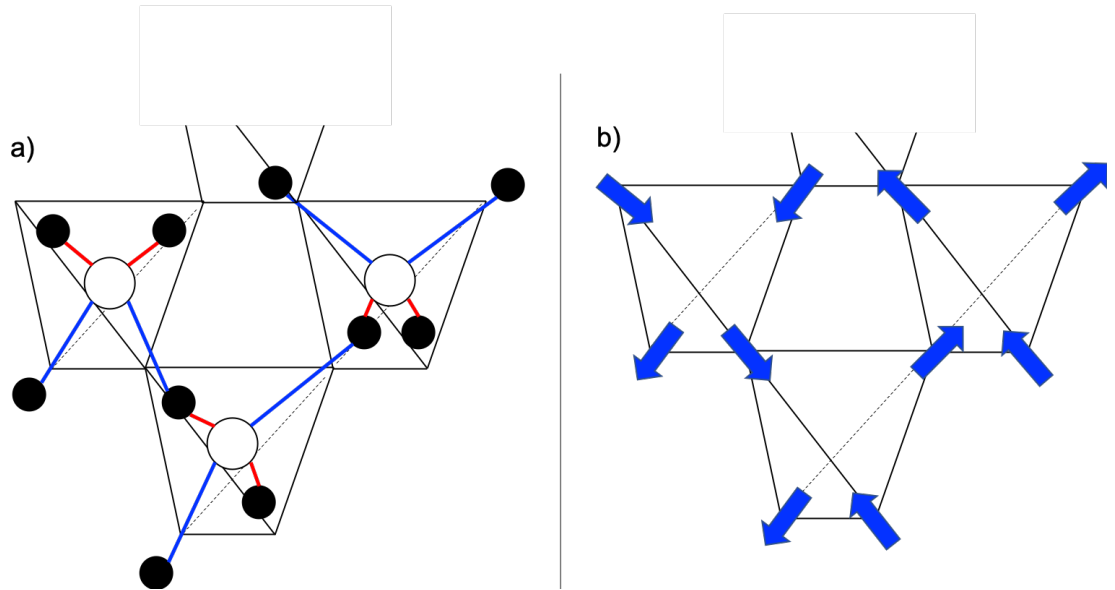


Figure 1.2. Left panel shows a representative figure of one possible ground state arrangement of water ice. White circles represent oxygen atoms and black circles represent hydrogen atoms, with short and long bonds colored in red and blue respectively. Right panel is an equivalent arrangement of spins in spin ice, with short bonds translated to inward pointing spins and long bonds translated to outward pointing spins. Based on figures from [16]

the unfavorable state. Thus the ground state does not simultaneously minimize the energy of all pairwise interactions. States that obey this 2-in, 2-out configuration are said to follow the “ice rule”. Because which interactions are favorable and which are unfavorable can be somewhat randomly assigned, there is a large degeneracy in the ground state of these materials. Experimentally, this leads to unique properties such as non-vanishing entropy even as the system approaches zero temperature.

Scientists at Penn State, in an attempt to find an alternate way to study the properties of this type of system, devised an “artificial” system with the same topological properties [7]. Artificial lattices are useful because they allow systematic engineering and tuning of properties such as interaction strengths and various types of defects to a degree far exceeding what is possible with naturally occurring crystalline lattices. Artificial spin ice consists of lithographically patterned, stadium-shaped magnetic islands arranged in a square lattice (See Fig. 1.3a), where each four island vertex finds its minimum energy state by having two islands pointing in and two islands pointing out. Each vertex is reminiscent of a tetrahedron in the three-dimensional spin ice system described previously. In initial experiments these

arrays were observed to follow the 2-in, 2-out ice rule. However, because this is a two-dimensional system, the degeneracy found in the three-dimensional system is lifted because the interaction is not identical between all four islands in the vertex. Initial experiments followed the ice rule because they failed to completely thermalize the system. Studies of as-grown states [17] and later demagnetization protocols using thermal annealing rather than demagnetization with a magnetic field were able to reach the ground state of square artificial spin ice [18]. Scientists subsequently developed a truly frustrated geometry of artificial spin ice in the kagome lattice (Fig. 1.3c) [19,20]. Recent work has also attempted to reinstate the degeneracy in the square geometry by raising one sublattice of the square ice and thus tuning the neighbor interactions [21].

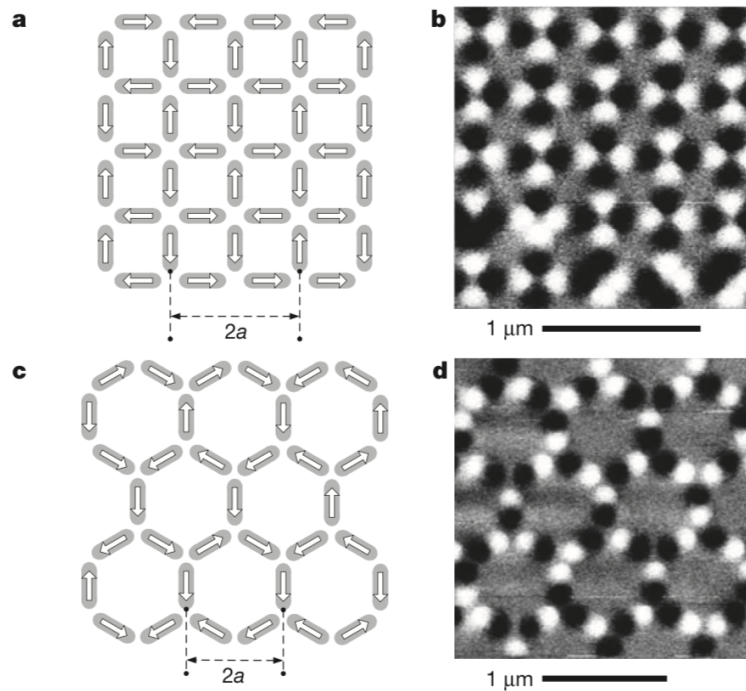


Figure 1.3. a) Schematic (left) and MFM image (right) of a square artificial spin ice array. The arrows in the schematic show the direction of the magnetization in the islands. In the MFM image, the magnetization of each island is visible as a pair of bright and dark spots, with the magnetization pointing from bright to dark. b) Schematic (left) and MFM (right) of a kagome artificial spin ice array. Figure reproduced from [18]

Artificial spin ice has been studied using magnetic force microscopy (MFM) to image demagnetized or meta-stable states and x-ray magnetic circular dichroism

photo-emission electron microscopy (XMCD-PEEM) to visualize states in an external field or with respect to temperature. Magneto-optical Kerr effect (MOKE) microscopy has been used to study overall properties but has not resolved the microstate present in artificial spin ice. Micromagnetic and other simulations have also been useful tools in understanding the behavior of these systems. Studies of artificial spin ice have led to the observation of magnetic monopoles and Dirac strings in well-controlled frustrated geometries [20–24] and they have also allowed access to the effects of thermal fluctuations [25, 26] and disorder [27, 28]. As the field of artificial spin ice has developed, new geometries have emerged. Vertex frustration, in which each individual vertex is not frustrated but a collection of vertices cannot reach the ground state due to geometrical constraints, have provided new avenues to study order and disorder [29]. Topological frustration, where a defect is introduced into an otherwise ordered lattice and nucleates far-reaching domain walls, has allowed studies on how defects might be accommodated into real lattices [30]. Geometries in which the patterned islands are connected rather than discrete elements introduce an additional component of domain wall dynamics into artificial spin ice and are studied using electrical transport measurements [31]. The creativity of artificial spin systems is in some ways only limited by the imagination of the researcher.

Perpendicular artificial spin ice systems [8, 32] are particularly propitious in this context because polar MOKE microscopy allows complete *in situ* imaging of microstates and their evolution as an applied field is varied [33]. Perpendicular artificial spin ice systems were first reported in 2012, and are distinct from in-plane artificial spin ice systems in that each constituent island is isotropically coupled to all other islands in an array. The interaction is dependent only on the distance between islands rather than the direction, which simplifies the system theoretically. Perpendicular islands arranged into arrays form a well-defined Ising system. Frustration in these systems is achieved in a different way than the in-plane artificial spin ice systems. Frustrated geometries are designed based on triangles. Due to the dipolar coupling between neighbors, islands prefer to be anti-aligned, or antiferromagnetically coupled. However, given a triangular arrangement of islands, if one island in the triangle points up and another points down, there is no way for the third island to minimize its energy constraints with respect to both of these neighbors. See Fig. 1.4 for a schematic of this type of frustration, as well

as images of magnetization in various perpendicular systems. Original studies on perpendicular artificial spin ice were conducted using MFM, and additional work has been carried out using MOKE microscopy. In this dissertation, we are particularly interested in the quasi-dynamic behavior of perpendicular artificial spin ice: how these systems undergo switching processes and the effect of disorder on correlations. We are also interested in ways to increase the interaction strength to more fully understand the impact of frustration on perpendicular systems.

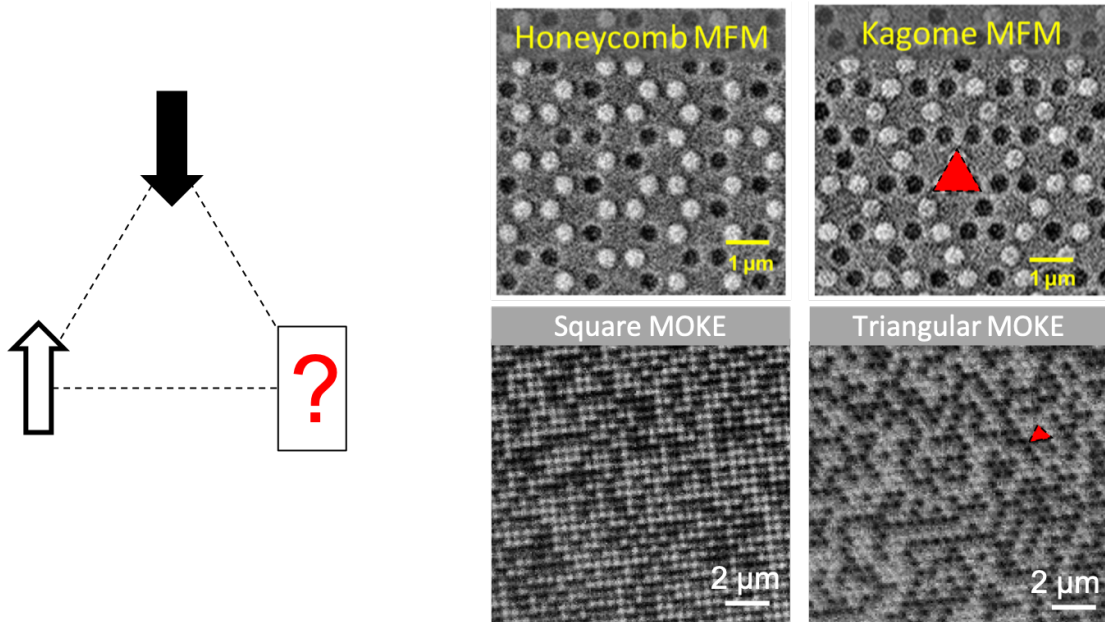


Figure 1.4. Left: Schematic of frustration in perpendicular system, with frustrated lattices designed based on these basic triangles. Right: Images of four different perpendicular geometries. The Hexagonal and Kagome geometries are imaged using MFM while the Square and Triangular geometries are imaged using MOKE. Square and Hexagonal geometries are not frustrated, while Triangular and Kagome are. One of the base triangles used to design these geometries is highlighted in red in each of the frustrated geometries presented. Image partially reproduced from [8]

1.1.3 Beyond Artificial Spin Ice

There is no fundamental reason that artificial systems need be constrained to two dimensions. There are additional challenges but also benefits to extending artificial materials to the third dimension. Experiments creating artificial materials by 3D polymer nanoprinting using two-photon lithography combined with metallic

deposition have been used to create a direct analog to artificial spin ice in three dimensions [34]. Another technique for creating three-dimensional artificial metamaterials is infiltration into ordered templates called opals made of polystyrene or silica spheres. These inverse opal structures are made using spheres on the order of 400 – 500 nm, with the smallest periodicities considered about 100 nm. They are often infiltrated using electrochemical deposition. Structurally, these systems have a series of larger magnetic features connected by a network of magnetic legs. The structural features change the magnetic behavior by acting as pinning sites [35] and adding new anisotropies to the system [36] (see Section 1.3). The magnetic properties are highly dependent on both the periodicity and the thickness of the inverse opal structure. Micromagnetic simulations have indicated that the legs in these systems function as magnetic islands in an artificial spin ice system, obeying the ice rule of two in, two out. The larger magnetic features go into a magnetic vortex state and thus do not contribute to the net magnetization of the system. In an external field, transitions between these complicated magnetic states lead to sharp jumps in the hysteresis. These jumps have not been reproduced experimentally [37].

In this dissertation, we consider a similar three-dimensional system to the inverse opal structure, but on a smaller periodicity, which we refer to as a metalattice. These are artificial structures with a small periodicity and a highly interconnected surface throughout. Unlike nanowires or quasi-2D films, for a metalattice, the confined and extended degrees of freedom cannot be separated [38]. For this dissertation, the metalattices considered consist of Ni, Pd, or Pt infiltrated into close-packed lattices of silica spheres with sizes ranging from 14 nm to 100 nm. The close-packed structure is well maintained in 100 nm, 60 nm, and 30 nm lattices, but measurements indicate a potential change in geometry for the 14 nm lattices. The geometry of these systems, both in cross-section and in a 3D rendering, is shown in Fig. 1.5. The spaces in the lattice that are infiltrated with magnetic material come in two sizes. There are larger octahedral sites that are about 41.4 nm or 12.2 nm for a 100 nm and 30 nm metalattice respectively. The smaller tetrahedral sites are 22.5 nm and 6.8 nm respectively. There are also magnetic necks of 7.8 nm and 2.3 nm. For simplicity, the size of the system is characterized by the size of the spheres used to create the template. This size regime for magnetic metamaterials is interesting because it is in the range of the magnetic exchange

length, the characteristic length over which magnetic interaction occurs. For nickel, the exchange length is 47 nm [39].

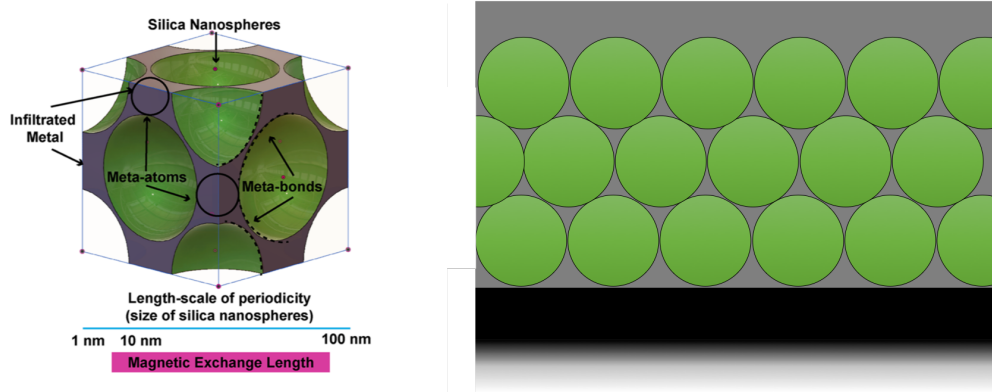


Figure 1.5. Left: 3D rendering of the geometry of magnetic material infiltrated into a metalattice, with example tetrahedral sites (meta-atoms) and necks (meta-bonds) highlighted. Reproduced from [38]. Right: Cross-sectional view of an infiltrated metalattice, showing the sphere template in green, the infiltrated metal in grey, and the silica substrate in black. There is usually a thick layer of metal on top of the infiltrated template at the end of the infiltration process that is removed later. Figure is not to scale.

These systems are non-trivial to fabricate, but there have been computational studies about how the magnetism in these systems might behave [40]. Due to the anisotropy introduced by the geometry, as the system becomes smaller the magnetization is confined to point in specific directions determined by the lattice structure. For larger inverse opal structures there are rich local dynamics leading to many jumps in the magnetization. This is related to the strong curling leading to vortices in the tetrahedral and octahedral sites. As the size is decreased into the metalattice regime, the magnetic features become too small to support these curling modes. By a 200 nm periodicity, only the octahedral sites are predicted to support such a mode, and by 90 nm no sites are predicted to support them [40]. Experimentally this transition has been observed around 200 nm rather than 90 nm [41]. Below this transition, the magnetization is predicted to order into a set of topologically distinct states, and transitions between these states can be initiated by sweeping a magnetic field. As the periodicity continues to decrease, the magnetization in the system continues to become more constrained until around 40 nm where it is expected to all align and show a square magnetic hysteresis with no jumps or transitions, with coercivity decreasing as the size is decreased. This is along the preferred axis of the system, but there are similar predictions for other

lattice directions (See Fig. 1.6).

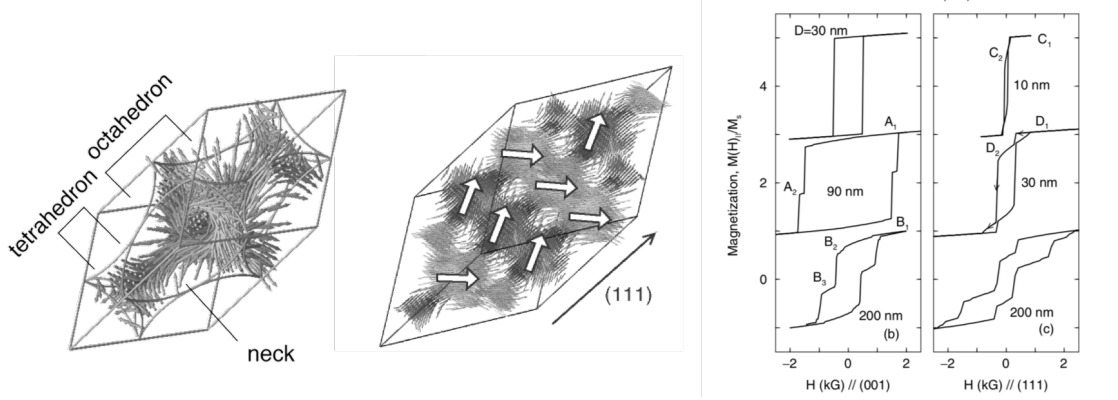


Figure 1.6. Magnetization showing curled domains in large periodicity samples and ordered domains in small periodicity samples, along with corresponding simulated hysteresis loops at different orientations and periodicities. Reproduced from [40]

While our initial interest in these systems was brought about by the desire to observe this ordering of the magnetization, these systems have other potential uses as well. Much like artificial spin ice, this is a diverse material system with applications far beyond its original intended design. The large surface-to-volume ratio makes them advantageous candidates for utilizing surface effects. The combination of confinement and large scale interconnectivity makes them an unusual platform for studying induced magnetism in Pd and Pt. The results presented in this dissertation are carried out using bulk magnetometry measurements, but these systems can also be studied using an imaging technique such as Lorentz TEM, or x-ray imaging techniques. The interconnectivity also means that these samples can be studied using electrical transport measurements.

1.2 Magnetism

The systems presented in this dissertation are all magnetic metamaterials. To fully appreciate these systems, a basic understanding of the origin of magnetic effects in materials is required.

1.2.1 Paramagnetism

Electrons form the basis of magnetism in materials. Each electron is a spin $1/2$ particle, with two possible states at any given energy level. These states correspond to spin $\pm 1/2$ and are denoted as spin up and spin down. Electrons that are anti-aligned effectively cancel out one another's spin angular momentum, thus atoms in which all electrons are paired do not exhibit a net magnetic moment. Electrons in atoms fill sub-shells in order of increasing energy: 1s, 2s, 2p, 3s, 3p, 4s, 3d, 4p etc. Each subshell can hold a fixed number of electrons: s shells can hold 2, p shells 6, and so on. Hund's rules dictate that a sub-shell will be filled with electrons arranged in a parallel direction before incorporating antiparallel spins, so partially filled shells will have unpaired electrons and thus a net magnetic moment. Consider Pd, a paramagnetic material that will be discussed in this dissertation. It has 8 electrons in the outermost shell (3d), which holds a maximum of 10 electrons. This leaves it with 2 unpaired electrons (5 spin up and 3 spin down), leading to paramagnetism.

The behavior of paramagnets is dominated by thermal energy, $k_B T$. In the absence of an external field, the magnetic moments randomize completely due to thermal fluctuations. In the presence of an external field, the moments tend to align with the external field. This alignment is not perfect, because the thermal fluctuations still work to randomize the system. The magnetization of a paramagnet follows the equation

$$M = \chi H = \frac{C}{T} H \quad (1.1)$$

χ is the susceptibility, H is the external applied field, and C is the material specific Curie constant. The magnetization increases as the external field used to align the spins is increased, or as the temperature is decreased causing a decrease in the impact of thermal fluctuations.

1.2.2 Ferromagnetism

Temperature Dependence

If there exists a spontaneous magnetization, a non-zero magnetization in zero magnetic field, a system is said to be ferromagnetic. For this to occur, two criteria

must be met. First, the system must be at a sufficiently low temperature that thermal fluctuations do not dominate the behavior of the system. The temperature where the system transitions from spontaneous order to random thermal fluctuations, or from ferromagnetism to paramagnetism, is referred to as the Curie temperature (T_C), described by the Curie-Weiss law:

$$\chi = \frac{C}{T - T_C} \quad (1.2)$$

Where C is the Curie constant and χ is the magnetic susceptibility. The Curie temperature is material dependent and can take on a large variety of values. For a paramagnet, the Curie temperature is zero and thermal fluctuations dominate at all temperatures. In this case, the equation reduces to Eqn. 1.1. In this dissertation, we are primarily interested in materials with a Curie temperature well above 300 K so that magnetic order can be observed at room temperature. For example, T_C is 627 K for Ni and 1388 K for Co [39].

Interaction and Stoner Criterion

The second criterion for spontaneous magnetization is sufficient interactions between electrons. Consider Co and Ni, two of the most commonly recognized magnetic elements and ones which will be discussed throughout this dissertation. Co has 7 electrons in the outermost shell (3d), and Ni has 8. This leaves Co with 3 unpaired electrons (5 spin up and 2 spin down) and Ni with 2 unpaired electrons (5 spin up and 3 spin down), leading to a net magnetic moment in atoms of each of these elements. For Ni, this is identical to the description of Pd, but Ni is ferromagnetic while Pd is paramagnetic. The interaction that leads to ferromagnetism is the magnetic exchange interaction, a fundamentally quantum mechanical property arising from the nature of electrons under exchange. Rather than attempt a full quantum mechanical description of magnetism, it is sufficient to use a semi-classical approach, accepting the existence of the exchange integral, J . The energy due to exchange can be written as:

$$E = \sum_{i,j} J_{i,j} \vec{s}_i \cdot \vec{s}_j \quad (1.3)$$

This equation is the Heisenberg Hamiltonian and is typically taken to be accepted as a valid starting point for theories of magnetism in insulators [39]. The sum is taken over pairs of spins such that $i \neq j$. The exchange constant J gives the sign and strength of the exchange interaction for the pair of spins being considered. Because the interaction comes from the exchange in location of two electrons, it is a very short range interaction and falls off rapidly with increasing distance. The length over which the interaction is significant, the magnetic exchange length, varies by material. The sign of J determines the preferred alignment of spins to minimize the energy of the system. $J < 0$ leads to a preferred alignment and ferromagnetism; $J > 0$ leads to a preferred anti-alignment and antiferromagnetism. In this dissertation, we work mostly with ferromagnetic materials, described in more detail in Section 1.3. Perpendicular artificial spin ice is actually an antiferromagnetic metamaterial because neighboring spins minimize their energy when anti-aligned. Ni, while ferromagnetic, actually becomes antiferromagnetic when oxidized into NiO. While the exchange interaction is a short-range effect, it leads to long-range order as interactions between neighboring spins mediate interactions between distant spins.

Exchange asymmetry is a fundamental property of electrons and occurs even in non-ferromagnetic materials such as Pd, indicating there must be some criterion on the exchange interaction which tells us when it is sufficient to produce magnetic order in materials. There is not a cutoff for the exchange interaction itself, but rather a consideration of both the magnetic exchange and the electronic band structure of the material. This criterion is called the Stoner criterion,

$$ID(E_F) > 1 \tag{1.4}$$

Here I is an exchange parameter related to J and $D(E_F)$ is the density of states at the Fermi level. The Stoner criterion tells us that for a metal to exhibit ferromagnetism there needs to be both a sufficient exchange interaction and a sufficient density of states around the Fermi level. Examples of the values of these parameters in real materials are given in Section 1.3. To understand the Stoner criterion, consider the effect of exchange on the electronic band structure. The exchange interaction causes a splitting of the d bands, so that opposite spin states have slightly different energies. The stronger the exchange interaction, the larger the

splitting. A simplified rigid band model showing the splitting of the 3d band in Ni is shown in Figure 1.7. The location of the Fermi level in the band leads to a majority and minority spin population. If the density of states around the Fermi level is insufficient, there will be no observable magnetism because the difference in the majority and minority spin populations will be too small.

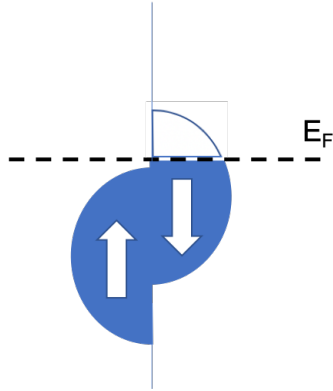


Figure 1.7. Simplified schematic of the d band splitting near the Fermi level in Ni. Figure reproduced based on [39]

Magnetic Fields

In addition to interacting with other magnetic spins in a material, each magnetic spin can also interact with an external field via the Zeeman interaction:

$$E = -\mu_0 \vec{s} \cdot \vec{H} \quad (1.5)$$

where \vec{H} is the external field. The Zeeman energy is minimized when a magnetic moment aligns with the applied field.

In the presence of an applied field, ferromagnets have a property called hysteresis. This means that the response of a magnet to an external field depends not only on the field applied but also on the magnetic history of the system. This comes from the competition between the energy from the exchange interaction which is minimized when the magnetization of neighboring spins is aligned, and the Zeeman energy which is minimized when the magnetization is aligned with the external field. A sufficiently high magnetic field will align all magnetic moments with the external field. In this state, a sample is saturated, and has magnetization M_S (saturation

magnetization). As the field is decreased to zero, the exchange interaction keeps the moments aligned. In real systems, there will be some relaxation due to other energies in the system. The remaining magnetization when the field is reduced to zero is the remnant magnetization, M_R . As the field direction is reversed and the field increases, at some point the Zeeman energy will be enough to overcome the exchange energy and the magnetization will begin to reverse. The field at which the magnetization passes through zero during the reversal process is material dependent and referred to as the coercive field, H_C . As the field continues to increase, the system will once again have all of its magnetic moments aligned with the external field and return to a saturated state in the opposite magnetic orientation. An example of this is shown in Fig. 1.8. This discussion is valid for preferred magnetization directions in hard ferromagnets. More complicated scenarios will be discussed later.

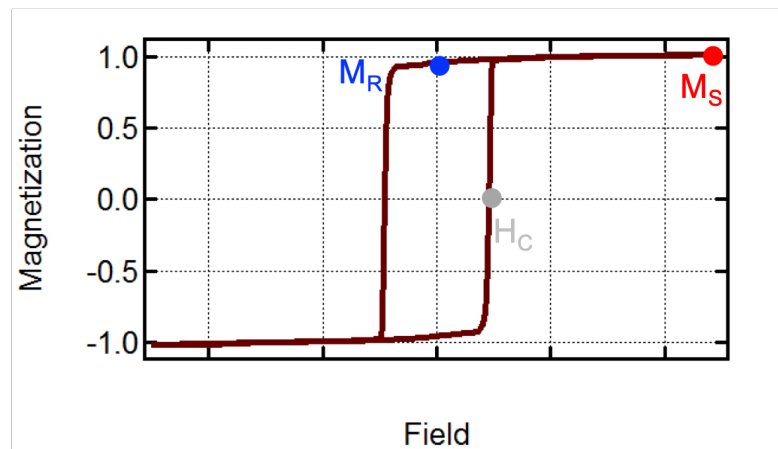


Figure 1.8. Example of hysteresis in a magnetic material. This data was taken on a Pt/Co multilayer film and is displayed with the magnetization normalized to the saturation magnetization.

Magnetic Domains

Each magnetic moment in a material, in addition to interacting with an external field, also creates its own dipolar field. Thus, an “external” field is also generated by the magnet itself. The interaction of the magnetization in a sample with the magnetic field it creates leads to an additional energy term of magnetostatic energy.

$$E_{MS} = \int_{sample} \vec{H}_D \cdot \vec{M} dV \quad (1.6)$$

\vec{M} is the sample magnetization and \vec{H}_D is the internally created dipolar field, usually referred to as the demagnetizing field. This energy is minimized by minimizing both the demagnetizing field and the sample magnetization, which causes the system to break up into ferromagnetic regions in which the magnetization is aligned called domains. Domains are separated by regions of transition from one state to another called domain walls. The demagnetizing field falls off less sharply than the exchange energy, so it governs longer range interactions in magnetic materials, on the micron length scale. The relative strengths and characteristic length scales of these two terms determine the preferred domain state of a given magnetic material.

Ferromagnetic domains and domain walls vary significantly with material properties. In a perpendicular ferromagnetic material such as Pt/Co multilayers, the domain wall width is on the order of 10s of nanometers, while in a soft ferromagnetic material such as permalloy it is 100s of nanometers. The characteristic domain wall width in a material is

$$\lambda = \pi \sqrt{\frac{A}{K}} \quad (1.7)$$

A is the exchange stiffness constant, which is related to the exchange integral. K is the anisotropy constant, related to how strongly the magnetization prefers to lie in a given direction. Materials with stronger directional preferences for magnetization have larger anisotropy. In addition to differences in domain wall width, there are also multiple potential orientations through which the magnetization may rotate as it changes between domains. In Bloch walls, the magnetization rotates parallel to the domain wall. In Néel walls, the magnetization rotates perpendicular to the domain wall. The Pt/Co multilayers discussed in this dissertation most likely have complex domain walls that are a mixture of these two types.

Domains play a pivotal role in hysteretic switching. When a magnet switches its orientation, first a small domain is nucleated. Then, the applied field expands the domain, causing the domain walls to move. There is an energy cost for lengthening the domain wall, but it is not as significant as the initial energy cost of creating the domain wall. So if a domain is nucleated with a pulse of field, it can be expanded in a much lower field than switching occurs in a hysteresis loop. The rate at which domains expand in a field is characterized by the rate at which the domain walls

move, the domain wall velocity. There are different regimes of motion, determined by external field strength and material properties. In this dissertation, domain walls are driven in the “creep” regime. In this regime, domain walls are modeled as 1D elastic interfaces moving in 2D pinning potential. The velocity at which domain walls move depends both on the temperature of the measurement and the applied field according to the equation

$$v = v_0 \exp \left[- \frac{U_d}{k_B T} \left(\frac{H_d}{H} \right)^\mu \right] \quad (1.8)$$

μ is a critical exponent and is $\frac{1}{4}$ in the creep regime. U_d and H_d are the depinning energy and field of the system.

Adding domain walls to a system helps lower the magnetostatic energy but at a cost to the exchange energy. As patterned magnetic features are decreased in size, the maximum magneto-static energy is also decreased. Below some threshold size, the cost of putting a domain wall in the feature cannot be balanced by the gain in magnetostatic energy and the feature is constrained to remain always in a single domain. Features below this limit are used to build artificial magnetic systems. The nature of this transition in Pt/Co multilayers is thoroughly examined in Chapter 3.

I have mentioned now several times the concept of magnetic anisotropy, or the idea that magnetization may have a preferred orientation in a material. Different materials have different anisotropy considerations. Specific examples of anisotropy will be covered in Section 1.3.

1.2.3 Superparamagnetism

Another possible magnetic state with features of both ferromagnetism and paramagnetism is superparamagnetism. It is easiest to imagine a superparamagnetic system as a collection of nanoparticles. Each nanoparticle is ferromagnetic but is not exchange coupled to the surrounding nanoparticles. These particles each act as a “superspin”, which behaves as a paramagnetic spin as described in Section 1.2.1 but with an extremely large magnetic moment. Like paramagnetic spins, superspins undergo thermal fluctuations but because of the large moment of the superspins, they take more thermal energy to reverse. The thermal energy is sufficient to dominate experimental measurements at and above the blocking temperature, below which

the particle is “blocked” in its initial state throughout the measurement and not subject to thermal fluctuations. A blocked superparamagnet appears ferromagnetic in measurements. The blocking temperature is described by the following equation:

$$T_B = \frac{KV}{k_B \ln \frac{\tau_N}{\tau_0}} \quad (1.9)$$

Where K is the anisotropy constant, V is the volume of the particle, τ_0 is the attempt time characteristic to the material, and τ_N is the average reversal time due to thermal fluctuations. Larger particles and particles with higher anisotropy tend to be blocked at higher temperatures. Larger particles are blocked at higher temperatures because the moment is larger and therefore takes more thermal energy to reverse. Particles with stronger anisotropy are blocked at higher temperatures because the magnetization has a stronger preference for lying in a particular direction and therefore is more difficult to reverse.

While it is simple to picture them as such, superparamagnets need not be collections of isolated nanoparticles. Superparamagnetic behavior can also occur in the switching behavior of magnetic thin films [42], granular nanostructures [43], or other magnetic systems. The artificially patterned islands that form the basis of magnetic metasystems such as artificial spin ice are blocked superparamagnetic spins. The superspins are used model real spins and build artificial systems with desired interactions which can be tuned by changing the geometry of the superspins, or the interaction strength of the superspins. Thermal effects can be considered by decreasing the blocking temperature of the superspins so that they are free to thermally fluctuate in accessible temperature regimes.

In some cases, it is the lack of superparamagnetic behavior that gives interesting information about a system. For example, in the metalattice geometry described in Section 1.1.3, one important characteristic of the system is that it is fully interconnected. It is well known that Ni nanoparticles in the size regime of the meta-atoms in our structure behave as superparamagnetic spins with a blocking temperature below room temperature [44]. So the lack of such a blocking transition would indicate that there is inter-particle exchange interaction occurring and that the system must be interconnected rather than discrete particles.

1.3 Materials

Specific magnetic properties depend on the particular materials system to be studied. Part of designing effective artificial magnetic systems is choosing appropriate materials to achieve the desired characteristics for that particular system. Four different magnetic materials investigated in this dissertation are presented in this section.

1.3.1 Pt/Co Multilayers

The material used to create the magnetic features and perpendicular artificial spin ice arrays considered in Chapters 3 and 4 is a Pt/Co multilayer stack [45]. Co is one of the three commonly known room temperature ferromagnetic metals. In a film of Co, the anisotropy (the existence of a directional dependence to the preferred orientation of the magnetization) makes it so the magnetic moment lies in the plane of the film. The direction the magnetization prefers to lie is referred to as an “easy axis”, whereas a direction that the magnetization does not naturally point is referred to as a “hard axis”. When a magnetic field is applied along an easy axis, the magnetization behaves as described in Section 1.2.2. Along a hard axis, a high magnetic field will still bring the system to a saturated state. However, as the field is decreased, the magnetization will relax into its easy axis, decreasing the magnetization in the direction of the applied field. Once the field is removed, the magnetization will lie entirely in the easy axis direction. If the hard axis being probed is perpendicular to the easy axis, this will give zero magnetization at zero magnetic field. This is illustrated in Fig. 1.9.

To rotate the magnetic anisotropy direction in Co to lie perpendicular to the film plane, scientists designed a system that takes advantage of the surface anisotropy. The bulk, or volume, anisotropy comes from magnetocrystalline anisotropy, which is highly dependent on the lattice structure of the element. It arises from the coupling of the electronic orbitals to the lattice structure. The surface of a magnetic film behaves differently than the interior because electrons are unlikely to be found outside the surface of the material, which changes the electronic structure at the surface. So when considering the anisotropy of a thin film, we consider the bulk anisotropy and the surface anisotropy separately. The anisotropy is typically given

as a normalized value in Jm^{-3} , and so the effective anisotropy taking into account both bulk and surface terms is

$$K_{\text{eff}} = K_v + \frac{2K_s}{t} \quad (1.10)$$

Here K_v is the normalized volume anisotropy, K_s is the normalized surface anisotropy, the factor of 2 comes from the assumption of 2 identical surfaces, and the factor of thickness t is necessary to have the correct units and normalization. As the thickness decreases, the relative contribution of the surface anisotropy increases. As this anisotropy is perpendicular, whereas the volume anisotropy lies in the plane, this leads to a transition to effective out-of-plane anisotropy for sufficiently thin cobalt layers. This transition takes place at a layer thickness of around 12 Å.

Strain also affects the anisotropy in magnetic thin films, and to get clean and uniform anisotropy we want to minimize strain in the system. Our samples are grown on Si wafers and contain a thin layer of Ti as an adhesion layer, a thick buffer layer of Pt, and then alternating thin layers of Co and Pt. The overall structure is $\text{Ti}_{2\text{nm}}\text{Pt}_{10\text{nm}}[\text{Co}_{0.3\text{nm}}\text{Pt}_{1\text{nm}}]_8$. The lattice parameters of our deposited materials are 2.95 Å (Ti), 3.92 Å (Pt), and 3.54 Å (Co). While the Ti layer is necessary for good adhesion and continuous film growth, it has a significant lattice mismatch with Pt, which introduces strain into the Pt layer. The thick Pt buffer layer allows the strain to relax, leading to unstrained interfaces and stronger anisotropy in the multilayer structure. Thin magnetic layers (Co) separated by thin non-magnetic

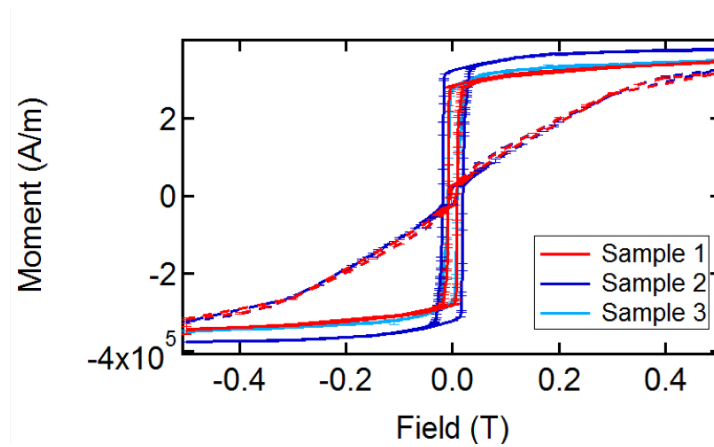


Figure 1.9. SQUID measurement of magnetization vs. magnetic field in various Pt/Co multilayer samples. Solid lines are measured with the field perpendicular to the film plane. Dashed lines are measured with the field parallel to the film plane.

spacers (Pt) couple together, causing the magnetization in each layer to switch together with adjacent layers. The overall magnetization of the film is increased by adding successive layers. Increased film magnetization gives each patterned island in our artificial spin ice arrays an increased magnetic moment, leading to stronger coupling. However, adding too many layers affects the perpendicular anisotropy of the system and also decreases the strong coupling between all layers in the system leading to less square hysteresis. For high-quality artificial spin ice arrays, the number of layers and layer thickness are tuned to maximize perpendicular anisotropy and saturation magnetization while maintaining the desired loop shape. We chose the parameters used in the films presented in this dissertation because they have our desired properties based on studies in literature. Magnetization information collected using superconducting quantum interference device (SQUID) magnetometry with the field oriented both in the sample plane (dashed lines) and perpendicular to the sample plane (solid lines) for three different depositions of Pt/Co used in this dissertation is presented in Fig. 1.9. These data show that while there is some variation in coercivity and saturation between different depositions, overall samples deposited with this structure show square hysteresis loops with a high remanence and a strong preference for the perpendicular orientation.

1.3.2 Permalloy

Some of the samples in this dissertation are also patterned using a permalloy (Py) underlayer. Permalloy is a Ni and Fe alloy, with 78% Ni. Unlike the Pt/Co multilayer samples presented in the previous section, Py prefers to have its magnetization lie in the film plane, with no preferred orientation in the plane. From the SQUID data presented in Fig. 1.10 we see that the easy axis is now the in-plane orientation and that the out of plane orientation is a hard axis. Again, the dashed line was collected with the field lying in the plane of the film and the solid line was collected with the field perpendicular to the plane. Py is also a soft magnetic material, meaning that the coercivity is very low and it takes very little applied field to reorient the magnetization of the material in the plane of the film. We take advantage of these properties of permalloy to increase the coupling between neighboring islands in artificial spin ice arrays.

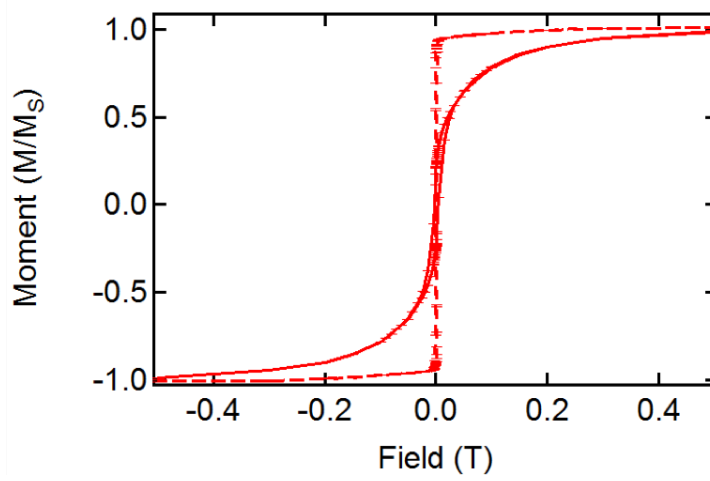


Figure 1.10. SQUID measurement of magnetization vs. magnetic field in a Py film. The dashed line was measured with the field oriented in the plane of the sample, and the solid line was measured with the field oriented perpendicular to the sample.

1.3.3 Nickel

Nickel, again, is one of the three room temperature ferromagnets. As described in Section 1.2.2, this is because Ni has both sufficient exchange coupling and a peak in the density of states around the Fermi level. The density of states of Fe, Co, and Ni, along with I , $D(E_F)$ and $ID(E_F)$ for the first 50 elements in the periodic table are shown in Fig. 1.11. This clearly shows that Ni meets the criteria to be ferromagnetic.

Ni is used for three-dimensional magnetic metastructures, for which there are different anisotropy considerations than the surface effects in Pt/Co. In these samples, the anisotropy is dominated by the pattern of the structure rather than the intrinsic magnetocrystalline anisotropy of the Ni. It is actually to our benefit in this respect that the Ni we use is highly polycrystalline. The magnetocrystalline anisotropy in polycrystalline materials can be understood using the random anisotropy model [48]. Each small crystal grain has its anisotropy oriented in a slightly different direction. Because these grains are smaller than the characteristic length scale of the magnetism in Ni, the anisotropy direction becomes averaged out over multiple grains within the magnetic exchange length. This effectively softens the overall anisotropy of the Ni compared to a single crystal sample.

The dominant anisotropy arises due to shape anisotropy from the pattern

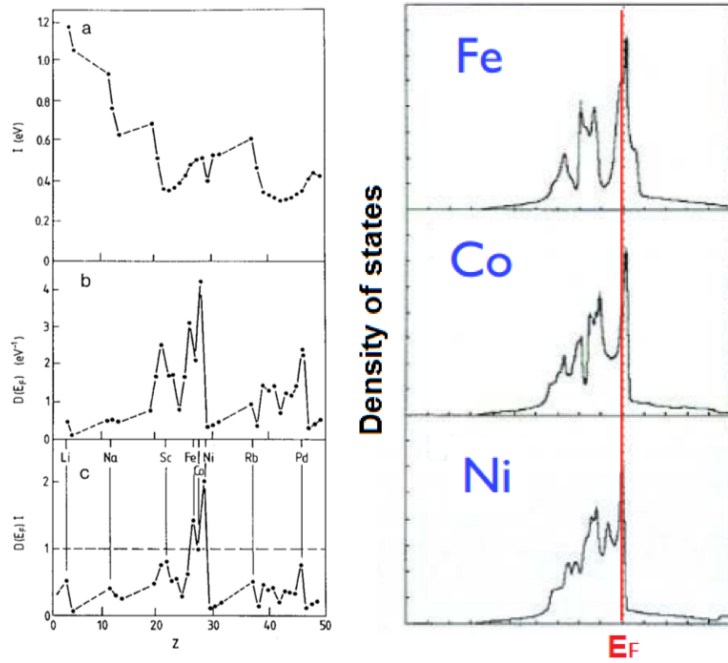


Figure 1.11. Left panel: I , $D(E_F)$, and $ID(E_F)$ for the first 50 elements, showing only Fe, Co, and Ni fulfill the Stoner criterion. Right: The density of states in Fe, Co, and Ni showing that each has a peak in the density of states at the Fermi Level. Graphic partially reproduced from [46] and [47]

of the structure, related to the demagnetizing field. In larger ferromagnets, the demagnetizing field favors the formation of domains. In small structures that cannot support domain walls, the demagnetizing field serves to orient the magnetization in particular directions in asymmetric shapes by minimizing stray fields created when the magnetization points perpendicular to the surface of a magnet. This introduces a preferred magnetization direction along the long axis of an oblong magnetic particle because this orientation leads to smaller stray field components compared to magnetization along the short axis (See Fig. 1.12). In the context of our metamaterials, this means that the shape anisotropy constrains the magnetization to prefer to lie along the magnetic necks as described in Section 1.1.3, and thus give rise to theoretically predicted magnetic states .

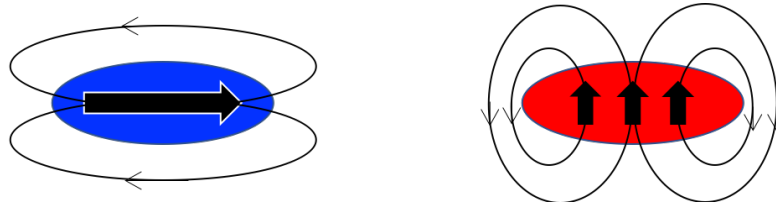


Figure 1.12. Shape anisotropy in oblong nanoparticles. Analogous to the shape anisotropy that occurs in the more complicated metalattice geometry.

1.3.4 Platinum and Palladium

From the periodic table, it is apparent that Ni, Pd, and Pt all have the same outer valence structure, as they are all in the same column (See Fig. 1.13). However bulk Ni is ferromagnetic, while bulk Pd and Pt are paramagnetic. This is because the density of states in Pd and Pt are different from the density of states in Ni, so they do not fulfill the Stoner criterion (see Fig. 1.11). Considering the band structure of Pd (Fig. 1.14) we see that there is a peak in the density of states slightly below the Fermi Level, but not coinciding with the Fermi Level. This suggests a potential avenue to induce magnetism in Pd.

Group	1	2	3	4	5	6	7	8	9	10	11	12	13	14	15	16	17	18
1	1 H																	2 He
2	3 Li	4 Be											5 B	6 C	7 N	8 O	9 F	10 Ne
3	11 Na	12 Mg											13 Al	14 Si	15 P	16 S	17 Cl	18 Ar
4	19 K	20 Ca	21 Sc	22 Ti	23 V	24 Cr	25 Mn	26 Fe	27 Co	28 Ni	29 Cu	30 Zn	31 Ga	32 Ge	33 As	34 Se	35 Br	36 Kr
5	37 Rb	38 Sr	39 Y	40 Zr	41 Nb	42 Mo	43 Tc	44 Ru	45 Rh	46 Pd	47 Ag	48 Cd	49 In	50 Sn	51 Sb	52 Te	53 I	54 Xe
6	55 Cs	56 Ba	57 La	72 Hf	73 Ta	74 W	75 Re	76 Os	77 Ir	78 Pt	79 Au	80 Hg	81 Tl	82 Pb	83 Bi	84 Po	85 At	86 Rn
7	87 Fr	88 Ra	89 Ac	104 Rf	105 Db	106 Sg	107 Bh	108 Hs	109 Mt	110 Ds	111 Rg	112 Cn	113 Nh	114 Fl	115 Mc	116 Lv	117 Ts	118 Og
				* 58 Ce	* 59 Pr	60 Nd	61 Pm	62 Sm	63 Eu	64 Gd	65 Tb	66 Dy	67 Ho	68 Er	69 Tm	70 Yb	71 Lu	
				* 90 Th	* 91 Pa	92 U	93 Np	94 Pu	95 Am	96 Cm	97 Bk	98 Cf	99 Es	100 Fm	101 Md	102 No	103 Lr	

Figure 1.13. Periodic table with Ni, Pd, and Pt highlighted to show they have the same valence structure. Graphic taken from Wikipedia

Theoretical investigations of magnetic ordering in Pd show that while Pd is not natively in a magnetic state, the system actually achieves a permanent magnetic ordering when the lattice spacing is increased. Calculations indicate that a 5.5% increase in lattice spacing is sufficient to produce a permanent magnetic moment [50] (See Fig. 1.15). This theoretical prediction supporting the idea that changing the

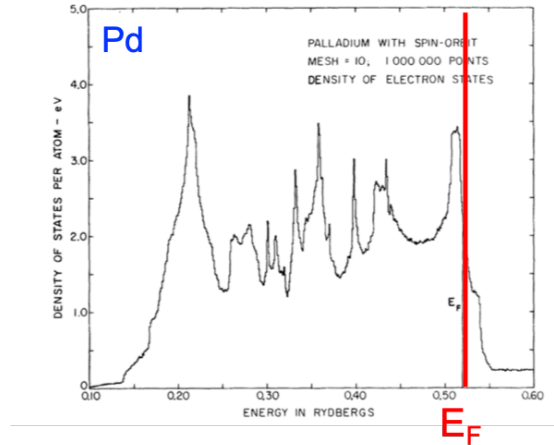


Figure 1.14. The density of states in Pd, with the Fermi level highlighted in red, showing that the peak in the density of states is slightly removed from the Fermi Level. Graphic reproduced from [49] with emphasis added.

density of states could induce ferromagnetism in Pd helped lead to experimental investigations into these systems.

Scientists have experimentally observed that nanostructures of platinum and palladium such as nanoparticles or nanowires display ferromagnetic ordering. There are multiple possible explanations for how the transition into nanostructures affects the band structure. Some studies indicate that this effect is due to the particle surfaces. The particle surface functions as a 2D magnetic film, with ferromagnetism induced by the narrowing of the d bands on the (100) surfaces due to the decreased coordination of those surfaces. The narrowing of the d bands is sufficient to change the local density of states enough to fulfill the Stoner criterion (Eqn. 1.4) [51]. Other studies suggest that the enhancement of the local density of states occurs at twin boundaries, where the breaking of cubic symmetry again leads to a local d band narrowing and fulfillment of Stoner criterion [52,53]. An example of a nanoparticle containing a twin boundary, along with the magnetic response of both Pt and Pd particles containing these defects, is shown in Fig. 1.15 Studies of nanowires suggest as well that the source of ferromagnetism is either a crystal defect like a twin boundary or some other change of boundary condition such as a twist or bend in the wire [54]. These studies indicate that the source of interesting behavior in these systems is imperfections or defects. This also supports the idea that our metalattice geometry, which has many twists and bends and potential

locations for defects, is an interesting platform with which to study magnetism in Pd and Pt samples.

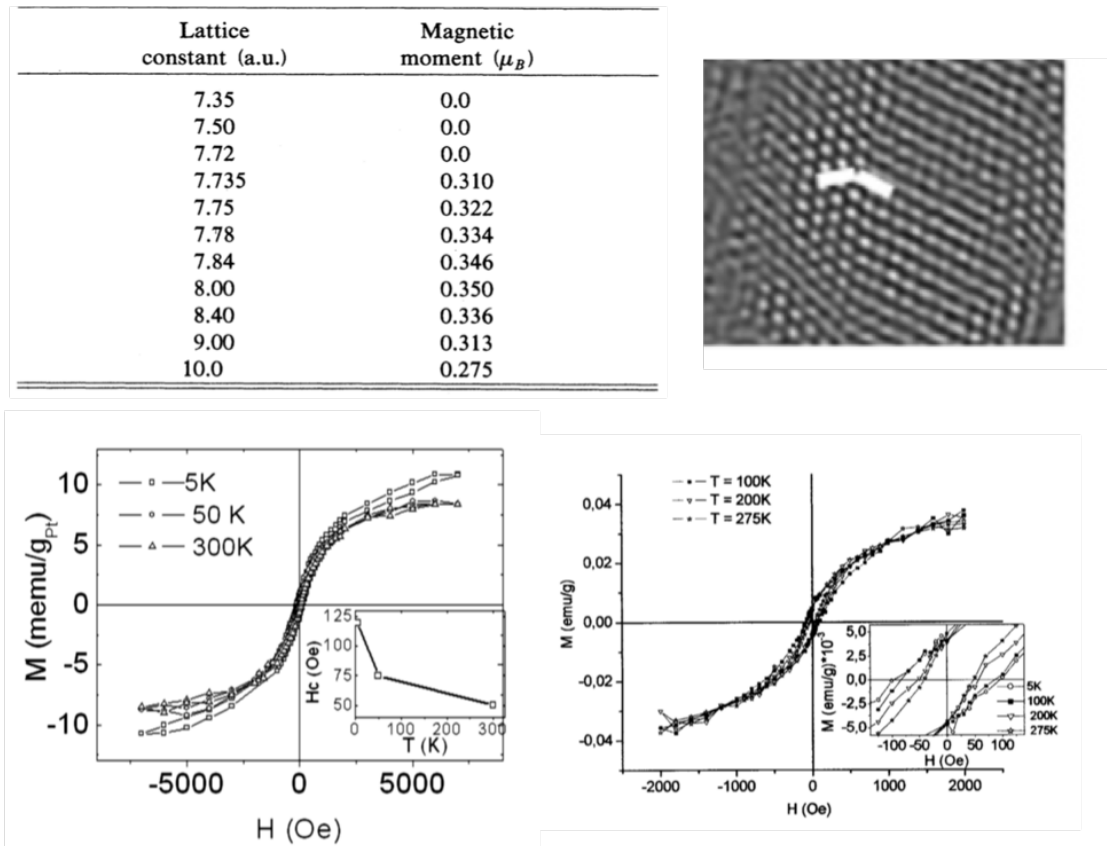


Figure 1.15. Top Left: Table showing values of magnetic moment as a function of lattice spacing. Reproduced from [50] Top Right: TEM image of a Pd nanoparticle showing a twin boundary, highlighted with the white line. Bottom: Hysteresis loops showing magnetism in Pt (left) and Pd (right) nanoparticles containing twin boundaries. Reproduced from [52] and [53]

Chapter 2 | Experimental Techniques

This chapter contains explanations of the basic techniques used for sample fabrication and characterization, as well as an overview of computational methods used for data analysis. Detailed procedures for lithography and film deposition and detailed documentation for computational methods are contained in Appendix A and B respectively.

2.1 Sample Fabrication

To create understandable artificial systems, we need to both carefully control the fabrication process and accurately characterize fabricated samples. The characteristics of artificial systems are highly dependent on the fabrication procedures used to create them. Adjustments in the lithography process can change the size and edge profiles of fabricated features, which changes the interaction strengths and disorder present. Non-uniformity in film deposition can lead to variations in the magnetic moment and anisotropy in the films used to create the features, altering the system properties. We begin with a discussion of the fabrication process, before discussing characterization.

There are two separate fabrication pathways for samples presented in this dissertation. The first is the approach used to create the two-dimensional patterned features discussed in Chapters 3 and 4. This approach will be covered in detail. The second is the approach used to create the three-dimensional structures discussed in Chapter 5. This fabrication is carried out by collaborators and a detailed discussion is beyond the scope of this dissertation, but a qualitative description of the process is included to provide a basic understanding of how those samples are constructed.

2.1.1 Lithography

Nanoscale structures can be fabricated using either a bottom-up or a top-down approach. In a bottom-up approach, nanostructures are grown or assembled from individual atoms, and in a top-down approach, a larger scale system is patterned or otherwise reduced to the nanoscale. The patterned features discussed in this dissertation are created using a top-down approach.

All sample fabrication is carried out in a clean room environment at the PSU Nanofabrication Laboratory. Dust and other contaminants affect the quality of fabrication so every effort must be taken to keep samples free of contaminants during the fabrication process, beginning by preparing the substrates. In this dissertation, we use intrinsically doped Si wafers as sample substrates. Substrates are cleaned with acetone and isopropanol to remove contaminants from the surface and then heated on a hot plate to evaporate any residual water. Prepared substrates are then ready for resist deposition.

A resist is a long chain polymer whose properties can be altered by exposure to light using photolithography or electrons using electron beam lithography; Specifically, exposure alters the solubility of the polymer in certain chemicals used for development. Our fabrication process uses electron beam lithography as it allows for the creation of small features, with a lateral resolution as small as 10 nm. Resist polymers are suspended in a solvent before dispersal onto the substrate and come in either a positive or negative tone. With a positive resist, exposure to electrons increases the resist solubility, and the exposed portion can be removed from the resist film in the development step. With a negative resist, exposure to electrons reduces the resist solubility and the development step leaves behind the exposed pattern. In this work, we use two types of positive tone resists. The first is a bilayer resist stack of poly(methyl methacrylate) (PMMA) and polymethylglutarimide (PMGI). Bilayer resist stacks are useful for small features because the two layers develop in different solvents. This allows for the development of an undercut, where the bottom layer of resist is overdeveloped relative to the top layer [55]. Undercuts reduce sidewall deposition. This resist stack is shown in the cartoon of the fabrication process in Fig. 2.1. Newer samples were fabricated using ZEP as the resist, a resist that was developed specifically for high resolution electron beam lithography [56]. A high resolution resist is useful for perpendicular artificial spin

ice arrays because the most densely packed arrays with the highest interactions have small island-to-island edge separations of 50 nm. A high resolution resist might help us have more cleanly defined features.

Once the resist is selected, it is applied to the prepared substrate by spin coating. Spin coating allows a thin, even layer of resist to be applied. Any dust or debris on the substrate will interfere with the quality of the resist layer and therefore the quality of the remainder of fabrication. Debris that was missed during the preparation step is often visible as streaks in the resist, and these areas should be avoided as areas to write a pattern. After each layer of resist is applied, the sample is baked on a hot plate to remove any remaining solvent, leaving just the polymer layer. For e-beam lithography, a thin layer of gold is then evaporated on top of the resist as a conducting layer to prevent accumulation of charge from the beam.

At this point, the sample is ready for e-beam exposure. In electron beam lithography, a beam of electrons is used to write a pattern into the resist. This type of lithography uses a direct write procedure, meaning there are no masks to block exposure. Computer-aided drafting programs are used to create a pattern for the beam to trace out, and the beam is scanned over the sample to draw the desired pattern. There are multiple ways to achieve the same size/shape of features with e-beam lithography since the final physical properties of magnetic features are determined by a combination of the beam size and dose, and the developing time and solvent. Small beams are used for small features; larger features can be written with large beams to save time. Using the software available, different beams can be selected to write different parts of the overall pattern to optimize the process. For our samples, a small beam is used to write the small islands and a large beam is used to write the finder bars, large rectangles positioned surrounding the arrays that are used to help locate the patterned region in the optical microscope. We found that the most consistency between samples was achieved using a moderate e-beam dose and a long development time.

Once the pattern has been exposed, it must be developed. Development is a process by which the material with the lower solubility after exposure is chemically removed. The strength of the chemical used as well as the development time impact the final structure of the features. With the bilayer resist samples, the development is tuned such that the underlayer is overdeveloped when compared to the overlayer. Once the sample is developed the pattern is visible for the first time, and can be

observed in an optical microscope.

After development, the sample is ready for film deposition, described in detail in the next section. Following film deposition, the remaining resist and any metal that was deposited on top of it are removed, leaving just the desired structure. For the bilayer samples, PRS - 3000 is used to dissolve PMGI and acetone is used to dissolve PMMA. For the ZEP samples, the resist is removed with PG remover. To help the lift-off process, the PRS - 3000 and PG remover are heated, but must be carefully monitored for overheating as PRS - 3000 has a flash point near the temperature used in the lift-off process. To help ensure that no resist is left behind in densely packed arrays of features, after soaking the samples in the lift-off solvent the samples are sonicated briefly. A minute is sufficient; over-sonication can damage features.

A schematic showing the entire fabrication procedure with a bilayer resist stack is shown in Fig 2.1.

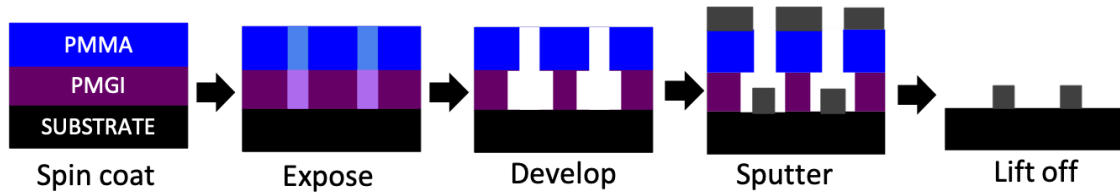


Figure 2.1. A schematic of the lithography process used to fabricate patterned magnetic thin films. This procedure features a bilayer of (PMMA/PMGI) as the resist, exposed using e-beam lithography, and developed with an undercut to prevent sidewall deposition. Produced based on figures from [55,57]

This process gives reasonably repeatable sample quality between depositions. Of course, with a real system, it is impossible to fully remove all sources of non-uniformity and disorder. However, having varying levels of disorder between fabrications – due to differences in preparation, development, and lift off – actually give us avenues for additional insight into the behavior of artificial spin ice. Continued improvements in fabrication to reduce sources of disorder will be paramount in fabricating samples that are capable of reaching a ground state.

2.1.2 Thin Film Deposition

We use two thin film deposition techniques to deposit the samples used in this dissertation: sputtering and evaporation. Sputtering is used to deposit Pt/Co multilayer films, and evaporation is used to deposit Py films and the thin gold layer necessary for e-beam lithography.

While we have sputtering capabilities at Penn State, the sputter depositions of the multilayer films presented in this dissertation are carried out using an ATC 2400 AJA International sputter system at Argonne National Laboratory [58]. Sputtering is a deposition technique that creates films using ion bombardment of a material source, or target. First, the substrate on which the film is to be grown is mounted in the sputtering chamber. An electric potential is created by applying a negative voltage to the target. This causes Ar^+ ions in the sputtering chamber to accelerate toward the target, ejecting atoms of the target material that are then deposited on the substrate to form a film. The sputtering process is highly energetic, and leads to more disordered interfaces in multilayers than a technique such as evaporation, leading to a decrease in the coercivity of the film. For our purposes, it is easier to work with samples with lower coercivity, as evaporated films tend to have coercivities beyond the range of our magnet. Additionally, there are practical considerations that make evaporating multilayers time consuming and challenging. Sputtering leads to the most repeatable and useful multilayer films.

Py and gold films are deposited in the nanofabrication facilities at Penn State using a Kurt Lesker Lab-18 Evaporator [59]. Again, we start by mounting the substrate in the chamber. To deposit a film by evaporation, source material in a crucible is heated past its boiling point, either thermally using resistive heating (Au) or by heating the sample with a beam of electrons (Py). Regardless of the type of heating, once the material is sufficiently heated it begins to outgas. This gas then condenses on the relatively cool substrate to form a film. To increase the uniformity of the deposited film, the holder on which the substrate is mounted is rotated throughout the deposition process. This rotation is advantageous for continuous films but should be avoided for deposition on to patterned samples as it can contribute to sidewall deposition. Also, when evaporation is used for patterned samples, the temperature of the process chamber is decreased to 0 C, to reduce the possibility of damage to the resist.

Side by side schematics of the sputtering and evaporation processes of film deposition are shown in Fig. 2.2.

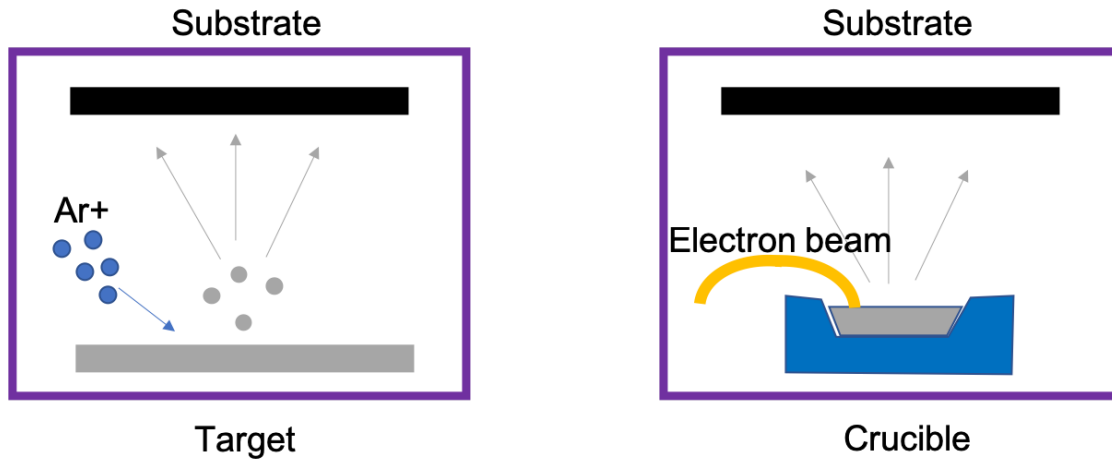


Figure 2.2. Left panel: Schematic representation of film deposition using sputtering. Ar^+ ions are accelerated toward the target, freeing some atoms to deposit on to the substrate as a film. Right panel: Schematic representation of film deposition using evaporation. The material in the crucible is heated above the boiling point using an electron beam, and evaporated material redeposits on the substrate as a film.

2.1.3 Metalattice Fabrication

The details of metalattice fabrication are beyond the scope of this dissertation. However, the process of fabricating these samples can be generally understood as a three step process: template synthesis, infiltration, and top coating removal. Template synthesis involves the self-assembly of silica nanospheres of the desired size into a close-packed lattice. Care must be taken in this and all future steps to avoid the introduction of contaminants that affect the magnetic signal, since the characterization method we use is quite sensitive (See Section 2.2.2). Once the template is synthesized, metal is infiltrated into the spaces between the nanospheres using high pressure confined chemical fluid deposition. This process is described in detail in reference [38]. Different metals have different relevant parameters for optimizing the deposition. Ni is very sensitive to confinement; well connected, large scale infiltration is only possible with intermediate confinement. For Pd depositions, high levels of strain lead to the templates peeling from the substrates unless accounted for by controlling the reaction rate using the temperature and H

concentration. For all metals, after infiltration, there is a film of material on top of the template. This contributes a large magnetic signal and masks the signal from the metalattice if not removed. The top layer is removed by either chemical (Ni) or physical (Pd, Pt) etching. Once the top layer is removed the samples are complete and ready for further characterization.

2.2 Sample Characterization and Measurement

2.2.1 Scanning Electron Microscopy

Scanning electron microscopy (SEM) is an imaging technique with high spatial resolution reaching down to approximately 1 nm. It uses a focused beam of electrons scanned over the sample surface in a raster pattern to create an image. When the beam interacts with the sample surface, electrons from the surface can be ejected (secondary electrons) or electrons from the original beam can be backscattered. The electrons from these two sources are collected in a detector and used to reconstruct a topographical image of the sample.

SEM is used for several types of characterization. In patterned film samples, we use SEM to verify that the sample completely lifted off and all resist has been removed. It allows us to measure the diameter of the islands since differences in fabrication can lead to different physical island sizes even in samples with identical patterned island sizes. It also gives the first indication of the level of disorder by allowing us to view the edge profile of the islands. In metalattice samples, we use SEM to check that the top layer has been fully etched.

It should be noted that prolonged exposure to an electron beam can damage multilayer samples, so as a standard practice multiple arrays of each lattice type and spacing are deposited on each sample, and arrays characterized by SEM are not used for further analysis.

2.2.2 Magnetometry Measurements

Magnetometry measurements presented in this dissertation are carried out using a Quantum Design Magnetic Properties Measurement System (MPMS) [60], which uses a superconducting quantum interference device (SQUID) detector to measure magnetization extremely sensitively. The MPMS has applied magnetic field

control up to 5.5 T using a superconducting magnet, and temperature control from 1.8 K to 350 K. Combining temperature and field control allows us to probe many magnetic properties including basic characterizations of coercivity, Curie temperature, magnetic saturation, and anisotropy axis; as well as more unusual characterizations such as verifying superparamagnetism using thermoremanent magnetization measurements (discussed in Chapter 5).

MPMS Instrumentation

The major components of the MPMS are the detection coils and associated SQUID, the magnetic shielding, the superconducting magnet, and the temperature control system. As many of these components are designed using superconducting wire, they must be operated at low temperatures and are immersed in or exposed to a bath of liquid helium to properly function.

The detection coils, shown in Fig. 2.3, consist of a set of four turns made of superconducting wire positioned outside the sample chamber at the center of the superconducting magnet. The outer two loops are wound counterclockwise and the inner two clockwise, a second-order gradiometer configuration, which serves to reduce the noise in the measurements. Any drifts or relaxation in the field of the magnet should occur uniformly over the four coils, leading to a zero net change in flux through the detector. The sample itself is oscillated through only the center detection coil during measurements, changing the flux through the detection coil and inducing a change in the supercurrent of the system. This change is used to inductively measure the magnetization in the sample. The magnetic shielding in the system provides additional stability and protection against noise, in addition to shielding the SQUID from the fields of the superconducting magnet.

One of the most important components of the MPMS is the SQUID connected to the magnetic detection coils. A SQUID consists of a superconducting loop with one or two Josephson junctions that serve as weak links. DC SQUIDS with two Josephson junctions offer higher sensitivities, but it has been difficult to manufacture two identical Josephson junctions. Therefore, RF SQUIDS with one weak link are more common and are what we use in our MPMS system. The Josephson junction in the MPMS is a superconductor-insulator-superconductor (S-I-S) junction, consisting of two sections of superconductor (Nb) separated by a

tunnel barrier (Al_2O_3). The SQUID detector functions as an extremely sensitive current to voltage converter. In summary, the sample is moved through the detection coils and induces a supercurrent, which is very precisely converted to a voltage by the SQUID. An example of the voltage response of the SQUID as a sample is passed through the detection coil is shown in Fig. 2.3. The ideal signal is modeled as a single point dipole with the center of the scan precisely on the detection coil. In situations that are reasonably close to this ideal, the magnetization of the sample can be retrieved from this curve.

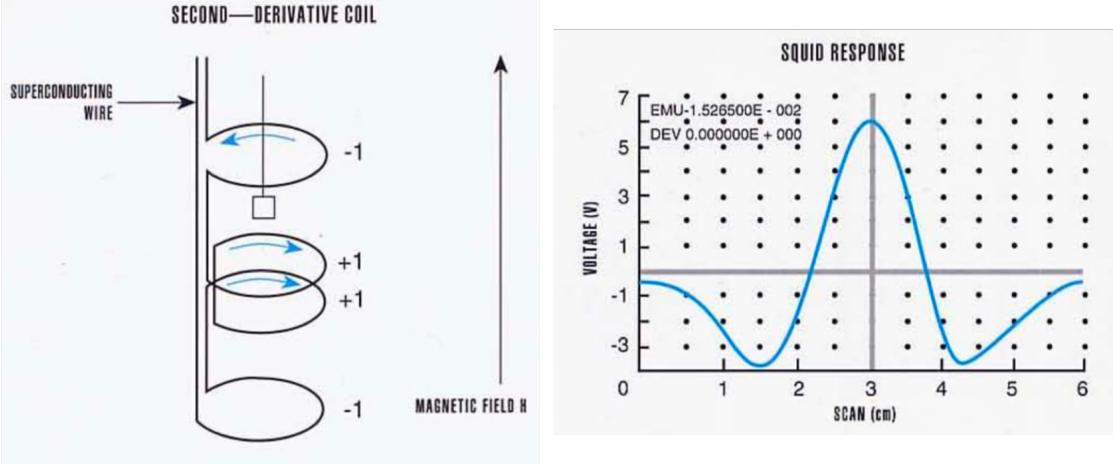


Figure 2.3. Left: Second order gradiometer configuration of the MPMS detection coils. Right: Voltage response of SQUID detector when an ideal sample is moved through the detection coils. Reproduced from [60]

The remaining two components of interest, the superconducting magnet and the temperature control system, are what allow us to use the MPMS to measure responses to external stimuli. The superconducting magnet is a solenoid created using a closed loop of superconducting wire, which can be supplied with current to generate a desired magnetic field up to 5.5 T. When operated in “persistent mode”, the mode in which we typically operate the system, there is no power supplied to the magnet while measurements are being carried out. This reduces noise in the magnetic field during measurement. To change the applied magnetic field, like while performing a hysteresis measurement, the current in the solenoid must be changed between measurements. Because the magnet is a closed loop superconductor, the current must be changed using a persistent switch, a small heater attached to part of the solenoid which can be used heat a small section

of the superconductor and cause it to transition into a normal metal state. This region can then be used to inject or deplete current from the magnet. It is necessary before opening the persistent switch to ensure that the current supplied by the power supply is not substantially different from the current already in the magnet. To change the magnetic field, the power supply is charged to match the current in the magnet, the persistent switch is opened, the power supply is slowly adjusted to the new desired current, and then the persistent switch is closed again. Once the magnet is charged, it takes additional time to stabilize due to residual magnetic forces acting on the superconducting wire. This is a slow process, but a significant difference in the applied current and the current already in the magnet could lead to a magnet quench, a runaway process in which the magnet transitions from superconducting to normal metal and begins to dissipate heat. While quenches are typically undesirable events, carefully controlled quenches after application of high magnetic fields are used to remove magnetic flux that can be trapped in the system.

The temperature control system contains a pair of heaters and a pair of thermometers to ensure accurate temperature control. When controlling the temperature of the system above the temperature of liquid He (4.2 K), the two heaters are used to modulate the temperature of He gas surrounding the sample space to maintain a consistent temperature environment up to 350 K. The sample is thermally coupled to the surrounding area by a small pressure of He gas in the sample chamber. Measurements below 4.2 K require a different type of temperature control. The space around the sample chamber is filled with a small reservoir liquid He and the temperature is controlled by adjusting the pressure on this reservoir. This type of cooling can reach temperatures down to 1.8 K.

Mounting and Loading

For measurements to be carried out, samples must be mounted in the center of the detection coils described above. This is accomplished by mounting samples in plastic straws, which are then attached to the end of a long graphite rod and suspended in the center of the sample chamber. The rod can be moved through a range of positions within the sample chamber, allowing for the generation of curves like those shown in Fig. 2.3. Because the magnetic field always lies along

the axis of the solenoid, to measure magnetization responses in different directions samples must be physically mounted in different orientations. To measure the magnetization perpendicular to the sample surface, a mesh of a plastic thread is sewn in the center of a straw. The sample is laid on the mesh, and an additional mesh is sewn over the top of the sample to hold it in place during measurement. To measure the magnetization in the plane of the sample, two straws are cut to a slightly shorter length. Then these straws are sliced lengthwise, the sample is inserted between the two straws, and the entire system is then inserted into a third straw for measurement. See Fig. 2.4 for illustrations of these two orientations. Because the SQUID is capable of such sensitive measurements, care must be taken to avoid introducing magnetic contaminants into the system. Thread and straws are plastic, which only contributes a diamagnetic signal to the measurement. Carbon or plastic tweezers are used, and plastic scissors, to avoid the transfer of trace magnetic materials from metal tools. Any metal that cannot be avoided, such as the needle used to sew the mesh in perpendicular mounting, should be wiped with ethanol before use to reduce contamination.

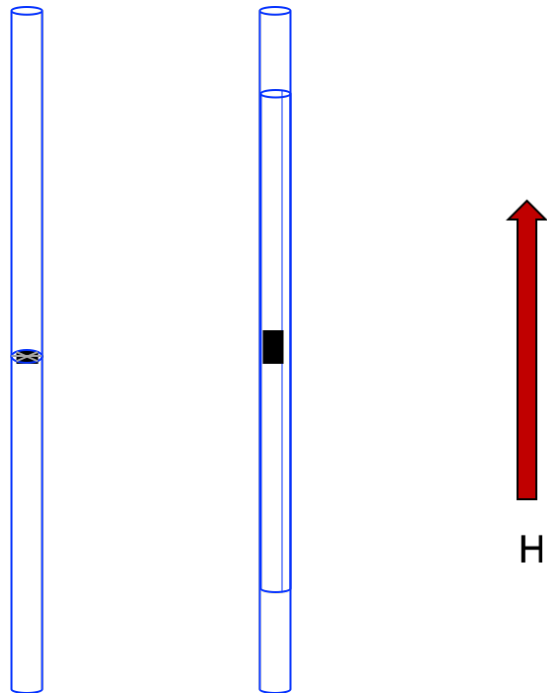


Figure 2.4. Left: Illustration of a sample mounted for measurement of magnetic response perpendicular to the film surface. Right: Illustration of a sample mounted for measurement of magnetic response parallel to the film surface.

After mounting, samples are inserted into the sample chamber, which is then purged of air and the atmosphere replaced with a low pressure of He gas. Samples are mounted as close to the center of the straw as possible, but after insertion into the sample chamber, the location with respect to the detection coil is checked by applying a magnetic field and measuring a curve like the one shown in Fig. 2.3. The physical location of the sample is adjusted based on this measurement so that it lies in the center of the detection coil. This centering may vary with temperature due to thermal expansion of the straw, but the MPMS has an auto-tracking feature to help adjust for these drifts. After the position is adjusted, the sample is ready for measurement. Because the response is assumed to be that of a uniform dipole, samples that are too large mounted in the in-plane orientation may fail to fit well. Samples in the out of plane orientation are constrained by the size of the straw. Small signals are also harder to fit properly due to the decreasing signal to noise ratio, so there are often measurement artifacts when the magnetization of the system passes through zero.

2.2.3 Magneto-Optical Microscopy

Theory of operation

Magneto-optical Kerr effect (MOKE) microscopy is a magnetic imaging technique that takes advantage of the Kerr effect; when polarized light is incident on a magnetic medium, the reflected light will experience a rotation of the polarization [61]. The Kerr effect occurs in multiple orientations: polar, transverse, and longitudinal. Each of these has a different angle of incident light and is sensitive to magnetization in a different direction. Polar MOKE is sensitive to perpendicular magnetization, with light incident perpendicular to the sample surface. Transverse and longitudinal MOKE are sensitive to different orientations of in-plane magnetization and use obliquely incident light. Our microscopy set up uses polar MOKE to study perpendicular features, so in further discussions, MOKE is taken to mean polar MOKE.

The Kerr effect is a type of magnetic circular dichroism, a difference in the absorption and transmission of left and right circularly polarized light when incident on a magnetic material. It is most easily observed using linearly polarized light, which is a combination of left and right circularly polarized light. Incident light

is an electromagnetic wave, and thus can excite electrons in the material. These electrons pick up a transverse motion due to local magnetic fields, which results in a rotation of the polarization direction relative to the incident light. The overall Kerr angle includes both the Kerr rotation and ellipticity and is described by the equation

$$\Phi_K = \theta_K + i\eta_K \quad (2.1)$$

θ_K is the Kerr rotation and η_K is the Kerr ellipticity. Because light is an electromagnetic wave, this equation is governed by Maxwell's equations and can be solved for using the Fresnel equations. This is a rather complicated process, and the solutions are only meaningful if one knows the magnetic susceptibility tensor describing the material. Multilayer samples have additional complications in that they require taking into account the behavior of each layer as a separate term. It is useful in some cases to find analytical expected values for Kerr rotation and ellipticity to compare to experiment to understand material properties. In our case, however, it is sufficient to know that the Kerr rotation will cause opposite rotations of polarization with up and down magnetized material and that in an appropriately designed system this will result in a resolvable intensity difference between up and down magnetized regions.

To resolve this difference, we use MOKE microscopy, a polarization-preserving bright field microscopy technique. Using a high intensity, incoherent light source, the beam is carefully modulated to provide Kohler illumination. This is a technique of defocusing the light on the sample to provide as uniform as possible of illumination over the field of view. The beam is reduced through a series of optics to the size of the opening in the objective lens and then polarized. It passes through a beam splitter and the objective lens. Reflected light is passed through a second polarizer, commonly referred to as the analyzer, and then captured using a CCD camera. The captured images are saved and analyzed. A schematic of this experimental set up is given in Fig. 2.5. Detailed descriptions of the equipment, along with considerations for reducing backgrounds and noise, are included in the following section.

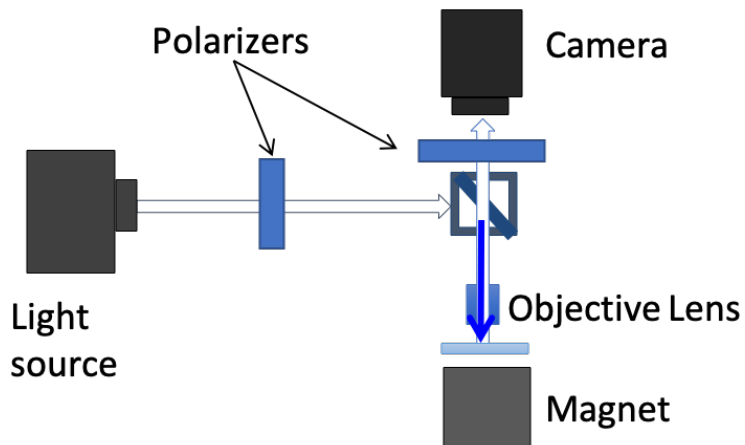


Figure 2.5. A simplified schematic representation of the optical set up used for MOKE microscopy.

Microscope components

As MOKE microscopy is a bright field microscopy technique, the choice of light source is important for producing repeatable, high quality Kerr images. Common light sources for MOKE include arc lamp sources, laser sources, and LED sources. There are many factors that affect the best choice of light source for a given experiment. We use a 75 W Xe arc lamp designed for high stability and low variation in intensity, which is a common problem with other arc lamp sources. This particular bulb is designed so that the arc point does not wander over the life of the bulb.

The next set of components is the optics used to reduce and collimate the beam. In collimated light, rays are parallel so there is minimal spread as the beam propagates. At its source, the beam is 3.5 cm in diameter and needs to be reduced so that the entire beam fits through the 5 mm polarizer and on to the back of the objective lens. This is accomplished with a series of commercially purchased lens pairs, optimized by the manufacturer to reduce aberrations and leave the beam well collimated. Apertures are also used near beam foci to control the beam width and quality. A photograph of the optics used to set up the beam is shown in Fig. 2.6. The yellow arrows show the path of the beam from the light source to the polarizer. The image on the right gives a clearer view of the lens pairs and apertures leading to the polarizer.

Once the beam is reduced and collimated, it passes through the first polarizer.

Our microscope uses Glan-Thompson calcite polarizers, which filter p-polarized light and transmit s-polarized light. They have reasonably high damage thresholds ($>1\text{W}/\text{cm}^2$), but we include a neutral density filter in our optical set up to avoid damage to the polarizer by the high-intensity light source. Glan-Thompson polarizers have a wide transmitted field, making them a natural choice for imaging applications [62].

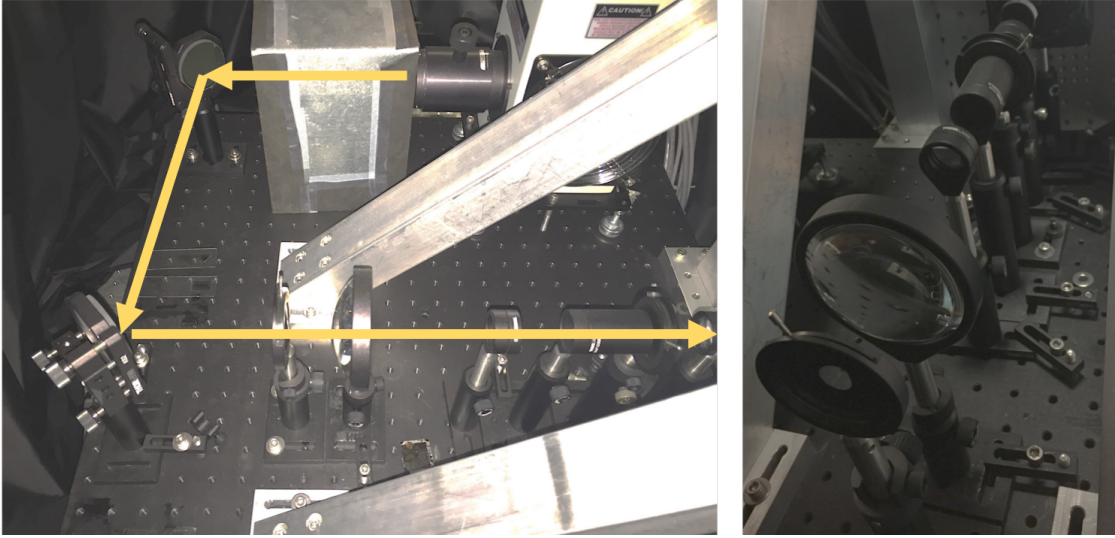


Figure 2.6. Photograph of the initial optical path of our microscopy set up. The yellow arrows show the path of the beam from the light source through the optics used to initialize the beam. The right image shows a clearer picture of the apertures and lens pairs used to reduce and collimate the beam.

Once it is polarized, the light is ready to illuminate the sample through the objective lens. The choice of objective lens is crucial in determining image quality and spatial resolution, as well as the strength of the magnetic contrast. Most commercial lenses are infinity corrected, which means they accept collimated light as an input. We use a 100x oil immersion lens, which uses a thin layer of oil rather than air as the medium between the objective lens and the sample. An oil immersion lens has a higher numerical aperture (NA) than air immersion lens since oil has a higher index of refraction than air. The NA is a physical property of an objective lens and is related to the maximum spatial resolution by the Rayleigh criterion:

$$R = .61 \frac{\lambda}{NA} \quad (2.2)$$

So a higher NA leads to a smaller spatial resolution. This equation is indicative of a fundamental limit imposed by diffraction. Our objective lens has an NA of 1.3, giving a lower limit on the spatial resolution of 190 - 330 nm over the visible wavelength range (400 - 700 nm). This is sufficient to resolve our 400 nm diameter features. The actual spatial resolution achieved depends on the size and quality of the beam entering the objective. In addition to increasing the numerical aperture of the objective to provide the necessary spatial resolution, oil immersion lenses have also been shown to have increased the Kerr intensity when compared to an air immersion lens [63].

After the light reflected from the sample passes back through the objective lens it must pass through the analyzing polarizer. The polarization angle of this polarizer determines the domain contrast in captured images. For light reflected from a non-magnetic material, setting the analyzer angle perpendicular to the original polarization angle renders the beam extinct. With a magnetic material, the angle of extinction is slightly off of cross polarization, at the Kerr rotation angle. Both the Kerr intensity and the background intensity are increased by increasing the analyzer angle. The ideal angle that maximizes Kerr contrast depends on many experimental parameters and is determined empirically. We find the ideal angle by measuring the domain contrast in a magnetic film at multiple analyzer angles and selecting the angle with the highest contrast for continued measurements. In our microscope, the analyzer angle is set to 11° .

The final piece of equipment in our Kerr microscope is the CCD (charge capture device) camera used to capture images. A CCD consists of a semiconductor grid in which incident photons are converted into electrons, and the accumulated charge of each pixel in the grid is then read out and used to digitize the image in the computer. We use a full-frame CCD camera with a temporal resolution of tens of frames per second. There are several potential sources of noise in the image capture process: photon noise, dark noise and read noise are all different types of noise that come from failures to accurately convert photons to electrons in the CCD, build up of thermally generated electrons in the CCD, or statistical variations in reading the signal respectively. Some of this noise can be reduced by taking multiple images and averaging them together, creating a more accurate image of the sample. There are other types of noise in the system that are not from the camera, including vibrational noise. High frequency vibrations may blur feature edges when using an

averaging technique. This vibrational noise is limited by building the microscope on a “floating” optical table with equipment on overhead racks and using sandbags or other vibrational dampeners where possible to limit the coupling of vibrations between different components in the system. Some noise reduces over time as the system mechanically relaxes after physical adjustments; it can take several months for the system to mechanically relax and reduce the high frequency noise. We balance the exposure time and the number of images averaged to maximize the signal while minimizing noise. The objective, analyzer, and camera are pictured in Fig. 2.7.

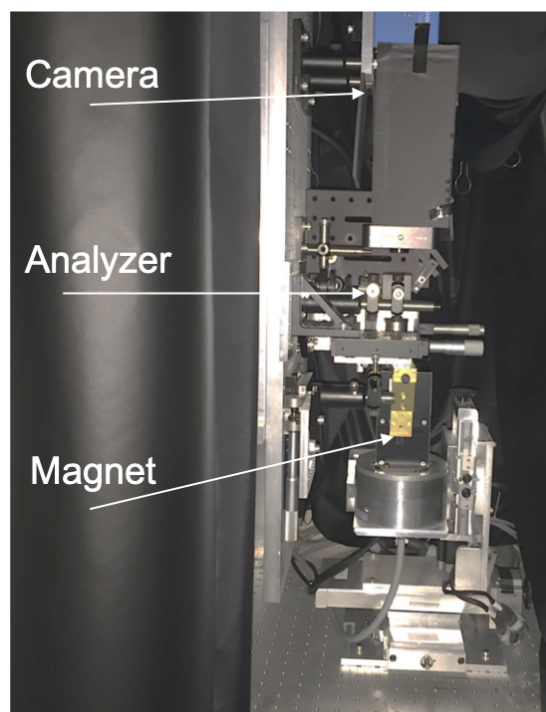


Figure 2.7. Photograph of the MOKE microscopy set up after the initial polarizer. Image includes the objective lens, analyzing polarizer, CCD camera, and projected field magnet.

One last component also pictured in Fig. 2.7 is an electromagnet. This is not part of the optical path, but it is an important part of the MOKE microscopy set up. The magnet is the external stimulus used to probe the magnetic response of our samples. We use a water-cooled GMW 5201 projected field magnet, so called because the magnetic field is projected from the magnet with perpendicular and parallel fields available depending on the relative position of the sample to the magnet poles.

In this dissertation, we use only the perpendicular component of the field, but the magnet is mounted on a stage capable of moving the magnet to change the field orientation without remounting the sample. For future measurements, studies using in-plane field components are of interest. The magnet has a maximum perpendicular applied field of .25 T. When measurements are carried out in the presence of an applied magnetic field, Faraday rotation in the objective lens introduces a linear background into the measurements. Faraday rotation is an effect similar to Kerr rotation but in transmission rather than reflection. This background can be reduced by measuring in zero field, but for some measurements, it is undesirable to remove the external field between field steps.

2.3 Computational Methods

The hardware and physical measurement process are the starting place for MOKE microscopy, but another critical part of this experiment is the ability to extract useful information from the images collected. This requires sophisticated image processing, which we have developed in-house specifically for the projects we are pursuing. There are separate protocols for processing images of multi-domain mesoscopic features to study the transition to single domain islands and for artificial spin ice arrays. More details are given in Appendix B, along with reference [57].

2.3.1 Mesoscopic Features

For the mesoscopic feature analysis, the relevant image analysis requires isolating each feature and locating the domains and domain walls throughout a switching process. All images requiring domain analysis are taken in zero magnetic field, so we needn't worry about the linear background from Faraday rotation. The only image processing required on images acquired in an external field is isolating the features. Because the Pt/Co features are quite reflective compared to the Si substrate, and the features are spaced far apart, it is straightforward to isolate the features in each image using commercially available algorithms. Once the features are isolated, finding the precise locations of domains and domain walls is a more complicated process. The first step is to convert the image from grayscale to binary. We begin by subtracting a background obtained by averaging together images in both saturated

magnetic states to remove intensity variations from non-magnetic backgrounds. In the background subtracted images, any non-magnetic material has a value that fluctuates due to noise but is centered around zero, and any magnetic material has a nonzero value based on its magnetic state. In theory, in the area that has been isolated as corresponding to a magnetic feature, any positive value should indicate an upward pointing magnetic moment and any negative value should indicate a downward pointing moment. Because the Kerr contrast is small on the order of the background intensity however, zero is not a sufficiently precise cutoff value. Instead of setting the cutoff at zero, we find the maximum and minimum values of the image and use their average as the threshold that separates magnetization oriented up from magnetization oriented down. This lessens noise due to intensity variations throughout a run. We set a limit on the intensity values through which the cutoff can reasonably vary, chosen empirically. Because the islands are not driven to a fully saturated state, and because the allowed fluctuation is constrained to minimize the impact of extreme outliers, this procedure robustly produces accurate binary equivalent images. See Fig. 2.8 to see a partially switched image and its binary equivalent.

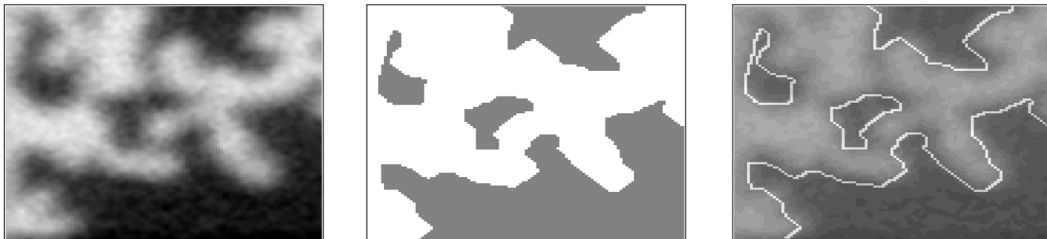


Figure 2.8. The first panel shows a background subtracted image of an isolated feature in a multi-domain state. The second panel shows the equivalent binary image, and the third shows the locations of the domain walls extracted from the binary image and overlaid on the original image.

Once a feature has been converted to binary, domain walls are found as the edges between up and down domains. The locations of these domain walls are overlaid on the original image to visually check for accuracy (See Fig. 2.8). Other values can also be calculated from the binary images, such as the fraction of switching that has occurred on the edge of a feature and the consistency of nucleation sites between multiple runs on the same feature. The net magnetization and domain wall length are extracted from these images throughout a measurement and used for further

calculations as well. All additional calculations are relatively straightforward so long as the image has been accurately converted to binary.

2.3.2 Find Locations and Datastreams

For artificial spin ice arrays, finding the location of each feature (which in this system we refer to as an island) is less straightforward. The islands are still bright compared to the Si substrate but they are close enough together that they are difficult to resolve with commercially available feature finding algorithms, even though by eye they appear quite distinct. The analysis procedure described here is used for large arrays of varying geometries; experiments on smaller patches of islands require significant adjustments to this procedure. We begin the analysis by subtracting a complete image of the bare Si substrate taken with identical parameters to our experimental image (exposure time, applied magnetic field, etc). This removes the global background due to inhomogeneity in the beam profile. We illuminate the sample as uniformly as possible, but in reality, there is always some amount of non-uniformity in the beam profile. To accurately find the location of each island, we then consider the image as a series of horizontal and vertical slices, the thickness of which is a tunable parameter in the algorithm. Using a peak finding algorithm on the intensity each slice generates a 2D map of potential island locations. We set a threshold distance and say that potential islands within that distance from one another must actually be two instances of the same island, and find a new set of potential islands by averaging these duplicates together. Finally, knowing that the background is not very reflective, we set a minimum intensity value for a potential object to be considered an island. This robustly generates a complete mapping of all of the islands in the array and requires no prior knowledge or assumptions about the geometry or spacing of those islands. Occasionally due to image quality, some islands are erroneously filtered out of the analysis, or locations outside of the array are mistakenly identified as islands.

In addition to finding the island locations in the initial image, we must also take in to account lateral drifts of the array throughout a measurement cycle. Any vibrational noise can cause lateral motion of the sample throughout the measurement, and even a single pixel value of lateral drift can affect the remainder of the analysis process. We need not go through the entire location finding algorithm

presented above for each image in the array. Instead, we isolate a small number of islands in the center of the array and find their locations in each image. This allows us to find the relative change in the position of the islands in this subset at each image in the data run. Because the relative positions of islands within the array are fixed, finding the lateral drift of a subset of islands is sufficient to find the lateral drift of the entire array.

We are also interested in comparing the behavior of specific islands between separate runs, which requires a way to accurately index the locations for run-to-run comparisons. To make these comparisons, we use the locations found in all relevant runs to create a master list of locations, using a similar procedure to the removal of duplicate islands described above. The locations for each run are overlaid and then islands within a certain distance are taken to correspond to the same physical island and their locations are averaged together. The final set of averaged locations is used for subsequent analysis. This overlay process is also helpful for runs that did not find all islands in the array in the initial location analysis. As long as an island is found in at least one data run, it will appear in the final mask. This technique allows for a higher acceptable failure rate in the initial location finding program.

With the indexed locations and drifts throughout a run, we now have the location of every island in every image throughout a data collection run. From this point, the image data is converted to numerical data to continue analysis. A bounding box is selected around the center of each island in each image. The intensity values of all pixels within the box are averaged together to give an intensity value for the island, which when tracked through a data collection run is referred to as a datastream. The process of generating datastreams is not dependent on the type of data run, but subsequent analysis differs based on sweep type. Example datastreams for different types of measurements are shown in Figs. 2.9 and 2.10.

2.3.3 Adjustments for Py Underlayers

For samples with arrays deposited on top of a layer of Py, there is a critical difference in the location finding procedure described above. The Py film is significantly more reflective than the Si substrate. This makes it so the program is unable to accurately filter out extraneous locations that do not correspond to real islands. We account for this by providing a secondary step after the initial location finding to

tell the program where we think the array is located and filter out all islands outside of that region. Also, there are additional issues with the larger lattice spacings of hexagonal and kagome geometries, which are created by systematically removing islands from a triangular geometry. Because of the reflectivity of the Py, these geometries tend to erroneously find islands in the spaces where the islands have been removed from a triangular geometry, in particular in regions of the array that are initially more brightly illuminated. This is typically no more than a quarter of the full array area, and usually much less. It is difficult to systematically filter out these extra locations. We take two different approaches, choosing the most accurate approach on a sample to sample basis. First, we use a spatially localized intensity filter. While the Py is more reflective than the Si, it is still less reflective than the Pt/Co. The intensity variations across an entire array are too large to distinguish the Py from the Pt/Co, but if we restrict the filter to a small portion of the array it can for some samples accurately remove potential island locations that correspond to locations on Py rather than Pt/Co. If this method fails, we simply restrict our analysis to a portion of the array that did not include extraneous locations in the list of found islands. We have performed checks on complete arrays that removing the amount and location of islands corresponding to the regions including extraneous islands does not significantly affect the global parameters calculated for the array. Finally, for some of the smaller lattice spacing arrays on Py, the reflectivity makes it difficult to find accurate locations in the most brightly illuminated sections of the array and ends up averaging together potential locations from two separate islands as one island. This produces locations that fall between actual island locations. This only occurs in a small section of the array, which is excluded from further analysis.

2.3.4 Hysteresis Analysis

One of the two main field sweep protocols used to understand the properties of artificial spin ice is a hysteresis loop, described in Chapter 1. Analysis for this type of data assumes each island switches in a single field step and only once in each field sweep direction. Therefore, by finding a switching field for each island we can describe the entire microstate of the array at any point in the hysteresis process. Naïvely, one might think that this field could be found by simply taking a

derivative of each island's datastream, but this is not a sufficiently robust method given the signal to noise ratio of our measurements.

To accurately and repeatably find the switching fields, we start by selecting a subsection of islands from the center of the array to serve as a comparison set. An image of the datastream of a target island from a Squ 800 array, whose switching field we are attempting to measure, is shown in blue in the top panel of Fig. 2.9. The datastreams of the comparison islands are shown in this figure in red. We subtract the datastream of the target island with each of the islands in the target set. This takes into account the effects of intensity fluctuations and drifts that occur uniformly throughout the data run. These curves are then differentiated as shown in the second panel of Fig. 2.9. Because each island's hysteresis loop has approximately the same slope and the same global backgrounds, the subtracted value of the two curves is approximately constant except at the field either the target or comparison island switches, where it is a step function. So, each differentiated curve is approximately zero except at the switching fields. One particular comparison curve is highlighted in blue to make this easier to see. The final step in finding the switching field is to take the absolute value of the differentiated curves and sum them. Each curve contains a peak from the target island at the same field and a peak from the comparison island at some other field. So the summation should have a large peak at the switching field of the target island, as shown in the final panel of Fig. 2.9. We find the locations of these peaks to find the switching field of each island.

This analysis is reasonably robust but does not always find a reliable switching field for every island in an array. Islands for which this analysis fails are re-analyzed using a secondary algorithm in which a linear fit is carried out to the high field data for both positive and negative fields. An island is considered to have switched when it transitions from being closer to the linear fit from one side to being closer to the linear fit from the other side. This is a less robust algorithm but gives a reasonable switching field for islands that failed the initial analysis.

Finally, switching field distributions are offset to be centered at zero. Changing the fabrication parameters, the geometry, or the lattice spacing of the array being considered will change the overall coercivity. It is easier to make comparisons with switching field distributions offset to be centered at zero. At this point, we have converted all visual information about the state of the array through the hysteresis

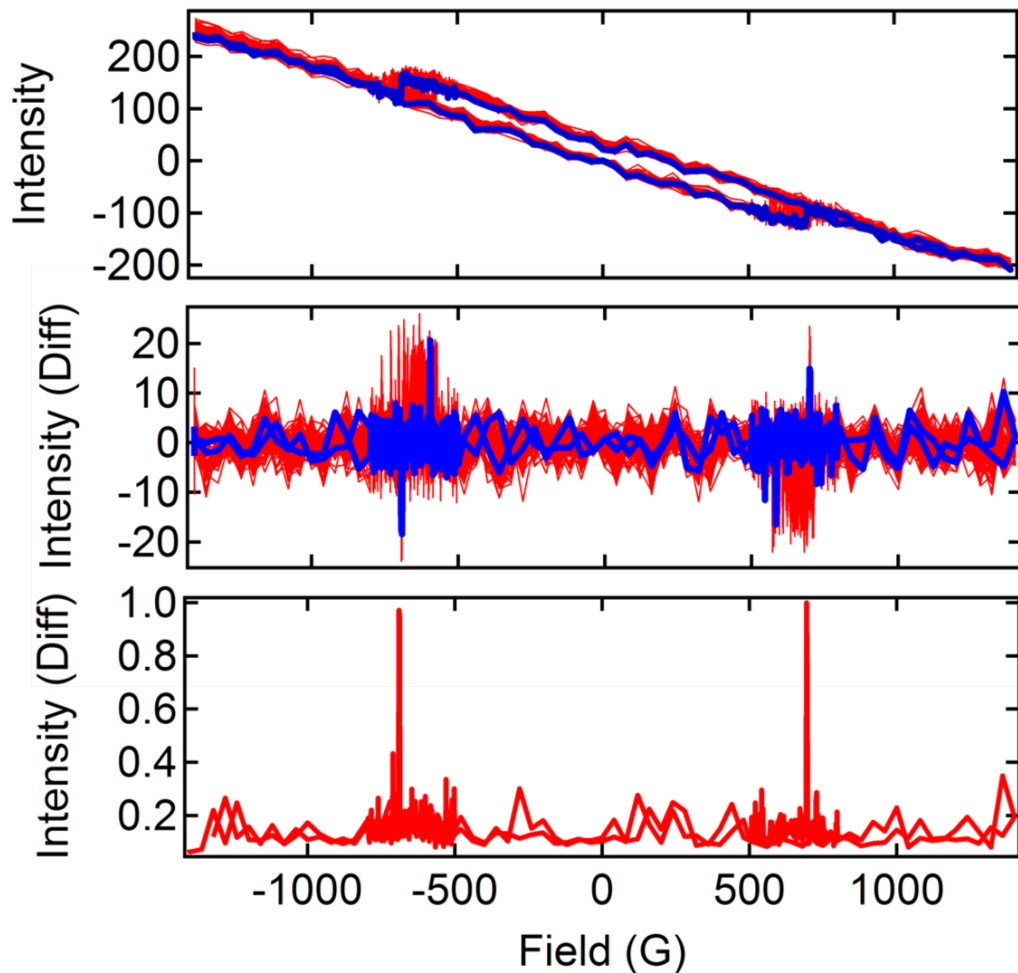


Figure 2.9. Top panel: Hysteresis loops for target (blue) and comparison (red) islands offset so that the intensity at zero field is zero. Middle panel: Derivatives of the difference between the target and comparison islands, with one curve highlighted in blue for visual clarity. Bottom panel: The sum of the absolute value of the curves in the middle panel. This data was taken on an 800 nm spacing square array

cycle into a simple database of island locations and switching fields. Further analysis involves straightforward numerical calculations using this information.

2.3.5 Demagnetized Array Analysis

The other major field sweep protocol we use is designed to put an array into a low energy state, by applying magnetic fields of alternating sign and decreasing magnitude. This is commonly referred to as a demagnetization protocol because

ideally, the low energy state should have no net magnetic moment. Islands will continually switch to align with the applied field until the field is no longer large enough to coerce them. As the field magnitude decreases, eventually the entire array reaches a stable state. Datastreams obtained using this type of sequence are qualitatively different from datastreams from hysteresis measurements (See Fig. 2.10).

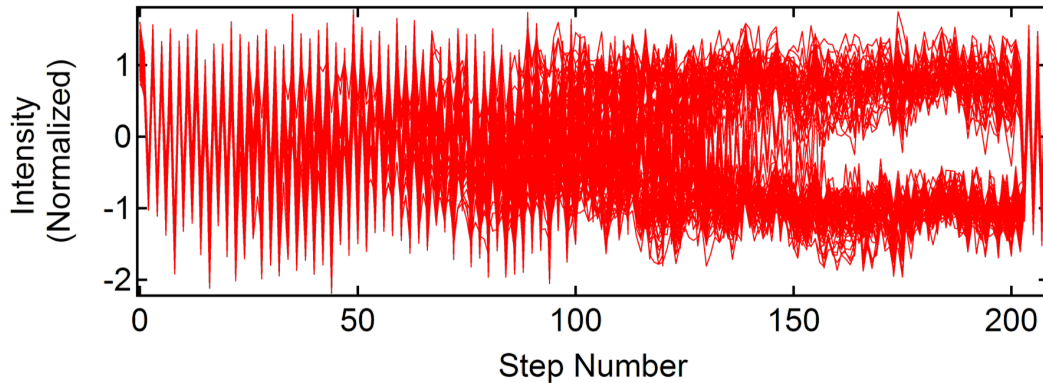


Figure 2.10. Normalized intensity as a function of field step for islands experiencing an oscillating demagnetization protocol. 100 islands out of an 800 nm lattice spacing square array are included in this graph.

These datastreams can be analyzed to track the magnetic state throughout the demagnetization process, but this is a non-trivial process. In this dissertation, we restrict our analysis to the final state achieved by an array through a demagnetization process. Images taken during a demagnetization protocol are collected in zero applied field, so there is no linear background. However, the overall intensity of each island varies due to inhomogeneity in the beam profile. Datastreams are first normalized using the high field data, where the applied field is sufficiently high that we know in a positive field every island will be in an upward magnetic state and in a negative field every island will be in a downward state. Several up values and several down values are averaged together and used to offset and scale the datastream such that when the island is oriented up it a value of around 1, and when oriented down it has a value of around -1. After the initial region where the islands all follow the applied field, there is a switching region where islands may or may not switch with every field step. Analysis of this region is not included in this discussion. Next, there is a stable region, where changing the field is no longer sufficient to coerce islands to switch and the array is fixed in its demagnetized state.

Finally, there is an ending saturation region, used both for image processing and for helping with datastream normalization.

Analysis is carried out by averaging the intensity of normalized datastreams for each island over several field steps in the stable region, and histograms are generated of this data. For arrays in which analysis is considered successful, the histogram has two distinct populations, one centered close to 1 and the other close to -1. The population centers are not perfect due to drifts in intensity throughout data collection, so much like the mesoscopic image conversion to binary, a more robust threshold than zero is required for accurate analysis. The two peaks are fit to Gaussian functions, and each island is assigned to the distribution in which it is likely to fall. If the distributions are too wide or too close together and islands cannot be reasonably assigned to one of the distributions, these islands are marked as questionable and excluded from further analysis. An example of the histograms generated during this process is shown in Fig. 2.11. Again, once each island has been assigned a location and a magnetic state, all further analysis is carried out by numerical calculations using this data.

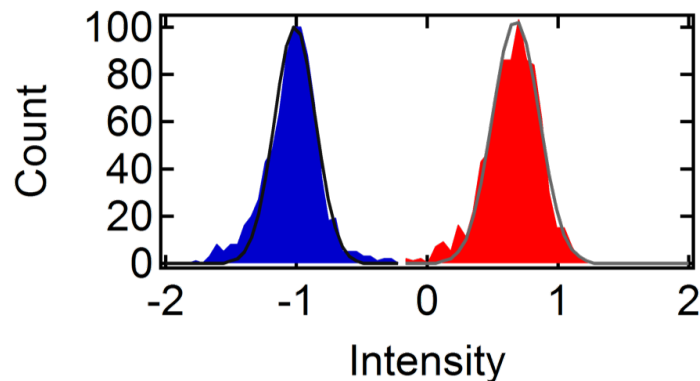


Figure 2.11. Histogram showing the averaged intensity of populations of up (red) and down (blue) islands in a demagnetized state of a square array.

The final saturation region, in addition to providing more accurate normalization, is used to create clear images of the demagnetized states. While arrays tend to undergo lateral drifts throughout a data run, there is very little lateral drift between two adjacent frames and the saturated image can be used as a background to be subtracted from the adjacent demagnetized image. This gives a clear image of the magnetic state of each island. These subtracted images are used for Fourier

analysis and for finding the demagnetized states of small patches.

Chapter 3 | Transition to Single Domain Structures

Note: a significant portion of this chapter is taken from reference [64]. This project was funded by the US Department of Energy, Office of Basic Energy Sciences, Materials Sciences and Engineering Division under Grant No. DE-SC0010778.

3.1 Introduction

In Chapter 1, I introduced the concept of using patterned magnetic thin films as artificial model systems. In this chapter, I will explore in detail the transition of a perpendicular magnetic anisotropy thin film through the mesoscopic regime and into the nanopatterned state that we will use for the artificial systems discussed in the next chapter. This project was an exploration of the physics of domain walls in confined structures, in addition to verifying that our artificial spin ice islands are the proper size to behave as Ising spins.

Magnetic domain wall motion is has been of interest both fundamentally and for application purposes. With contemporary desires for minimizing the size scale of technologies, understanding the influence of decreasing feature on size domain wall motion is a necessary step before designing useful applications. Materials with strong perpendicular magnetic anisotropy (PMA) are of particular interest because they have narrow domain walls which can be efficiently moved [65]. Domain wall motion in thin, effectively 2-dimensional, films of PMA material has been studied extensively [66–68]. PMA materials have also been patterned into nanowires to study the quasi-1-dimensional motion of domain walls [69–72], or patterned

into nanodots and used as Ising-like spins in modeling studies, behaving as 0D features [8,32,33]. In this chapter, we study 2-dimensional patterned squares in sizes that span the transition from quasi-infinite films to 0D nanodots, to qualitatively and quantitatively investigate the nature of this transition.

Domain walls have a material dependent, characteristic width determined by the magnetic exchange stiffness (A) and anisotropy (K) of the material, $\delta \propto \sqrt{A/K}$. Due to energy considerations, the minimum size of feature that can energetically support a domain wall is larger than this characteristic width. Ferromagnetic systems break into domains to lower the demagnetization energy of the system. However, the creation of a domain wall increases the exchange energy of the system. As the feature size is decreased, the overall demagnetization energy of the system is also decreased, until eventually, the possible reduction in demagnetization energy cannot outweigh the increase of exchange energy. This indicates that there is some size regime where the demagnetization energy and exchange energy have similar contributions. Below this size, features are constrained to exhibit single domain behavior, with magnetic reversal that appears instantaneous on the timescales of our experiment rather than domain nucleation and propagation.

In addition to this static consideration of domain walls, there are also dynamic considerations. In thin film ferromagnetic systems, domain walls can be treated as one-dimensional elastic interfaces moving in a 2D pinning potential. [66] The strength of the external field used to move the domain walls determines not only the velocity at which they move but also the qualitative regime of the motion. If the applied field is much smaller than the depinning field (H_d), the domain wall motion occurs by jumps between local energy minima rather than continuous motion. Domain walls often follow similar paths over multiple distinct runs, since the path is determined by the physical positions of pinning sites. [73] Multilayer samples such as those used in this chapter have contributions to disorder and pinning sites from each interface; and increased levels of pinning and disorder lead to fractal domain shapes [69, 74, 75] and affect domain wall velocity [76–78]. Patterning the magnetic film into a nanowire introduces additional pinning sites due to the edge roughness [69], which adds another set of constraints to the domain wall motion. Some papers seem to indicate very little influence of patterning on domain wall velocity [70] while others indicate that there is a decrease of velocity and an increase in effective pinning field as the width of the wire is decreased (which increases the

relative contribution of the edge) [69]. It is unclear what effect the increase in edge influence will have if the domain wall is not constrained to move along an edge.

In this chapter, we studied both hysteresis loops and domain wall propagation in the thermally activated (or creep) regime for square PMA features ranging in size (s) from 10 μm to 400 nm, spaced $> 5 \mu\text{m}$ apart to minimize interactions between neighboring features. These squares were patterned as described in Chapter 1, using e-beam lithography with a bilayer PMMA/PMGI resist stack and a standard lift-off technique. Films were deposited using DC sputtering, and SQUID measurements for Pt/Co films are shown in Chapter 1. The mesoscopic feature samples were codeposited with sample 2.

The sample quality was verified using SEM, which shows that the samples lifted off cleanly and that the feature sizes match the intended sizes designed in the e-beam patterns. SEM images also verify that the film quality and edge roughness are consistent across samples of different sizes. This is important because if samples of different sizes have substantially different edge profiles, it is impossible to say if any trends in the data are due to finite size effects or simply effects of edge roughness. Partial SEM images of various size features, adjusted so each partial image is on the same scale, are shown in Fig. 3.1.

Optical measurements were carried out using an optimized polar magneto-optical Kerr effect (pMOKE) microscopy apparatus with a nominal resolution of ~ 300 nm, described in Chapter 2. As our microscope field of view is around 50 μm by 50 μm , there are multiple features within the field of view of our microscope. In pMOKE images, the magnetization of the sample is proportional to the intensity of the captured image. Hysteresis loops were measured by sweeping the magnetic field from -800 G to 800 G and back, using fine steps of 2 G in the switching region (150 G to 450 G) and coarse steps of 40 G elsewhere, and images were captured in the presence of an applied field. Domain wall propagation measurements were carried out by first nucleating domains with a magnetic field pulse (~ 1 s) at a field greater than the coercive field. Since the coercive field varies with feature size, the applied nucleation field was also varied. Also, we chose to consistently nucleate approximately 10% of the feature, which for different size features meant nucleating different absolute areas. This choice gave us a significant initial domain but also space into which the domain could be expanded using additional field pulses. Pulse times were adjusted based on the applied field so that features neither switched

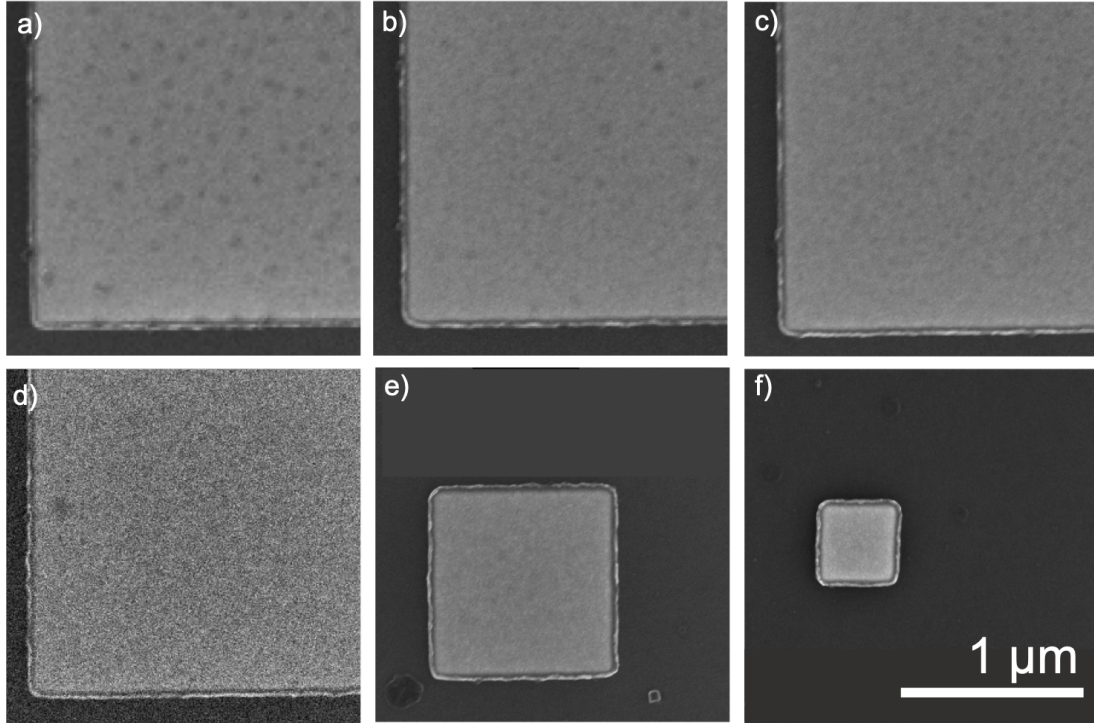


Figure 3.1. SEM images showing the lift-off quality and edge roughness profile of patterns square features with sizes of a) $10\ \mu\text{m}$ b) $5\ \mu\text{m}$ c) $3.75\ \mu\text{m}$ d) $2\ \mu\text{m}$ e) $1\ \mu\text{m}$ and f) $0.5\ \mu\text{m}$

fully within the first 3-5 images nor stayed in metastable states for more than a few pulses. Pulse times ranged from 100 ms to 1 s, with fields between 245 and 345 measured in 10 G steps.

3.2 Hysteresis

We use the hysteresis data to pinpoint the transition region from domain wall nucleation and propagation to seemingly instantaneous rotation. Hysteresis data is analyzed for both entire images and individual features therein, so features within an image are isolated as part of the analysis process. The magnetic film is significantly more reflective than the non-magnetic substrate, so it is straightforward to isolate the bright locations that correspond to features. Average intensity values are found by averaging all pixels in an image or all pixels identified as corresponding to a feature location. Once intensity values are extracted from images, we subtract a linear background correction to correct for Faraday rotation in the objective lens

and normalize the data. Normalized data is differentiated and fit to a Gaussian function to determine the width of the switching region, $\frac{dM}{dH} = Ae^{-\frac{(H-H_c)^2}{2\sigma^2}}$. Here H_c is the coercive field, and σ represents the width of the switching. If a feature switches in too few field steps, it is impossible to fit the derivative accurately. In this case, we still find the switching field from the derivative but set the width to a constant value that is below our measurement threshold. We chose 5 G for this value.

From the hysteresis data (Fig. 3.2), we observe a qualitative change in behavior as the features decrease in size. In this figure, red curves correspond to the average intensity of isolated features and blue curves correspond to the average intensity of the entire field of view. Larger features, when isolated, switch indistinguishably from one another or from the switching of the entire field of view. Features become increasingly distinct as the size is decreased, showing sharper switching over a range of fields. To quantitatively ascertain the transition region, we consider σ_I (from the entire image), σ_F (from the isolated features), and the standard deviation of H_c (SD) of all features in an image. If the features switch by domain nucleation and propagation with minimal effect from the boundary, we expect $\sigma_I \approx \sigma_F$ and $SD \approx 0$. If the features switch as single domain rotations, we expect $\sigma_I \approx SD$, and $\sigma_F \approx 0$. The data show this transition with onset by $s = 2 \mu\text{m}$ and completed by $s = 500 \text{ nm}$.

As the features are decreased in size, the average coercive field and the onset field of switching decrease. The simplest mathematical representation of a perpendicular magnetic system has a Hamiltonian of $H = -J \sum s_i s_j - \mu B \sum s_i$, representing the magnetization as Ising-like spins and taking into account Heisenberg exchange and the external field. The demagnetization energy is also a significant factor in this system, but in the simplest approximation serves as a modification of the external field so we disregard it for now. To understand how changing the size of the systems changes the impact of the external field, we consider what external field is necessary to overcome the exchange energy for systems of different sizes with nucleated domains of a fixed size. In other words, we consider the point where the external field energy is equal to the exchange energy. Setting the Hamiltonian to zero and rearranging the terms gives $B = -\frac{J}{\mu_B} \frac{\sum s_i s_j}{\sum s_i}$. In this ratio, the denominator is determined by the magnetization and the numerator is determined the domain wall length, both normalized to the area. Since we have fixed the size of the

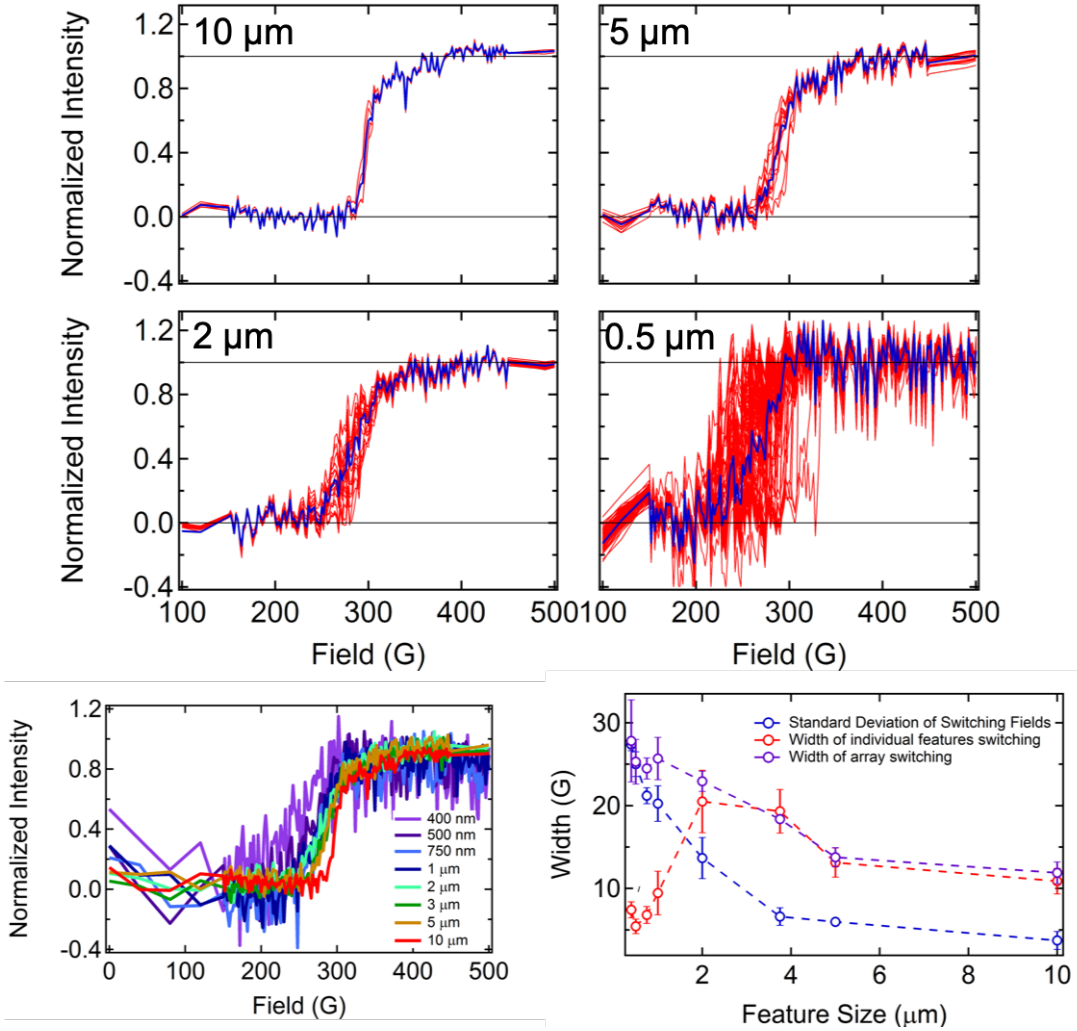


Figure 3.2. The change in the hysteresis of an ensemble of square magnetic features of different sizes a) $10\ \mu\text{m}$ b) $5\ \mu\text{m}$ c) $2\ \mu\text{m}$ d) $.5\ \mu\text{m}$ for both the isolated features in each set (red) and the average of the entire field of view (blue). e) The magnetic switching behavior for arrays of different size features ranging from $s = 10\ \mu\text{m}$ to $400\ \text{nm}$. f) Parameters from fitting the derivatives of the data shown in a-d to a Gaussian distribution.

nucleated domain, the numerator will increase with decreasing feature size as the perimeter of a square and the denominator will increase as the area of a square. So the overall, the ratio decreases. From this argument, it is reasonable that as the features become smaller, they nucleate at lower fields. While this agrees with our data, the demagnetization energy has not been included in the calculation, and the motion of the domain wall through the complicated 2D pinning potential is not

covered at all by this treatment.

3.3 Domain Wall Propagation

The increase in switching width as the feature size is decreased is likely contributed to by the change in the switching field. Domain walls propagate more slowly in lower applied fields, which would lead to wider switching ranges at lower fields since the field sweep rate is held constant. To accurately compare the domain wall motion between different sizes of features, we use domain wall propagation measurements. Domain wall propagation analysis requires significant image processing, as it is insufficient to know the average magnetization. We still begin by isolating the magnetic features in each image. We also average together an image of the magnetization in a saturated “up” state and an image in the saturated “down” state and use this as a background to remove non-magnetic contributions to image intensity. Background subtracted images are converted to binary domain images, with magnetization up and down represented by white and black respectively. These binary images give us precise locations of domains and domain walls and allow us to quantify the domain area a , the domain wall length l , and the proportion of switching that occurs along the edge. We analyze sequential images to calculate the additional parameters $a' = da/dt$ and $l' = dl/dt$.

To gain a qualitative understanding of the pinning potential experienced by domain walls, we use the domain wall propagation data to visual the average switching path (Fig. 3.3). This figure shows the top left feature visible in each image, but other features display similar behavior. We use the binary domain images to generate these composite images, correcting for the effects of lateral shifts between runs to precisely overlay features from 50 individual runs. Images are taken from a variety of applied fields but are chosen such that the magnetization in the feature is the same in all of the overlaid images. These composite images range in value from 0 to 50, with the intensity representing how likely a given area of the feature was to switch over the course of 50 runs, which allows us to visualize a potential energy map of the feature. Variations in the pinning potential determine the path of switching. These pinning variations are likely due to physical differences in film quality throughout the feature, such as changes in surface roughness or other fabrication defects [79].

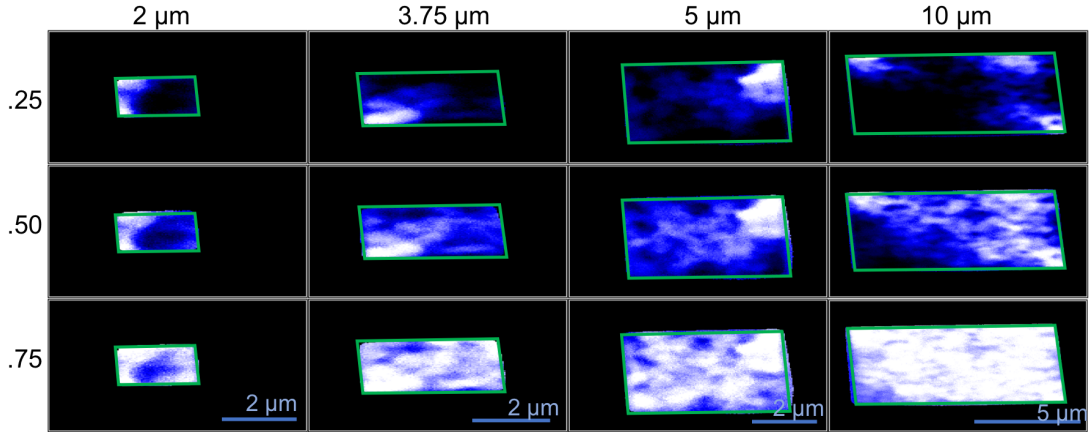


Figure 3.3. The composite filling data at 25%, 50%, and 75% switched over a total of 50 runs for 2 μm , 3.75 μm , 5 μm and 10 μm features. White areas switched every run and black areas switched no runs, with blue scale between.

Composite images help us visualize the 2D pinning potential experienced by domain walls and also confirm the complicated, fractal nature of domains in our multilayer film. As these are highly disordered domain walls, we cannot simply measure domain wall velocity by a change in domain wall position with time as you might for an isolated domain wall propagating down a wire or for a smoothly expanding bubble. To study the domain wall velocity in fractal domains, we use the following equation [78, 80]:

$$v = \frac{(a' - \frac{r_0 l'}{2})}{l - \pi r_0} \quad (3.1)$$

with a , a' , l , and l' as the previously introduced parameters we extract from binary domain images. r_0 represents the size of a nucleated domain, which is below our resolution limit. Following other papers [80], we use a value of about half our minimum resolution for r_0 ; we use $r_0 = 150$ nm in our calculation. Because a , l , a' , and l' are all time dependent, we are able to use this equation to calculate the instantaneous velocity throughout the switching process. To compare data between different propagation fields, we need to convert the velocity from a function of time to a function of magnetization. Various sources of noise in the system, including physical sources such as vibration and analytical sources such as fluctuations in the extracted locations of the domain walls, affect this conversion. To convert this to a one-to-one function of velocity as a function of magnetization rather than time, we

average the velocity using bins of 1% of the area switched. Once we have calculated the velocity, we further analyze the domain wall propagation using the standard equation for domain wall velocity in the creep regime:

$$v = v_0 \exp \left[- \left(\frac{H_d}{H} \right)^{\frac{1}{4}} \left(\frac{U_d}{k_B T} \right) \right] \quad (3.2)$$

Here, v_0 is a normalization constant, H_d is the depinning field, U_d is the depinning energy, H is the applied field, and T is the temperature. In our measurements, H is the only variable parameter. By rearranging this equation slightly, we see that $\ln(v)$ is a linear function of $H^{\frac{1}{4}}$. The slope of this function gives us the effective critical field, $H^{\text{eff}} = \left(\frac{U_d}{k_B T} \right)^4 H_d$, which gives us the strength of the pinning potential.

We first note that the calculated domain wall velocity is more similar for features of different sizes at the same magnetization than it is for features of the same size at different magnetizations (Fig. 3.4a). As the magnetization is increased, the domain wall velocity decreases (Fig. 3.4c). This is likely not a result of energetics but rather of statistics: as the feature fills in there are fewer local minima to transition to so the rate of switching decreases. There could also be a stabilizing effect from the demagnetizing interactions between neighboring domains. A similar effect is observed, although less clearly, in the hysteresis data. In the hysteresis curves for larger features, there is a fast switching regime followed by a slow tail as the system saturates. This suggests that the energy required to annihilate the domain walls in this system is greater than the pinning energy, causing both the tail at the end of the hysteresis and the decreasing velocity as a function of filling.

While the velocity itself does not change significantly as a function of feature size for the field range considered, the analysis of the velocity using Eqn. 3.2 indicates that H^{eff} decreases as the size of the features decreases. The data in Fig. 3.4b is artificially offset to more clearly show the difference in the raw data, that the slope is decreasing with decreasing feature size. The data in Fig. 3.4d shows the values of H^{eff} extracted from these fits. H^{eff} is considered as a function of the reciprocal of the feature width, comparable to previous studies on domain walls in nanowires. This reveals that as the feature size is decreased, the energy barrier to domain wall motion is also decreased, opposite to what was observed in nanowires of varying width [69]. This is not concerning, as the motion of a domain wall down a wire has different physical constraints than the switching of our two-dimensional

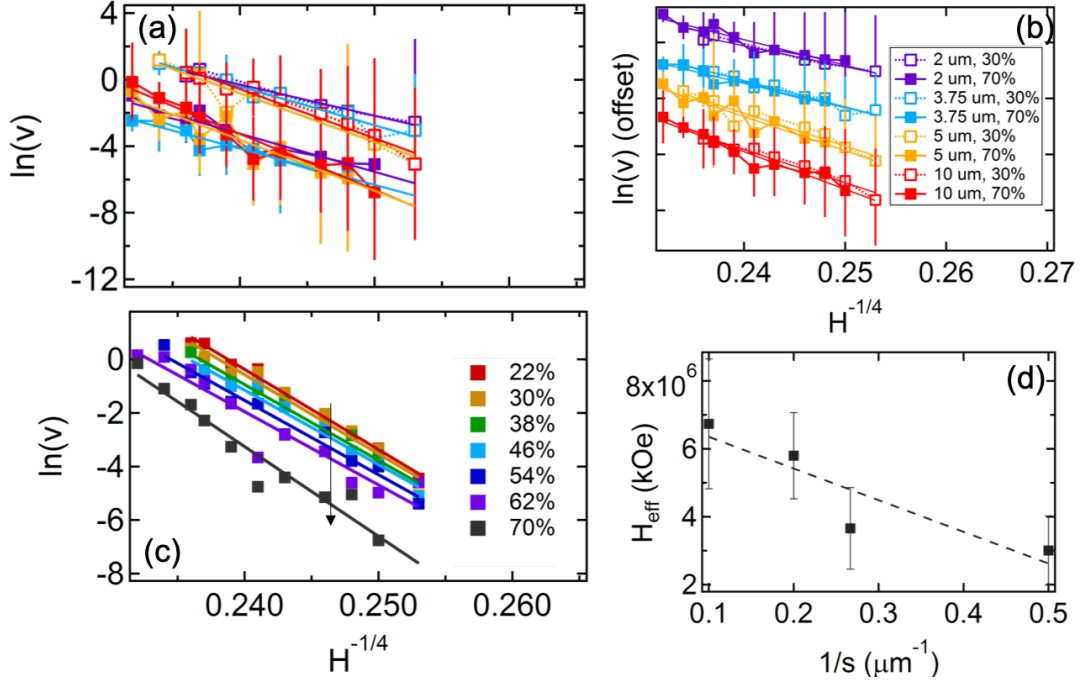


Figure 3.4. a) The instantaneous domain wall propagation information for $s = 10 \mu\text{m}$, $5 \mu\text{m}$, $3.75 \mu\text{m}$, and $2 \mu\text{m}$ features, at 30% filling and 70% filling, colored by feature size. b) The same data, artificially offset to show the difference in slope between the four sizes, and the similarity in slope within a particular size. c) The instantaneous domain wall propagation for the $10 \mu\text{m}$ sample, colored by area switched at the moment the velocity was calculated. The arrow represents the progression of increasing filling percent. d) The average effective pinning potential from linear fits to the velocity of different-sized features plotted against the reciprocal feature size

features. To understand the qualitative source of this difference, we return to the pinning potential maps in Fig. 3.3.

From these images, we observe that nucleation always takes place on the edge of a feature. For larger features, the switching then tends to penetrate from the nucleation site to the interior of the feature. Conversely, for smaller features, the switching tends to occur more along the edges. To quantify this, we measure the percent of the edge that has switched as a function of the overall magnetization of the feature. Again, measured data is a function of time and is averaged in bins of 1% to convert to a function of area and generate the curves shown in Fig. 3.5. The noise that is averaged to convert to a function of area as well as any run to run variations contribute to the error bars. However, the dominant contributor to the large error bars on this plot is most likely that multiple features of the

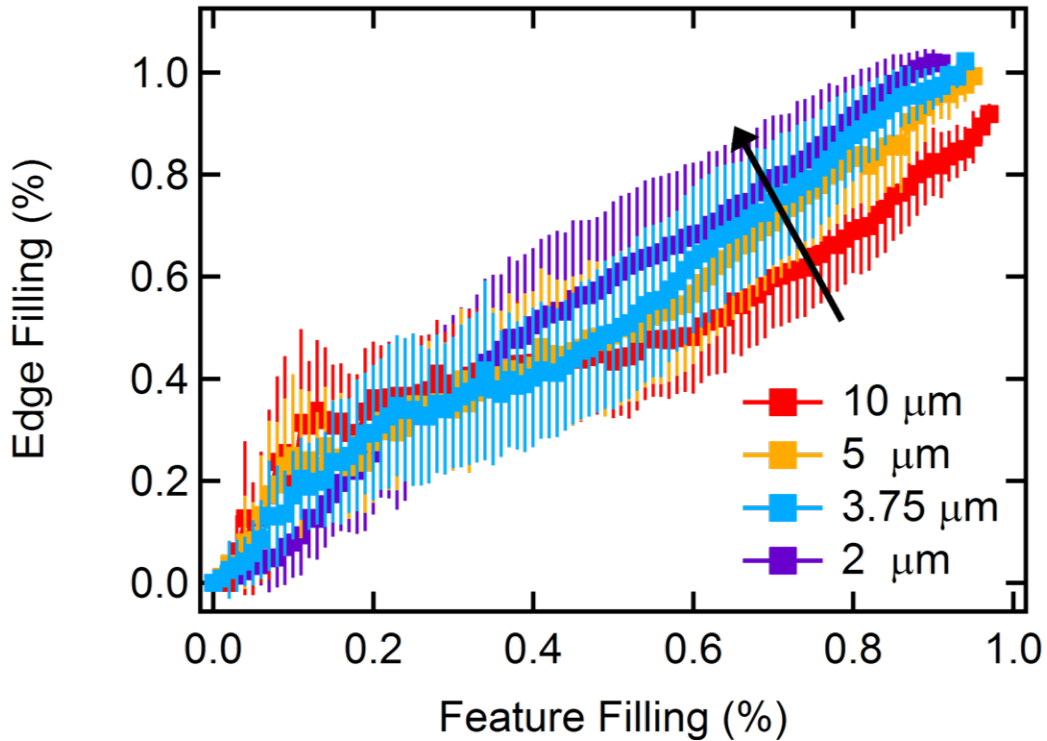


Figure 3.5. The average amount of the edge that has switched as a function of how much of the area has switched, for four different sizes of features. The arrow indicates the trend in edge switching as with decreasing feature size

same size are averaged together, each of which may have a different characteristic edge-to-area switching pattern. While the uncertainty in the data is large, there is still a discernible trend with feature size: as the size decreases, switching is more likely to occur on the feature edges.

For the larger features, the penetration could be caused by an increase of pinning energy at the edge of the feature, similar to the energy change observed in domain walls propagating down increasingly narrow wires. It could also be an effect of the demagnetizing field, which would favor domain penetration. The demagnetizing field is stronger in the center of the sample than toward the boundary, so domains that penetrate into the sample have a larger impact on the demagnetization energy than domains on the boundary. These domains help minimize the overall energy despite the exchange energy cost of the increase in domain wall length. As the features become smaller, the demagnetization field decreases due to the decrease in the amount of magnetic material, while the exchange energy cost of the domain

walls remains approximately the same. This is one possible mechanism by which switching is pushed toward the edges as the feature size is decreased. The decrease in H^{eff} as the feature size is decreased is related to these qualitative changes in the behavior at the edge. If the edge is easier to switch than the interior, as suggested by the nucleation always occurring along an edge, that would explain the decrease in effective pinning potential as the edge switching become more energetically favorable.

In conclusion, squares of perpendicular magnetic anisotropy material with disordered domain structures show a distinct decrease of domain wall velocity with increased magnetization as the features go through a switching process. As the system approaches the transition to single domain features, the domain switching is preferentially shifted to the feature boundaries. Also, the effective pinning potential decreases slightly with decreasing feature size, although in the field range considered the velocity itself does not vary significantly. The features completely undergo a transition to supporting only a single domain by a width of 500 nm, with an onset of about 2 μm . We can be confident then, that islands presented in the next chapter are in an Ising-like state.

Chapter 4 |

Perpendicular Artificial Spin Ice

Note: Sections of this chapter were taken from reference [1]. This project was funded by the US Department of Energy, Office of Basic Energy Sciences, Materials Sciences and Engineering Division under Grant No. DE-SC0010778.

4.1 Introduction

Islands smaller than the single domain transition described in the previous chapter are used as the constituent components to form perpendicular artificial spin ice arrays. We are interested in these arrays as a model system to study order and disorder in magnetic systems. First, I will present an investigation into the correlations and stochasticity during hysteresis of weakly interacting arrays. Then, I will explore one way to increase the interaction strength to study both demagnetized states and quasi-dynamic hysteresis in more strongly ordered samples.

4.2 Stochasticity and Correlations in Hysteresis

In Chapter 1, we introduced artificial spin ice as a model magnetic system. Most studies of the hysteresis loops of artificial spin ice systems focus on the *macrohistory* of an array, the development of the macrostate, characterized by aggregate quantities, which is reproducible from one field cycle to another. This includes the hysteresis curves themselves, equivalent to the raw distribution of switching fields, as well as local switching field distributions accounting for the magnetic fields produced by nearby islands, and the development of nearest-neighbor spin correlation as the average magnetization of the array varies through a field sweep. Interaction

between islands makes a significant and identifiable contribution to the width of the raw switching field distribution. In this dissertation, we also focus on the *microhistory* of an array, the evolution of its microstate during a field sweep, which is not reproducible from sweep to sweep. Although the energy scale of ambient temperature is very small compared to relevant magnetic energies in these systems, the origin of this stochasticity may be associated with thermal fluctuations that become significant near the coercive field.

The samples studied in this dissertation were patterned using electron beam lithography, with a standard liftoff of bilayer poly(methyl methacrylate)/ poly-methylglutarimide (PMMA/PMGI) resist stack as described in Chapter 2 and Appendix A. All samples considered contain frustrated (kagome and triangular) and non-frustrated (hexagonal and square) arrays, with lattice spacing ranges of 600 - 1000 nm (sample 1) or 500 - 800 nm (samples 2 – 5). The islands are 400 - 450 nm in diameter, as confirmed by scanning electron microscopy. Magnetic films of Ti(2 nm)/Pt(10 nm)/[Co(0.3 nm)/Pt(1 nm)]₈ were deposited using DC sputtering at Argonne National Lab. We used superconducting quantum interference device (SQUID) magnetometry to confirm the strong perpendicular magnetic anisotropy of these films, as well as to measure the saturation magnetization for each film. To confirm the magnetic characteristics of our arrays, we consider films of Pt/Co multilayers that were codeposited with the patterned substrates which should have identical magnetic characteristics to the corresponding arrays. There is a diamagnetic contribution from the substrate and sample mounting supplies, which is approximated as a linear fit to the data at high field and then subtracted as a background. The data shown here are after this background correction has been taken in to account. All measurements are carried out at 305 K. Hysteresis loops for films corresponding to samples 1 – 5 are shown in Fig. 4.1. Specific details on island size and magnetization properties for all samples considered are found in Table 4.1.

Data are collected using the MOKE microscopy set up described in Chapter 2. Using the image processing techniques previously described, we can resolve, *in situ*, the magnetization states of every island in an array as shown in Fig. 4.2, thereby obtaining the complete microhistory of the array during a field sweep. Since each island reverses magnetization only once during a field sweep, a microhistory α is encapsulated by the list of switching fields of the islands; the value of H_{app} at

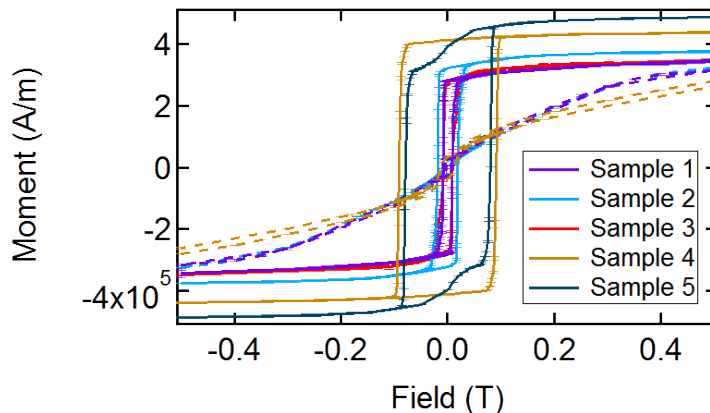


Figure 4.1. SQUID measurement of magnetization vs. magnetic field for out-of-plane (solid lines) and in-plane (dashed lines) orientations for the samples presented in this dissertation

	Diameter (nm)	M_s (A/m)	$B_0(500 \text{ nm})$ (G)	σ_d (G)	σ_h (G)	Avg. Overlap (%)
Sample 1	400	3.46×10^5	3.61	15.70	–	–
Sample 2	450	3.75×10^5	4.96	28.21	10.8 ± 1.8	87.7 ± 1.1
Sample 3	425	3.46×10^5	4.09	17.28	9.8 ± 0.9	84.3 ± 0.8
Sample 4	450	4.40×10^5	5.82	41.84	–	–
Sample 5	450	4.86×10^5	6.43	35.51	–	–

Table 4.1. Physical, magnetic, and statistical properties of five different artificial spin ice samples

which island i switches in sweep α is denoted h_i^α . Although we do not distinguish notationally, it is to be understood that up-sweeps and down-sweeps are treated separately, not combined in aggregate quantities or directly compared via correlation functions.

4.2.1 Macroscopic degeneracy

We begin with the run-to-run consistent, macroscopic (aggregate) aspects, starting with the switching field distribution and the contribution of island interactions thereto. The total field experienced by an island comprises not just the externally applied field H_{app} , but also a configuration-dependent contribution from other islands which broadens the distribution of observed (raw) switching fields. Without

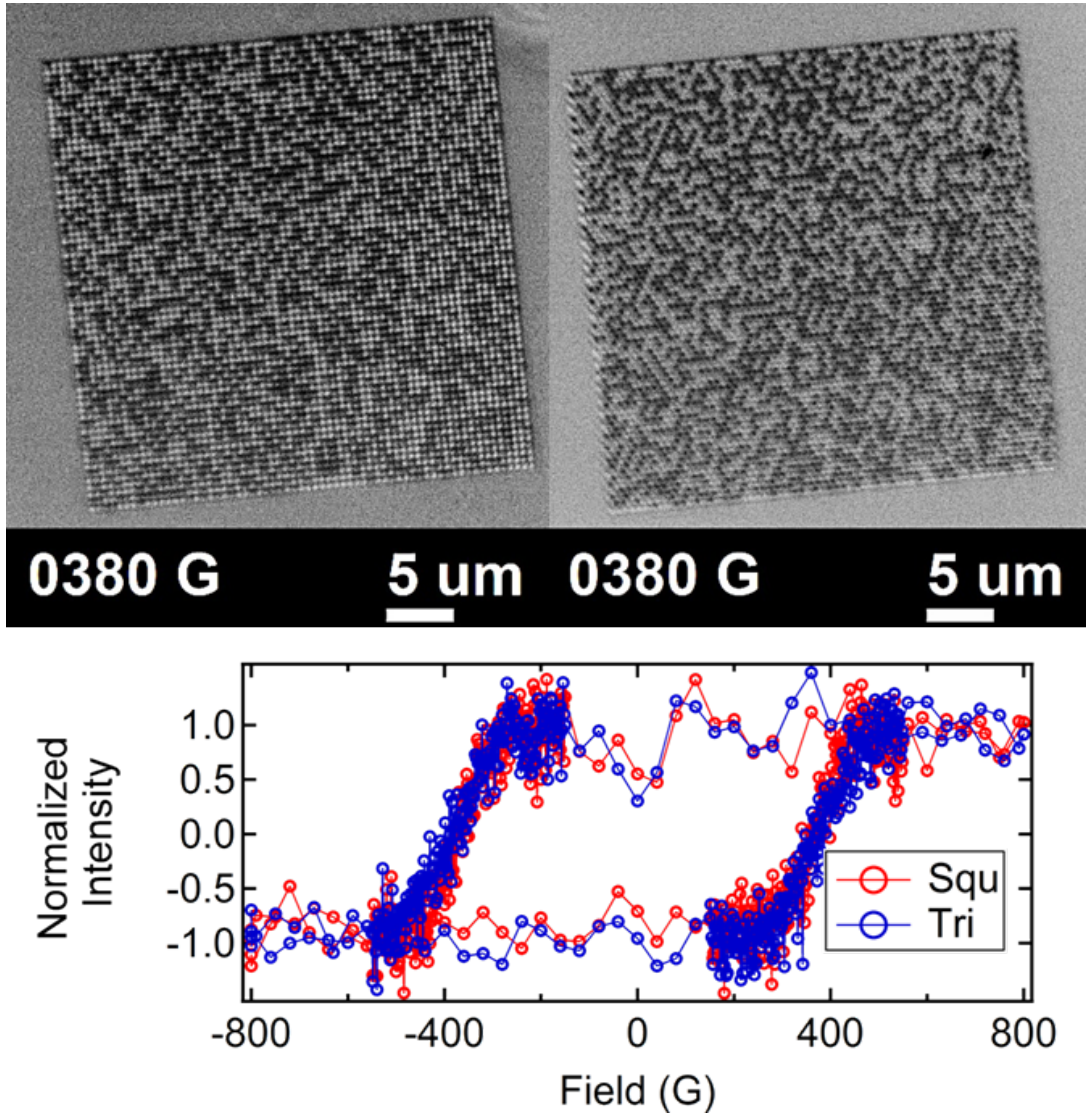


Figure 4.2. Top panel shows MOKE images recorded at 380 G in an increasing the field sweep, near the coercive field, for 500 nm lattice spacing square (left) and triangular (right) arrays from sample 2. The bottom panel shows normalized hysteresis loops recorded using imaging MOKE for these arrays with intensity averaged over the entire array area.

knowledge of the microstates the semi-empirical equation [33]

$$\sigma = AKB_0(L) + \sigma_d \quad (4.1)$$

allows the observed width of the switching field distribution to be separated into contributions of island interactions and static disorder, the latter presumably

introduced by the lithography process. Here, A is a constant, K is an effective coordination number, $B_0(L)$ is the dipolar field of an island on its nearest neighbor at lattice spacing L , and σ_d is the static disorder. We presume that the static disorder is introduced during the lithography process due to previous results from both experiments and modeling [27,28]. Furthermore, we do not separate disorder contributions from multiple sources of disorder because simulations on in-plane artificial spin ice systems indicate that the contribution of disorder to the ordering in an array is not dependent on the source of disorder, only on the magnitude. To further investigate the possibility that lithographic differences are a primary source of disorder in these samples, we consider SEM images. SEM images of islands from samples 2 and 5 are shown in Fig. 4.3. Comparing these images to the extracted disorder values listed in Table 4.1, we see a dramatic increase in disorder for sample 5 compared to sample 2, and also that sample 5 has a considerably less desirable edge profile than sample 2.

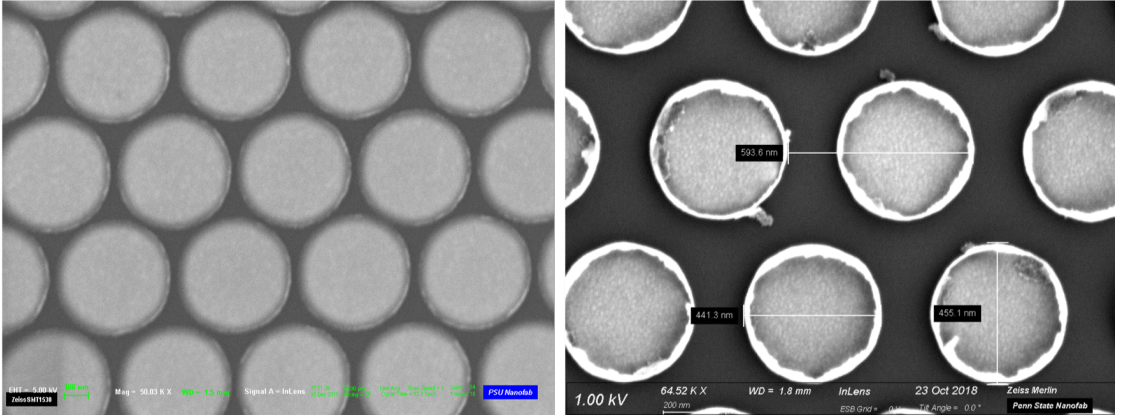


Figure 4.3. SEM images of samples 2 (left) and 5(right) showing the different edge profiles that might contribute to the different levels of disorder in these two samples.

Provided the microhistory, we can directly calculate the r -neighborhood-corrected switching field $h_{i,r} = H_{\text{app}} +$ (field from up-to- r^{th} neighbors) in point-dipole approximation, accounting precisely for both the internal and external fields felt by an island when it switches. In this enriched notation, the raw switching field for sweep α is denoted as $h_{i,0}^\alpha$.

The top panel of Fig. 4.4 shows the distributions of the r -neighborhood-corrected switching fields $h_{*,r}^\alpha$ for a single sweep for a 500 nm square array from sample 2 for $0 \leq r \leq 5$. These are the distributions of all aggregated islands, hence the ‘*’

subscript on h . The expected narrowing of the distribution as r increases (further-neighbor fields accounted for) is prominent. The lower panels of Fig. 4.4 show how the widths of the $h_{*,r}^\alpha$ distributions change with lattice spacing for different lattice types. The broadening in the raw ($h_{*,0}^\alpha$) distributions for different geometries is accounted for completely by the difference in effective coordination number. For each geometry, as r is increased, the width decreases, becomes independent of the lattice spacing, and approaches the calculated value of disorder. The magnitude of the decrease is on the order of $AKB_0(L)$, with K calculated considering r neighbors. This decrease agrees with Eqn. (4.1) and reduces to the static disorder contribution alone in the limit of large r . This behavior agrees with previous studies pointing to the significance of long-range interactions to the behavior of artificial spin ice [81]. The results in Fig. 4.4 were taken from sample 2; similar results are obtained for sample 3. The analysis supports the treatment of islands as interacting point dipoles, wherein an island's neighbors influence its switching behavior by supplementing the external field with their net dipolar field strength.

While the r -neighborhood-corrected switching field distributions demonstrate an influence of islands on one another, they say nothing quantitative about correlations. We turn to these next. The average spin (magnetization) in an array during sweep α is $\langle S_i^\alpha \rangle_i$. Subscripts on averaging brackets indicate what is averaged over, and each spin takes value $+1$ or -1 . $\langle S \rangle$ is a fairly reproducible function of external field (for the same sweep direction). For purposes of comparing different sweeps and different arrays, it is preferable to parametrize the macrohistory by magnetization $\langle S \rangle$ rather than the applied field; this will remove fluctuations due to finite size. Thus, the nearest-neighbor spin correlation for sweep α ,

$$\begin{aligned} C_S^\alpha(\langle S \rangle) &= \left\langle S_i^\alpha \right\rangle_i \left\langle S_j^\alpha \right\rangle_j - \left\langle S_i^\alpha S_j^\alpha \right\rangle_{\alpha; \text{NN}} \\ &= \langle S \rangle^2 - \langle S_i^\alpha S_j^\alpha \rangle_{\text{NN}} \end{aligned} \quad (4.2)$$

is regarded as a function of $\langle S \rangle$. The sum is over all nearest neighbor pairs (i, j) as indicated briefly by the NN subscript. C_S is zero if spins are independently assigned values $+1$ or -1 with probabilities consistent with $\langle S \rangle$, and we have chosen a sign convention such that it increases with the proportion of energetically preferred antiferromagnetic nearest-neighbor configurations.

C_S consists of two terms, one containing the information about alignment/anti-

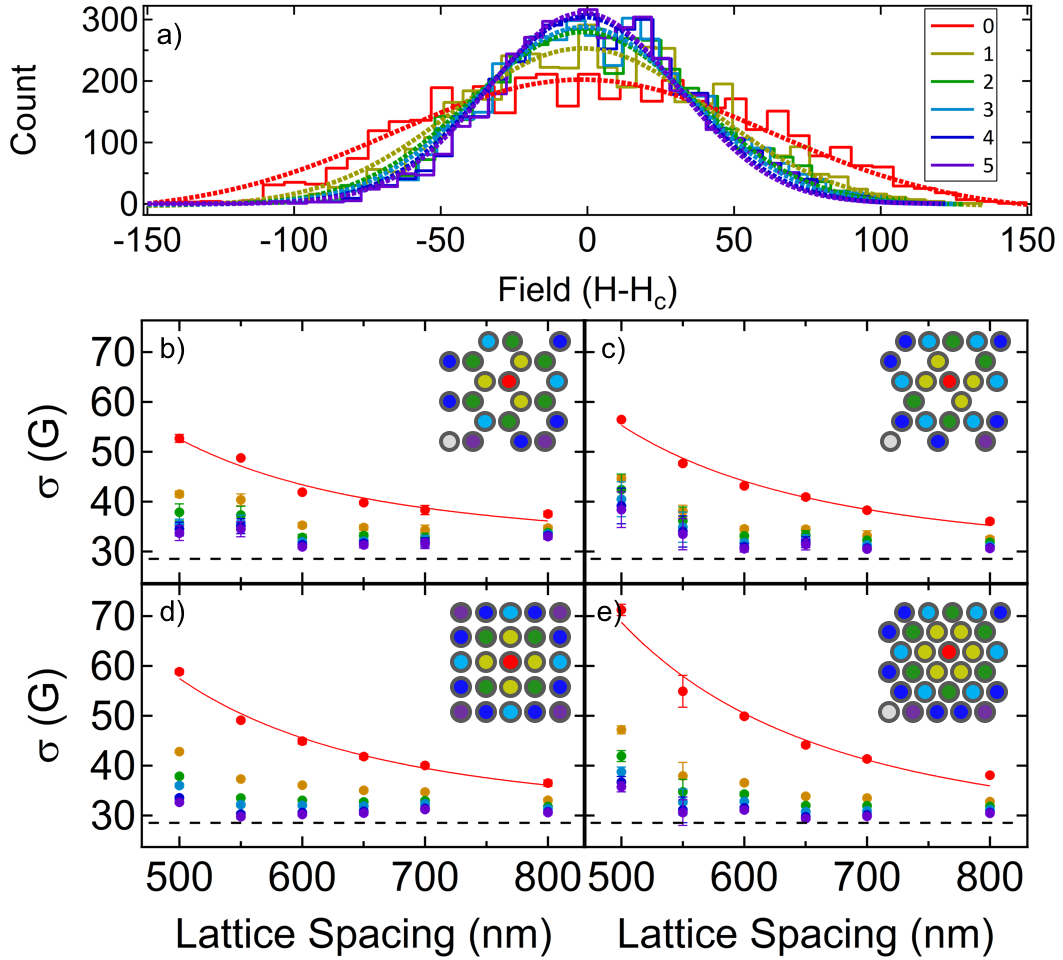


Figure 4.4. a) Switching field distribution and associated Gaussian fits, with switching fields calculated by removing dipolar effects from 0 (as measured) to 5 nearest neighbors for a 500 nm square array (Sample 2). Width of the Gaussian fits for b) hexagonal, c) kagome, d) square, and e) triangular as a function of lattice spacing taking into account increasing numbers of neighbors. Fits to Eqn. 4.1 are shown as red lines, and disorder values from these fits are shown as black dashed lines. The inset images show a cartoon of the lattice geometry colored by target island (red) and neighbor number to match the colors on the graphs. A full set of neighbors is shown up to third nearest neighbor, along with a partial set of fourth and fifth nearest neighbors.

alignment of neighbor pairs ($\langle S_i^\alpha S_j^\alpha \rangle$) and one containing a correction for the expected alignment due to non-zero magnetization ($\langle S \rangle^2$). These two components for a single sweep on a 500 nm square array from sample 2 are plotted separately for reference in Fig. 4.5 (top). The blue curve is the correction term and the red curve is the alignment term. The same alignment data is also shown reflected across the

y-axis to highlight the asymmetry. The curve obtained from subtracting these two curves (corresponding to C_S as we have defined it) is shown in Fig. 4.5 (bottom). Again, the solid and dashed curve are the same data reflected over the y-axis to demonstrate the asymmetry.

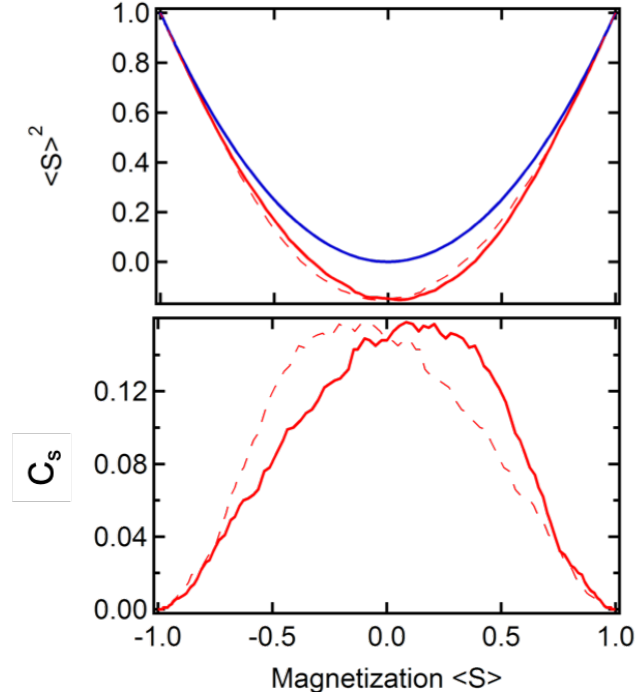


Figure 4.5. Top: The blue curve is a correction term for expected alignment at non-zero magnetization, and the red curve is the nearest neighbor alignment term for a 500 nm Squ array from sample 2. Dashed curve is a reflection of the solid red curve to show the asymmetry. Bottom: The subtraction of these two curves (C_S)

Fig. 4.6a,b show the evolution of $C_S^a(\langle S \rangle)$ for up-sweeps for the square and triangular arrays on sample 2. The correlation increases and then decreases as the sample transitions from a saturated state, through zero magnetization to the oppositely saturated state. However, the correlation does not peak at zero magnetization. Rather, it continues to increase for a while, peaking at an *offset* $\langle S \rangle$. This behavior indicates the importance of the quasi-dynamic switching path and the influence of island interactions on it. While the offsets are repeatable and observed in multiple samples, the data are too noisy to discern any clear trends in the values. We find the offsets by finding zeroes of the derivative of the quasi-dynamic correlation curve shown in Fig. 4.6. Due to the noise in the

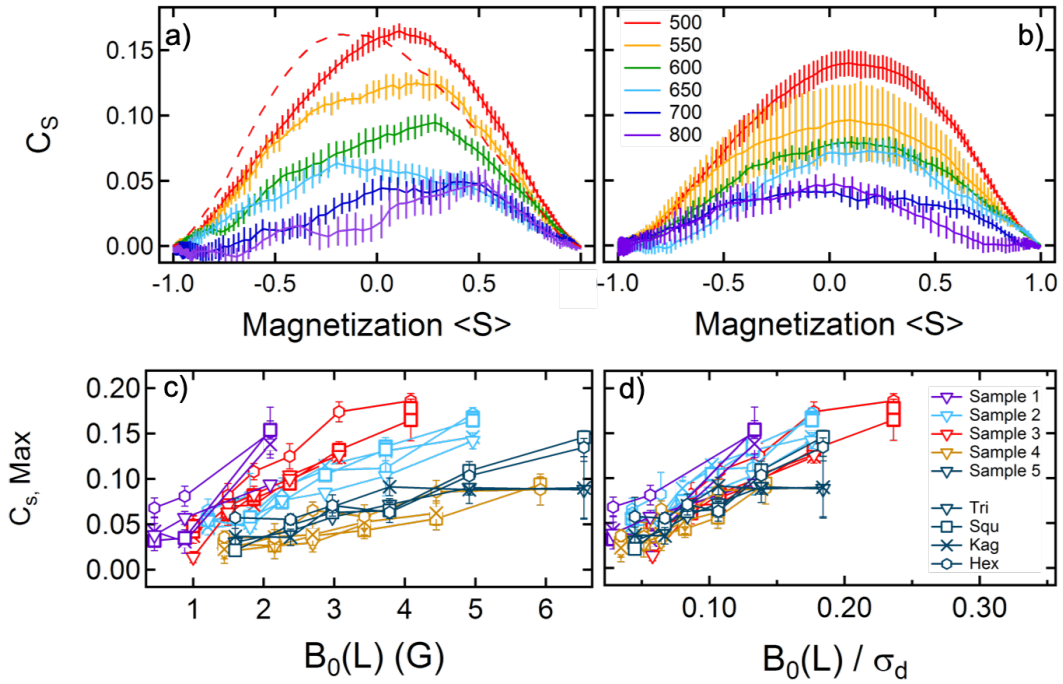


Figure 4.6. Plots of $C_S(\langle S \rangle)$ for various lattice spacings of a) square, and b) triangular arrays from sample 2, for increasing values of applied field. The dashed line in panel a shows $C_S(\langle S \rangle)$ as the field is decreased to more clearly illustrate the asymmetry. Panel c) shows the maximum value of correlation as a function of the dipolar field of an island on its nearest neighbor (i.e. the interaction strength) for samples 1 – 5. Panel d) shows the same data as a function of the dipolar field scaled by the measured disorder in the system.

experimental data, however, it is better to carry out a curve fit to the correlation curve than to attempt to take a derivative of this data. We begin by fitting the curves to the polynomial function $f(x) = -(x + 1)^2(x - 1)^2(a + bx + cx^2)$. This function contains the constraint that the correlation and its derivative must go to zero at the endpoints of the hysteresis loop. There are three free parameters to describe the correlation. An example of this fit a correlation curve from a Squ 500 array from sample 3 is shown in Fig. 4.7. The fitting coefficients give us the functional form of the derivative. The derivatives for the Tri arrays from sample 3 are shown in the right panel of Fig. 4.7. We apply a root finding algorithm to these derivatives, using appropriate logical constraints to choose the appropriate zero if there are multiple possible zeros. Calculated offsets for samples 1 – 3 are shown in Fig. 4.8. The fits become noisy and less accurate as the interaction strength is

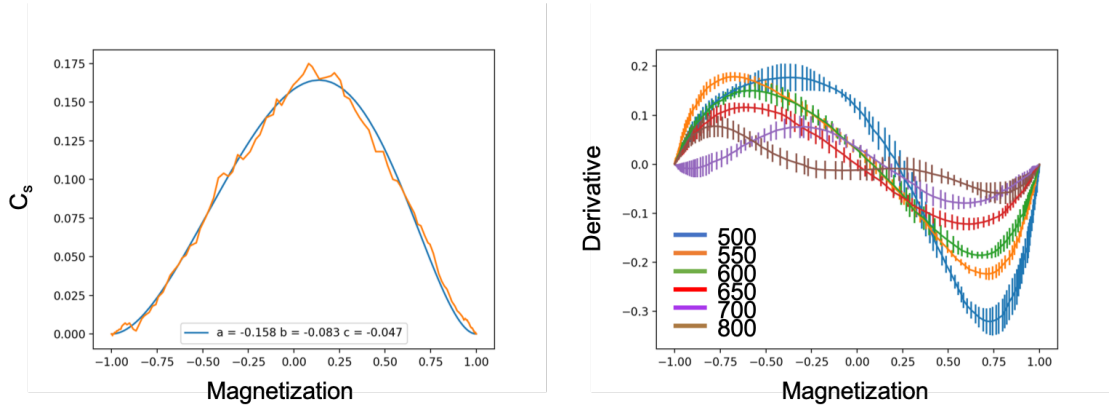


Figure 4.7. Left: Correlation curve and associated functional fit from one run of a Squ 500 array. Right: Calculated derivatives for multiple lattice spacings of triangular arrays from sample 3.

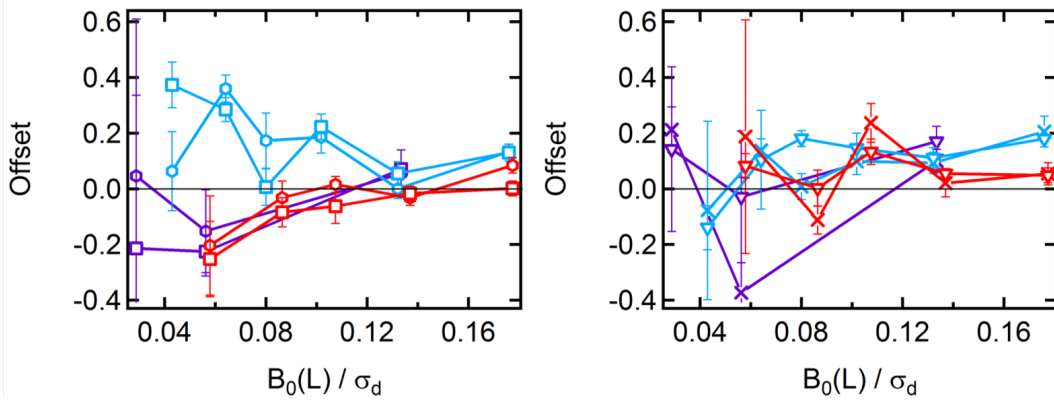


Figure 4.8. Offsets calculated using the zeroes of the derivatives for left: unfrustrated and right: frustrated arrays from samples 1 – 3.

decreased, leading to the large error bars at low interaction strengths.

One anticipates that the maximum value of nearest-neighbor antiferromagnetic correlation will increase with the strength of interactions, $B_0(L)$. Fig 4.6c shows that this expectation is borne out and that the dependence is roughly linear. Data for samples 1 – 5 are plotted in different colors. For each sample, the maximum value of $C_S(\langle S \rangle)$ is consistent among all geometries, indicating that the interactions are not sufficiently strong for the distinction between frustrated and unfrustrated geometry to manifest in the macrostate. However, there is distinct variation in the correlations between samples, indicating that interaction strength is an insufficient parameter to characterize these systems. Using instead the dimensionless ratio $B_0(L)/\sigma_d$ of

interaction strength to static disorder as the independent variable, a significant, albeit partial, data collapse is obtained, as shown in Fig. 4.6d. Quite reasonably, local ordering is enhanced by increasing interaction strength and hampered by increasing static disorder.

4.2.2 Microstructure variation

Data and analyses discussed to this point show that the systems are macroscopically determinate, in that the histories of the global quantities $\langle S \rangle$ and C_S , as well as distributions of switching fields $h_{i,0}$ and $h_{i,r}$, are very similar run-to-run. A perfectly deterministic system, though, would have a reproducible *microhistory*, following exactly the same sequence of island switchings each time it is subjected to the same external field sweep. Run-to-run variations were studied in depth for samples 1 – 3, but this analysis was not carried out on samples 4 – 5 as they were fabricated for a different part of the project. Possibly the simplest quantification of irreproducibility is the run-to-run switching field variance

$$\sigma_h^2 = \left\langle \left(h_i^\alpha - \bar{h}_i \right)^2 \right\rangle_{i,\alpha}, \quad (4.3)$$

where

$$\bar{h}_i = \langle h_i^\beta \rangle_\beta \quad (4.4)$$

is the run-averaged switching field of island i . The average in Eqn. (4.3) is over islands in the array and multiple (7 – 10) macroscopically identical hysteresis loops.

The run to run variance of a single array can best be visualized by considering the comparison of h_i^α to \bar{h}_i^α . This is shown for a 500 nm spacing (red) and 800 nm spacing (blue) Squ array from sample 3 in Fig. 4.9. The 500 nm data fills a larger range on the x-axis because it has a wider switching field distribution due to broadening from interactions. The 500 nm data is also broader in the vertical direction, indicating a larger run to run variance, which is also due to interactions.

In contrast to the *aggregate* switching field distributions displayed in Fig. 4.4, the run-to-run variance inherently involves an average over runs and involves subtraction of an *island-dependent* mean. Table 4.1 reports average values across all geometries of the run-to-run switching field standard deviation (the square root of the variance) σ_h for samples 2 and 3 at lattice spacings above 650 nm, of

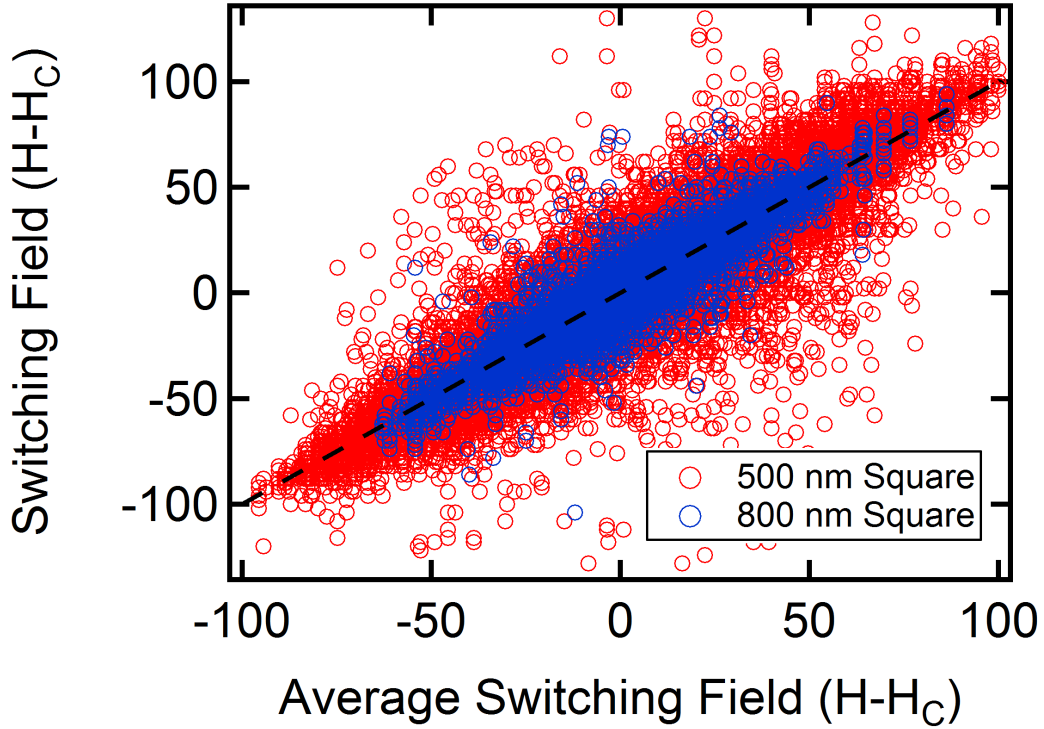


Figure 4.9. The switching field as a function of average switching field

around 10 G. Values of σ_H for these samples as a function of lattice spacing and geometry are shown in Fig. 4.10. The standard deviation increases with increasing interaction strength, maximizing at around 20 G for the arrays with the strongest interaction. These values are much less than the width of the aggregate switching field distribution because they are measuring different quantities. The aggregate switching field distribution measures the variation of h_i throughout a lattice, while these values measure the variation of individual island's switching field around its mean value over a series of distinct runs.

Island switching is significantly influenced by local environment; this is already clear from the switching field distributions in Fig. 4.4. An indication of how this influence contributes to microhistory variation is provided by the switching field *covariance*

$$C_h = \left\langle (h_i^\alpha - \bar{h}_i)(h_j^\alpha - \bar{h}_j) \right\rangle_{\alpha; \text{NN}}. \quad (4.5)$$

This quantity is plotted for all arrays in Fig. 4.11a as a function of interaction strength $B_0(L)$. That C_h is negative conforms to expectations since if one island

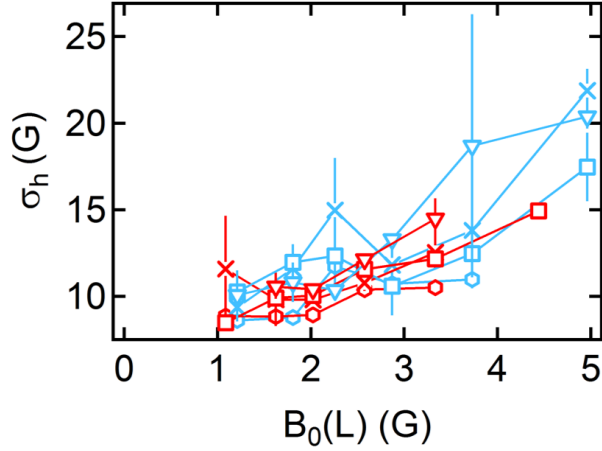


Figure 4.10. Value of σ_h as a function of neighbor field for various lattice types on two samples

switches “early”, it will increase the energy barrier for a neighbor to switch, due to the antiferromagnetic interactions. The arrays with the weakest interaction, although they show significant σ_h (Fig. 4.10), show no significant covariance. As the interactions are increased, the covariance between neighboring island’s switching fields increases in magnitude. The increase in covariance also increases as a function of effective coordination number, similar to how the switching field distribution broadens with effective coordination number. In fact, at these interaction strengths, the impact of array geometry can be described completely by the coordination of the array, rather than whether or not there is frustration. The behavior at low interaction strength gives an indication of the intrinsic behavior of the islands, and the change with increasing interaction strength allows us to judge the impact of interactions. Because dynamics play a large role in the correlations of these systems, and there is some level of random variation that propagates through the lattice by neighbor interactions, it is likely that we will observe significant differences in the microstates.

To further characterize (non)reproducibility of the microhistory, we examine the average overlap

$$\overline{f_{=}} = \frac{1}{2} \left[1 + \left\langle S_i^\alpha S_i^\beta \right\rangle_{i;\alpha \neq \beta} \right] \quad (4.6)$$

at zero magnetization, $\langle S \rangle = 0$. The average overlap is simply the fraction of islands that are in the same state in a randomly chosen pair of distinct runs. Calculated

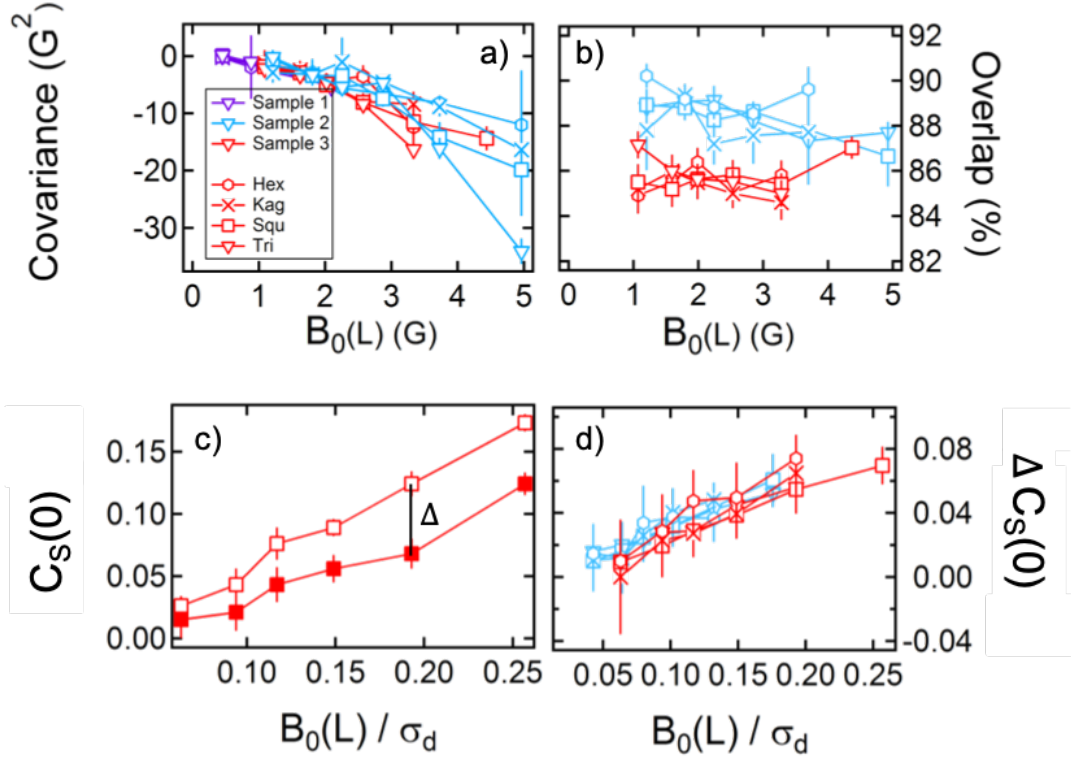


Figure 4.11. a) The covariance of switching fields between multiple runs for all three samples. b) The average overlap at the coercive field between pairs of runs for samples 2 and 3. Overlap is defined as the percent of islands that are in the same state in both states considered. c) The experimentally measured value of $C_S(0)$ (open squares) and the average value of $C_S(0)$ for randomly generated states with the experimentally measured overlap with the experimental state (solid squares), for a 500 nm square array from sample 3. The difference between these two curves is defined to be $\Delta C_S(0)$ d) The average difference in correlation between the experimentally measured state and a state with the experimentally measured average overlap.

values for samples 2 and 3 are plotted in Fig. 4.11b and range from 84% to 90%. Sample 2 has a consistently larger overlap than sample 3, which is reasonable since σ_h is similar for the two samples while σ_d is larger for sample 2. A larger ratio of σ_d/σ_h implies that each island has access to a smaller subset of the switching region, increasing the number of islands in the same state at any given point in the switching process.

One may wonder whether an average overlap approaching 90% is enough by itself to explain the observed macrohistory repeatability. A simple numerical experiment shows this is not the case. Starting from one specific $\langle S \rangle = 0$ microstate, we randomly select a fraction $1 - \bar{f}_-$ of islands, flip them, and calculate the change

$\Delta C_S(0)$ of the nearest-neighbor correlation (see Fig. 4.11c). Average values of $\Delta C_S(0)$ for 1000 repetitions of this experiment are plotted in Fig. 4.11d. The drop in C_S is significantly greater than the standard deviation of the distribution over runs, hence one concludes that there is more to the correlations than simply the overlap. Indeed, one may calculate that if microstate S'_i is obtained from S_i by independently flipping spins with probability $1 - \overline{f_{\pm}}$, that the nearest-neighbor correlation of the new microstate has an expectation value

$$\langle S'_i S'_j \rangle_{\text{NN}} = (1 - 2\overline{f_{\pm}})^2 \langle S_i S_j \rangle_{\text{NN}}. \quad (4.7)$$

The origin(s) of microhistory stochasticity are not clear. Noise arising from the experimental setup, for instance in the power supply or magnet, seems unlikely to be responsible since such influences would be uniform across the sample; the magnetic field is quite homogeneous over our small field of view. However, the significant run-to-run switching field covariance shows that the stochasticity is at least strongly affected by local conditions. *Prima facie*, one expects thermal fluctuations to be completely negligible; the energy scale of room temperature $k_B T$ equals the magnetic energy of an island in a field of order 10^{-1} G, about 5% the field step size, which should lead to high thermal stability at room temperature. However, near the coercive field, thermal fluctuations can be surprisingly significant in understanding the behavior of nanomagnetic systems. [82, 83]

A non-negligible fraction of islands might be caused to switch in a slightly different field by a thermal fluctuation in a given run, and the “misstep” would then be amplified and propagated by island interactions. One might expect these propagated missteps to lead to a decrease in the zero magnetization overlap as the interactions are increased. However, we observe that the overlap is insensitive to interactions. This is possibly because only a subset of islands may be susceptible to thermal fluctuations at any given field step. Any island with a coercivity that is not sufficiently close to a given field is constrained to remain stable in its moment orientation at that field in all runs.

In conclusion, weakly interacting arrays of perpendicular artificial spin ice can be characterized using MOKE microscopy to understand both the development of correlations and the microstructure stochasticity. Further studies are indicated to confirm or disprove the proposal that thermal effects contribute significantly

to the stochastic nature of these systems. While it is interesting to study these effects and understand the ordering in a system dominated by disorder, to maximize the usefulness of perpendicular artificial spin ice it is necessary to increase the interactions in the system. It is evident from this data that changes will need to be made to the system to reach a regime where we can observe effects of frustration on quasi-dynamic data and characterize the ground state. The remainder of this chapter will be focused on a way to enhance the interaction strength in perpendicular artificial spin ice.

4.3 Increasing the Interaction Strength

We demonstrate in the following sections that it is possible to increase the interaction strength in perpendicular artificial spin ice arrays by channeling the magnetic flux between islands through a soft magnetic underlayer of Py. There have been studies on the behavior of exchange coupled in-plane islands on Py [84] and Py on Co/Pt [85, 86]. To serve as a flux channel, the coupling between the islands and the Py must be via dipolar interactions rather than direct exchange. The idea of increasing coupling through an exchange-decoupled layer of Py is an idea that comes from the bit patterned media community [87–89], but because our systems are larger and operate on a much slower timescale we have different materials considerations than exist in the more densely packed and significantly smaller arrays that comprise bit patterned media.

Previous sections demonstrate how critical a precise quantization of disorder is if we would like to make comparisons between multiple samples. Also, we know that dipolar fields fall off rapidly with increasing distance, so it is desirable to have the soft layer in close proximity to the islands we are attempting to couple. With these ideas in mind, we initially attempted to deposit the Py layer on top of the islands rather than underneath, so that we could directly compare correlations before and after film deposition. Depositions on continuous films confirmed we could still detect the Kerr effect through a 10 nm thick Py layer. However, when we deposited such a layer on our patterned sample, the Py did not form a continuous film. Instead, it formed a thin coating over every island and left discontinuous gaps between islands (See Fig 4.12). To quickly compare correlations between samples, we fabricated small rhombuses of 16 islands each and demagnetized them,

comparing the distribution of energy states in these patches to gauge how strongly interacting each sample is. The more small patches that are in the ground state, the more strongly interacting the sample is. We found that for samples with a Py overlayer, the correlations became completely random, indicating that the process of depositing Py on top of the islands removed any order in the sample.

Next, we fabricated pairs of samples: one with a py underlayer and one without. Sample 4 has a corresponding sample 4p with a Py underlayer, and 5 has a corresponding sample 5p. Since the Pt/Co films in each pair were co-deposited and the lift-off was carried out simultaneously, we assume that the disorder in both of the samples is identical; our assumptions in the calculation for finding the disorder are no longer true for the Py coupled samples and we cannot directly calculate the disorder in those samples. Again considering the small rhombuses, the sample with the Py underlayer has more patches in the ground state and thus is likely more strongly coupled (See Fig. 4.13). Therefore, we continued our experiments with samples fabricated using Py underlayers.

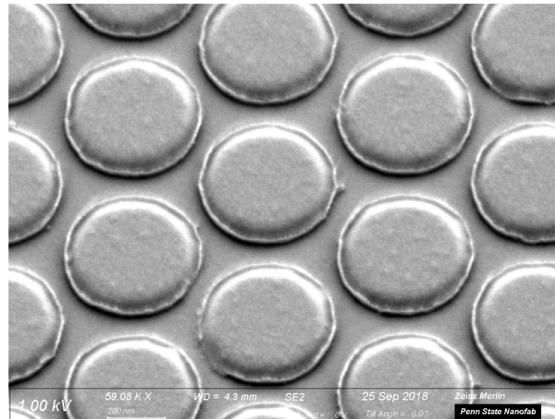


Figure 4.12. SEM of a sample with a Py layer deposited over an array of Pt/Co islands, showing the discontinuity of the Py layer deposited this way.

4.3.1 Magnetization in Py Layers

A simplified schematic of the proposed magnetic flux channeling effect is shown in Fig. 4.14. Two islands in opposite magnetic states are shown side by side. Each of these exerts a dipolar field on the Py layer, causing the spins in the Py to align with the field as shown in the figure. These Py spins, in addition to aligning with

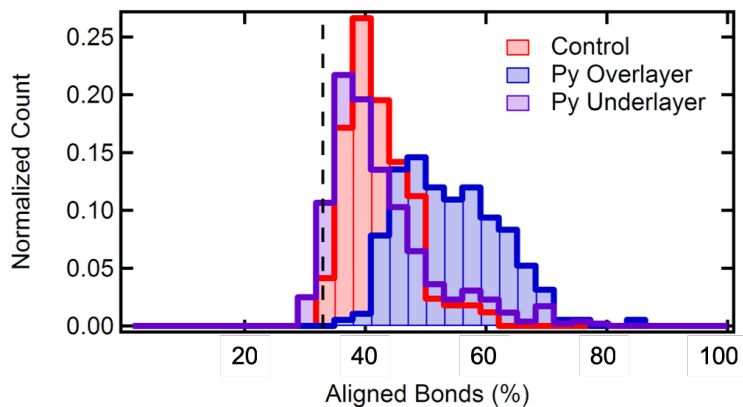


Figure 4.13. Percent of aligned bonds, proportional to the energy, in demagnetized patches of Pt/Co islands for a sample on Si, a sample with a Py overlayer, and a sample with a Py underlayer. The vertical dashed line denotes the ground state energy.

the dipolar field of the islands, also produce their own dipolar field which in this case then serves to supplement the islands' dipolar field and increase the strength of the interactions. There are additional effects in the presence of an external field, as an external perpendicular field causes the spins in the Py to cant to align with the field and supplement the net perpendicular field. This is shown in Fig. 4.14b. Of course, these are simplifications that become far less intuitive in complicated, multi-island patterns. It may be more accurate to think of the Py acting as a third body in the interaction rather than passively following the flux of the islands in more realistic considerations of the system.

One way to visualize what might be happening in the Py layer in realistic scenarios is to use micromagnetic simulations. We use MuMax3 as our simulation package [90]. While it would be prohibitively expensive computationally to simulate an entire array, it is possible to simulate small groups of islands and extrapolate longer range behavior from there. We begin by simulating pairs of Pt/Co islands at the lattice spacings used in our physically fabricated samples. We use an initial magnetization state with the islands either aligned or anti-aligned with one another, and then let the magnetization relax to a physically realistic state. Once relaxed states have been generated, there are multiple ways to carry out further analysis. We first calculate the difference in energy between the aligned and anti-aligned states, to calculate an estimate of pair energy as a function of lattice spacing. In carrying out this calculation, we find pair energies that agree with previously

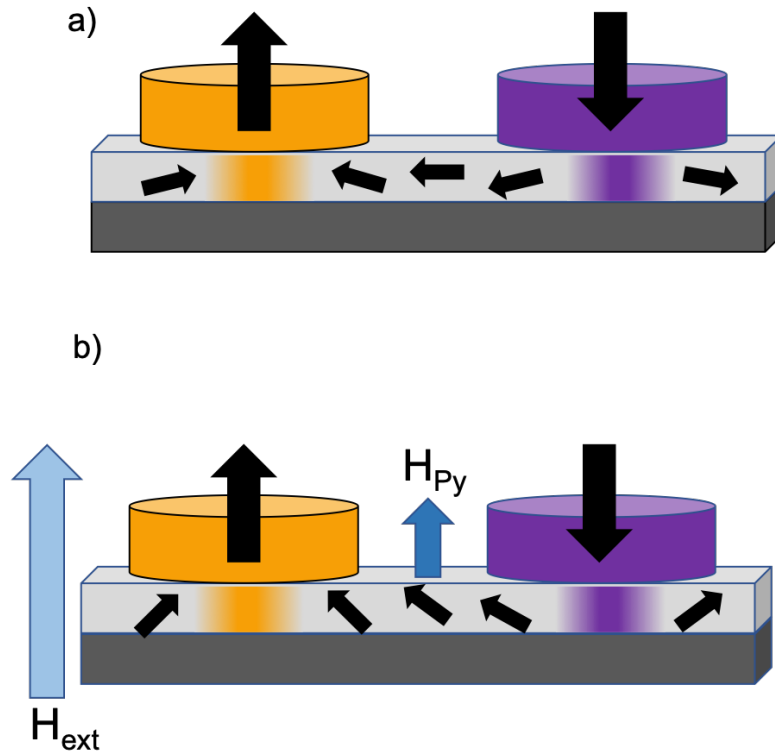


Figure 4.14. Cartoons showing simplified flux channeling between neighboring islands in anti-aligned states, a) without and b) with an external field.

published results [8]. We also extract the effective magnetic field at each of the islands from the simulation. This effective magnetic field contains contributions from both the island itself and from its simulated neighbor. By taking the difference in effective magnetic field at one of the islands between the aligned and anti-aligned states divided by two, we arrive at a reasonable estimation of the field of an island on its neighbor. Comparing this estimate to the dipolar estimate we have been using thus far, we observe a good agreement for most of the lattice spacings, but the dipolar estimate slightly underestimates the interaction field at very close lattice spacings (Fig. 4.16). This suggests our dipolar approximations are generally sufficient, and that our simulations can be used to reasonably extract the field of an island on its neighbor.

Once we add Py layers to the simulations, the system becomes significantly more complicated. For one, there is more magnetic material to be simulated and therefore the relaxation times become longer. We must decide how large a

section of Py to simulate. If we use too small a piece, the boundary effects due to finite size of the Py contribute significantly to the energy of the system and the simulation is not accurate for a pair of islands on an infinite film of Py (what we would ideally like to simulate). If we use too large a film of Py, the computation becomes prohibitively time consuming and it would be unrealistic to run full sets of simulations. In addition to the size of the Py, we must make a decision about the initial condition on the magnetization in the Py. If we start from a random magnetization or a saturated state in the $\pm\hat{z}$ direction, the Py tends to relax to a state with many magnetic vortices, even far away from the islands. This may not be a reasonable representation of the actual magnetization in the Py, and also makes it difficult to compare between states with islands saturated aligned or anti-aligned as the differences in the Py dominate the energy. However, if we initialize the magnetization to be uniform in the plane of the Py, there are multiple nonequivalent directions in which the magnetization might lie.

Another option is to use a small section of Py with periodic boundary conditions, but this is not an avenue we can utilize to simulate a single pair of islands on Py. If we simulate a 4 island square array with Pt/Co islands arranged in the ground state configuration and allow the system to relax from a random initial permalloy state with periodic boundary conditions, the final state of the permalloy develops a preferred direction in the in-plane orientation. This, in combination with the fact that we believe we have an in-plane field component providing a bias in our system, leads us to believe that starting from an in-plane saturated direction will give us the most realistic representation of the magnetic state in our system. We start with the saturation in the $\pm\hat{x}$ and $\pm\hat{y}$ directions. Islands pairs are oriented such that the islands are offset in the \hat{x} direction. Images of relaxed states with islands aligned and anti-aligned and initial Py magnetization in the $-\hat{x}$ and $-\hat{y}$ directions are shown in Fig. 4.15.

We observe qualitatively both similarities and differences between the initial starting conditions. Considering specifically the anti-aligned island pairs, in both cases, the Py nearest the islands develops an opposite \hat{z} component from the island, indicated by lighter colored Py around darker islands and vice versa. In simulations where the saturation initially lies in the $-\hat{x}$ direction, this effect in the Py is quite symmetric. In simulations where the initial saturation lies in the $-\hat{y}$ direction, there is an asymmetry which leads to a yin-yang structure in the magnetization. As with

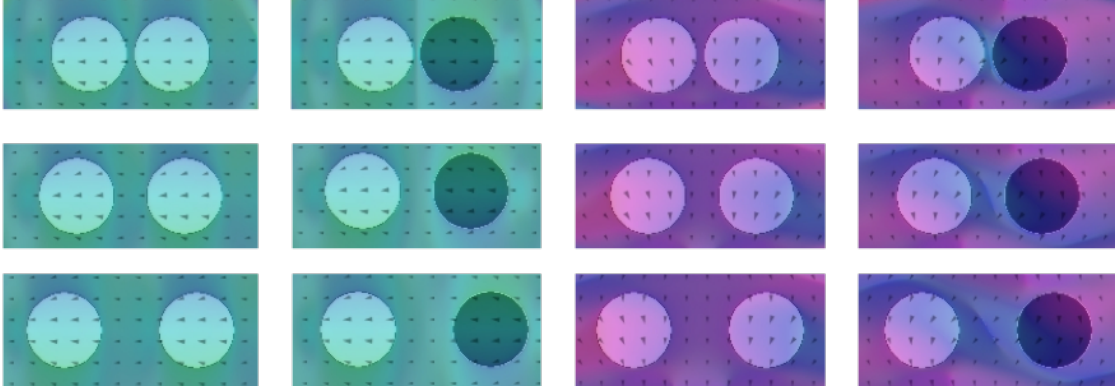


Figure 4.15. Left: Relaxed states from micromagnetics simulations with islands aligned and anti-aligned with initial Py magnetization in the $-\hat{x}$ direction, for 500 nm (top) 650 nm (middle) and 800 nm (bottom) lattice spacing island pairs. Right: Relaxed states with initial Py magnetization in the $-\hat{y}$ direction.

the isolated pairs of islands, we can compare the energy and effective magnetic fields between aligned and anti-aligned pairs. The energy is not so straightforward, as the Py itself provides a contribution to the energy. However, by comparing the effective nearest neighbor fields we can achieve a reasonable estimation of the coupling enhancement provided by the Py layer. This is plotted in Fig. 4.16 for both random initial conditions and saturated in-plane initial conditions. The data with random initial conditions shows the same general trend as the saturated data, but with more fluctuations due to the development of vortices in the Py during relaxation. We can see in general that the coupling strength follows a similar decrease with increasing lattice spacing as the coupling strength without an underlayer, and shows approximately a factor of two increase in magnitude with the addition of a Py layer.

Simulations of more complicated states involving more than a single pair of islands are ongoing.

4.3.2 Demagnetized States

Demagnetization protocols are oscillating, decreasing perpendicular field protocols designed to prepare the artificial spin ice arrays in a state that is as close to the ground state as possible. The ideal, lowest energy state is different dependent on the array geometry. For an unfrustrated array, the ground state is well defined, and arrays that are close to the ground state should have large domains separated by

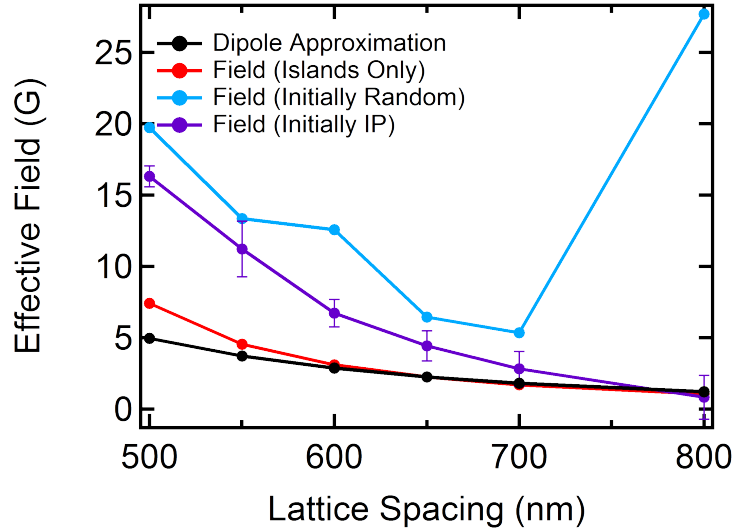


Figure 4.16. The field an island experiences from it's nearest neighbor in the dipolar approximation, and in simulations with and without Py underlayers.

domain walls. For a frustrated array, the ground state manifold is highly degenerate, and it is not clear *a priori* what the ideal ground state should look like. As with the hysteresis data presented above, the order in the arrays can be described using the nearest neighbor spin correlation, C_S , which in the ground state is 1 for an unfrustrated array and .333 for a frustrated array.

The correlations in demagnetized states show the same partial data collapse as the correlations in hysteresis, with a distinct splitting between the correlations of frustrated and unfrustrated arrays for $B_0(L)/\sigma_d > .1$. Correlations in demagnetized states for samples without Py underlayers (samples 2 – 5) are shown in Fig. 4.17.

Unfrustrated Geometries

In the unfrustrated arrays, there is a well-defined ground state with a correlation value of 1. Samples without Py underlayers contain regions of ground state domains, but do not achieve a correlation value greater than 0.39. Samples with Py underlayers show an increase of correlation with an average value of .15 per array; direct comparisons are shown in Fig. 4.18. The chosen x-axis assumes that the disorder in the samples with Py is identical to the corresponding sample without a Py underlayer and uses the field of an island on its neighbor as $B_0(L)$ for samples with and without underlayers, disregarding the impact of the Py on

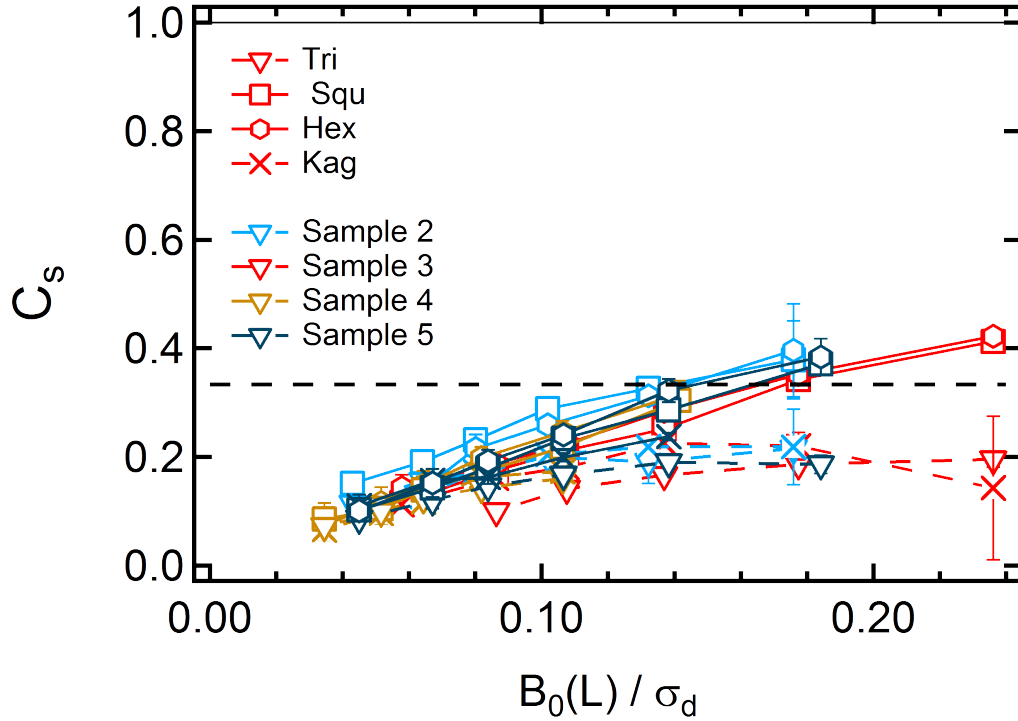


Figure 4.17. Correlation in samples 2 – 5 in demagnetized states showing agreement across all samples when considered as a function of both neighbor field and disorder in the system. Curves with solid lines correspond to unfrustrated geometries, and curves with dashed lines correspond to frustrated geometries. The dashed line at .33 represents the maximum correlation possible for a frustrated array and the solid line at 1 represents the maximum correlation possible for an unfrustrated array.

the interaction strength. The system is designed so that the Py will supplement the interaction strength, but the precise value of the increased interaction strength is unclear. According to papers on soft magnetic underlayers, the underlayer potentially doubles the magnetic write depth [89]. Our micromagnetic simulations also indicate that the field of an island on its neighbor approximately doubles with the addition of a Py layer. So as a first approximation, we considered the correlations assuming that the Py layer doubled the interaction strength. As can be seen in Fig. 4.18b, doubling the value of $B_0(L)$ for samples with Py layers leads to a good agreement of correlations between samples, so this provides a reasonable first approximation of the adjustment in interaction strength from the Py. More detailed calculations are needed to fully understand the nature of this interaction.

The correlation gives a global indication of the microstate of the array, but

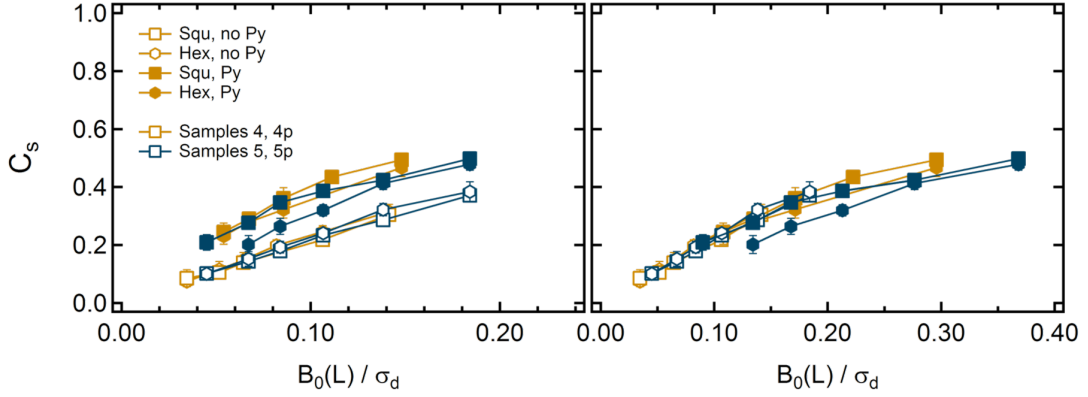


Figure 4.18. a) Correlation in 4, 4p, 5 and 5p showing the enhancement in correlation with a py underlayer b) showing agreement assuming a doubling of interaction strength

as discussed in Section 4.2 there are multiple microstates that could be described by any given global characterization. To further understand how the increased correlation affects the state of the array, we look at images of the demagnetized states. Fig. 4.19 shows images of 500 nm lattice spacing Squ array in a demagnetized state from samples 4 and 4p (without and with a Py underlayer). The domains are visible to the eye as ordered regions in the images, clearly showing an increase with the addition of a Py underlayer. More ways to consider the increase in the range of the interactions will be presented in a subsequent section.

Frustrated Geometries

Frustrated arrays have a highly degenerate ground state manifold with a maximum correlation value of 0.33. Because there are many options for how the system can be placed in a ground state, it is easier for frustrated arrays to achieve correlations that are closer to the ground state than their unfrustrated counterparts, even though the value of nearest neighbor correlation is lower. In Fig. 4.18 we observe that the unfrustrated arrays with a Py underlayer achieve a correlation that is approximately 50% of the ground state correlation. Frustrated arrays with Py underlayers are close to 75% of the ground state correlation (See Fig. 4.20). The correlation in the frustrated arrays has an absolute increase of up to .07 with the addition of an underlayer and follows the same behavior as the unfrustrated samples in that assuming a factor of two increase in interaction strength leads to a rough collapse of the data.

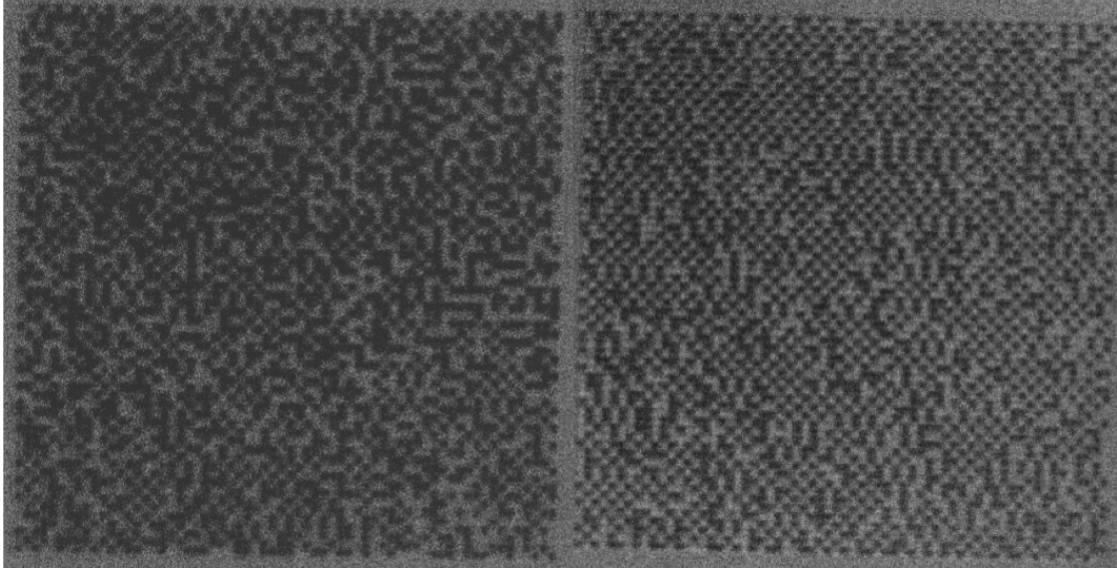


Figure 4.19. Image of demagnetized states for 500 nm lattice spacing square arrays from sample 4 (left) and 4p (right).

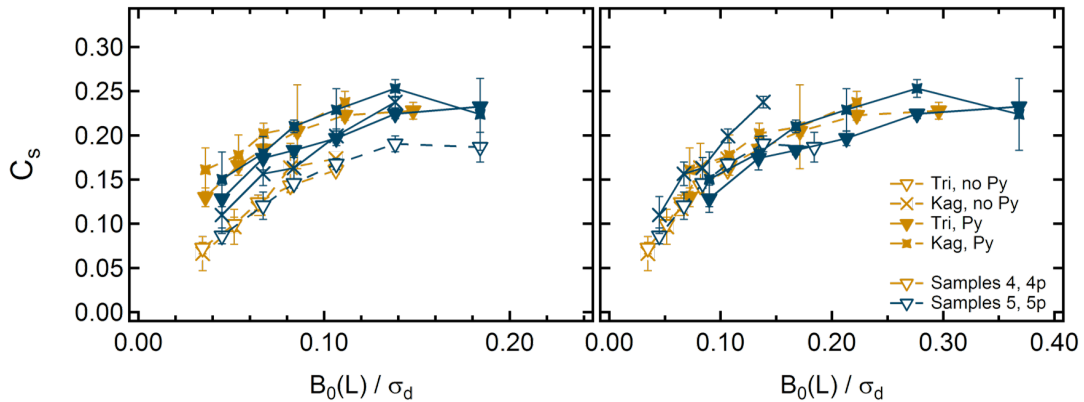


Figure 4.20. a) Correlation in 4, 4p, 5 and 5p showing the enhancement in correlation with a py underlayer b) showing agreement assuming a doubling of interaction strength

Unlike the unfrustrated arrays shown previously, it is difficult to define a “domain” in the frustrated ground state since there are many degenerate ground states. However, it is visually apparent when considering the demagnetized states of frustrated lattices that the Py layer has had a profound impact on the ordering of the array (Fig. 4.21). The control samples show an apparently random arrangement of islands, with small patches of maze-like domains randomly distributed throughout. The Py samples show a strong preferential alignment, developing long maze-like domains in a somewhat uniform orientation. The underlayer in the frustrated

samples apparently is not only increasing the correlation, but it is also providing a preference for what type of ground state the system reaches. We believe this preference is strongly influenced by in-plane fields in the system. This qualitative change in the microstate will be further explored in the next section.

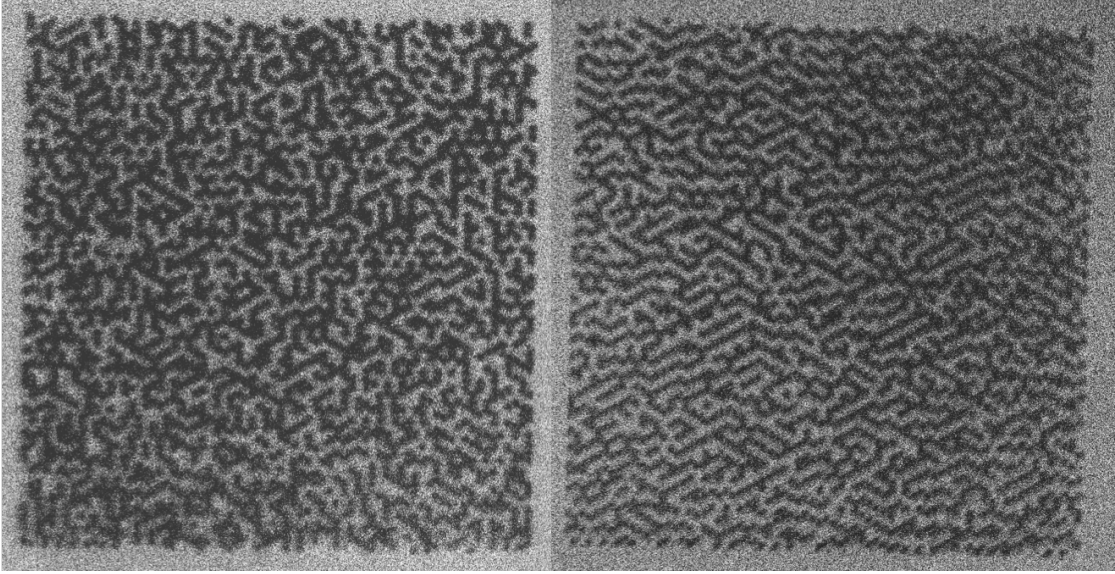


Figure 4.21. Image of demagnetized states in 500 nm lattice spacing Tri arrays from samples 4 (left) and 4p (right).

Qualitative Microstate Ordering

There are two aspects to the qualitative ordering in the microstates that we want to explore further: the increase in the range of the interactions (corresponding to the increase in domain size for unfrustrated arrays) and the symmetry breaking presumably caused by in-plane field components.

To investigate the increase in the range of interactions, we calculate C_S for neighbor pairs beyond first nearest neighbor, which will be denoted as $C_{S,n}$ where n is the neighbor number. Longer range interactions manifest as correlations in farther neighbor pairs, and the extent of the correlations indicates the size of the domains. Even though all pairwise interactions are antiferromagnetic, the correlations will change in sign depending on the neighbor number because the nearest neighbor interactions are stronger than the next nearest neighbor interactions. For unfrustrated geometries, the expected sign of the interaction for

each neighbor number is well defined based on whether that neighbor would be aligned or anti-aligned in the ground state. In square arrays, therefore, $C_{S,1}$ is positive, $C_{S,2}$ is negative, $C_{S,3}$ is negative, $C_{S,4}$ is positive, and so on. Because frustrated arrays have no well-defined ground state, it is not possible to assign an expected sign to every neighbor number. However, it is still reasonable that the correlations would show some variation in sign with differing neighbor number.

Data for square and triangular arrays with and without Py layers are shown in Fig. 4.22. Hexagonal and kagome arrays, while not included here, show similar patterns. In samples without Py underlayers, there are no distinguishable correlations past 3rd nearest neighbor for any lattice spacings, and no correlations past nearest neighbor for lattice spacings greater 600 nm. The initial change in sign of correlation to negative is visible, but by the neighbor number that the system would return to positive correlation, the correlation is already effectively zero. With the addition of the Py underlayer, we see not only an increase in $C_{S,1}$, we also see an increase in the magnitude of $C_{S,>1}$ as expected. All measured lattice spacings show nonzero correlations up to at least $n = 3$. A clear alternation of sign up to at least $n = 6$ is visible in the arrays with the highest interaction strength for both frustrated and unfrustrated arrays. The square array shows the same basic pattern with and without an underlayer, just enhanced by the Py. The triangular array shows a much more dramatic change since the alternation is not visible in the sample without an underlayer.

To explore the symmetry breaking, we use Fourier transforms to visualize the ordering in different directions in the arrays. To find the order in a particular direction, we divide the background subtracted, demagnetized image into 10 pixel wide strips, averaging across each strip to minimize noise. We then take an FFT of the resulting curve and average the FFT's of all slices across an image to generate curves such as those shown in the right panel of Fig. 4.23. This figure contains curves taken in two different directions in the lattice, as denoted by the arrows in the left panel. The relevant frequency for antiferromagnetic patterns corresponds to twice the lattice spacing of the array, denoted by the box in Fig. 4.23. We can see that the triangular array considered has a peak at this frequency when considered perpendicular to the apparent ordering direction, and no features when considered parallel to that direction. To characterize this asymmetry more thoroughly, we rotate the image through 5° increments and carry out the FFT in each direction,

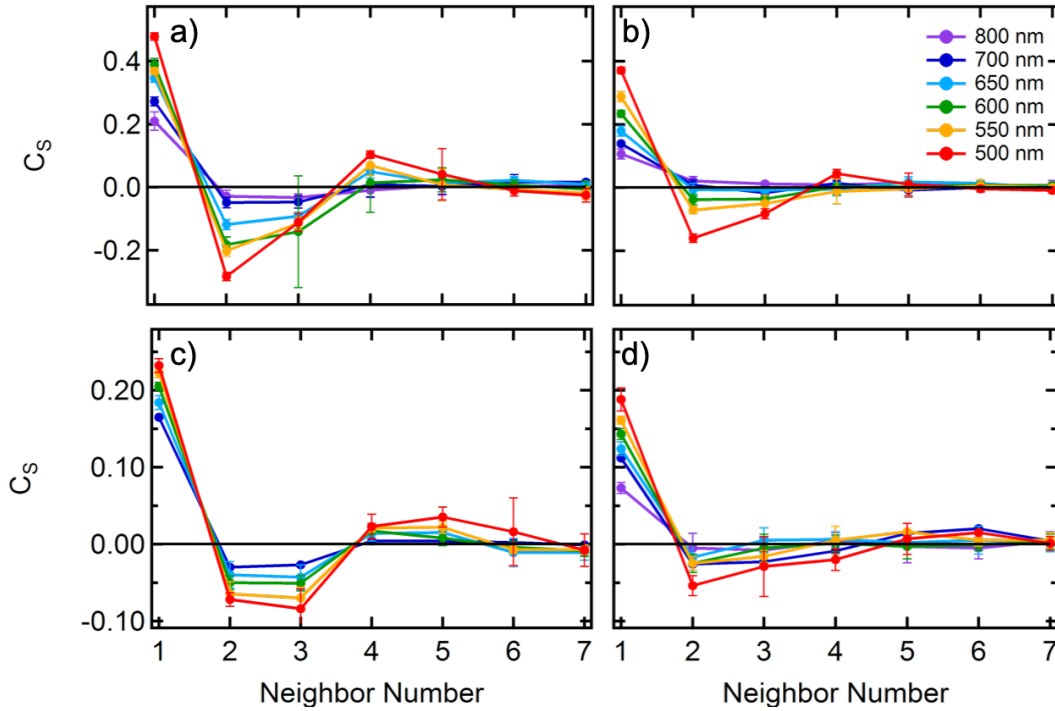


Figure 4.22. $C_{S,n}$ for $n = 1 - 7$ for square arrays from sample a) 5p and b) 5 and for triangular arrays from sample c) 4p and d) 4.

isolating the frequencies corresponding to twice the lattice spacing. For a symmetric state, these rotational curves would have peaks in directions that align with the underlying lattice symmetry, so in 90° increments for the square array and in 60° increments for the triangular and kagome lattices. The hexagonal lattice has no continuous lines of islands and so does not show antiferromagnetic ordering discernible through this type of FFT. Directional FFTs are shown in Fig. 4.24 and 4.25 for unfrustrated and frustrated lattice types, respectively. These curves were taken from 500 nm arrays from samples 4 and 4p, but samples 5 and 5p show the same behavior.

First, considering the directional FFT of the unfrustrated lattices without Py, we observe that the hexagonal array appears quite noisy, as expected. The square lattice has a small peak in antiferromagnetic ordering every 90° , in line with the underlying lattice symmetry. We believe these are due to magnetic order and simply not lattice structure because they are broad peaks. With the addition of the Py underlayer, the peaks become more well defined due to the increased order in the array. They also develop an asymmetry, with the peaks at 90° and

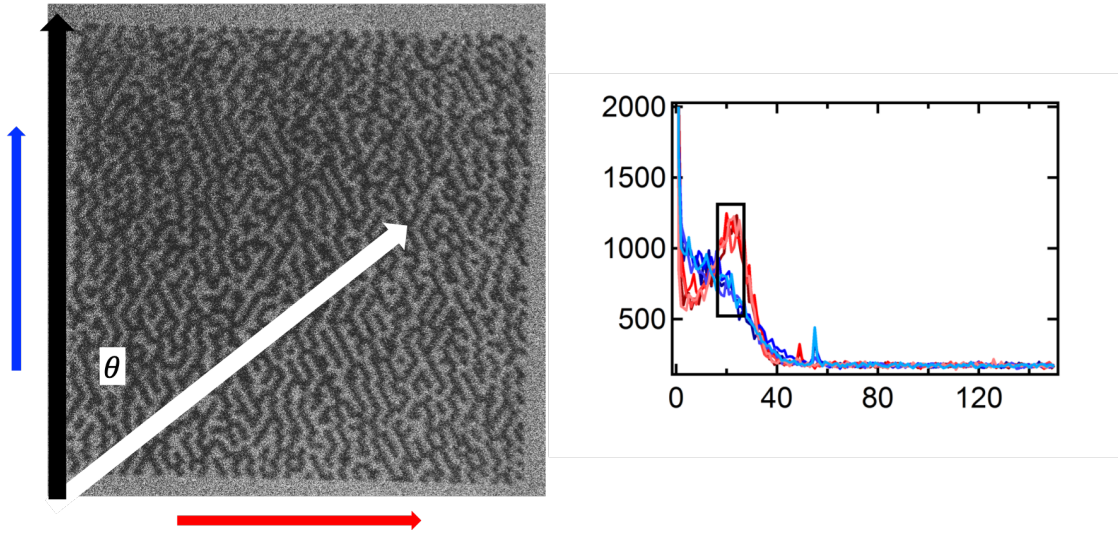


Figure 4.23. Left: A demagnetized state of a 500 nm lattice spacing triangular array, with arrows denoting slice directions used for directionally dependent Fourier transforms. Right: Fourier transforms taken in directions separated by 90° , showing a distinct asymmetry in ordering. The box highlights the frequency corresponding to twice the lattice spacing, where we expect a peak with antiferromagnetic ordering. Each curve corresponds to a different demagnetized state, confirming that this asymmetry is consistently present when the system is reinitialized into a new demagnetized state.

270° appearing stronger than the peaks at 0° and 180° . This indicates that there is likely some physical symmetry breaking in our measurement system; most likely a small in-plane field component that slightly biases the Py layer and gives a preferential direction to any deviations from the ground state to appear in the lattice.

From the directional FFT of the frustrated lattices, we find no apparent ordering in the samples without a Py underlayer. The peaks in the kagome lattice are likely due to the underlying lattice structure rather than any magnetic ordering present due to the peak sharpness. This is unsurprising as the magnetization appears quite randomly distributed in the frustrated arrays. In samples with Py underlayers, the kagome lattice develops the expected 60° symmetry, with a marked asymmetry in the peak strength. The triangular array does not develop a 60° symmetry, instead showing two strong peaks at 180° separation, consistent with a well oriented, stripe domain structure. Again, this asymmetry is likely due to the presence of an in-plane field component, but it has a much stronger effect on the frustrated arrays and the triangular lattice in particular. We suspect that the effect is stronger in the

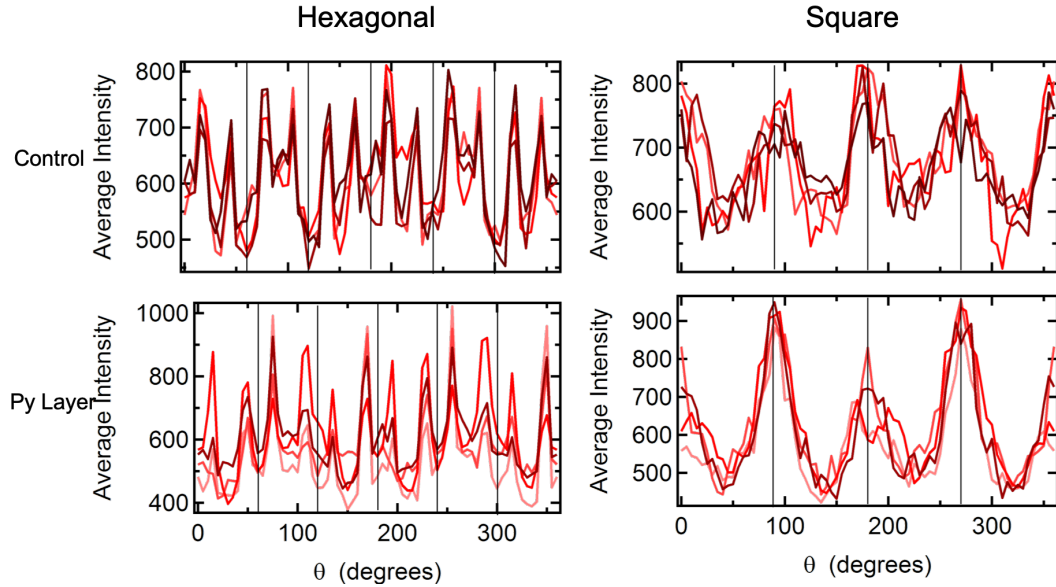


Figure 4.24. Directional Fourier Transforms in unfrustrated arrays (left: hex, right: squ) at 500 nm lattice spacing, for samples without (top) and with (bottom) Py underlayers. Each curve corresponds to a different demagnetized image.

triangular lattice because it is more highly coordinated, and there is less space in the lattice for the Py magnetization to relax.

These initial measurements suggest it might be possible to control the final magnetization state in perpendicular arrays of artificial spin ice on Py underlayers by intentionally applying in-plane fields in different directions during the demagnetization process.

4.3.3 Quasi-Dynamic Data

In addition to considering the impact of the Py layer on the demagnetized states of artificial spin ice arrays, we also consider the impact of the Py layer on the quasi-dynamic behavior as discussed in section 4.2. In the presence of an external field, the Py layer contributes a supplemental field to the external field (See Fig. 4.14). This supplemental field will lower the applied field required to switch the Pt/Co islands. We compare the coercivity of the samples patterned with and without Py underlayers to judge the influence of the Py layer. Fig. 4.26a shows the coercivity of arrays from samples 4 and 4p, with a coercivity of about 800 G for the control sample and an average decrease in coercivity of around 125 G. Samples

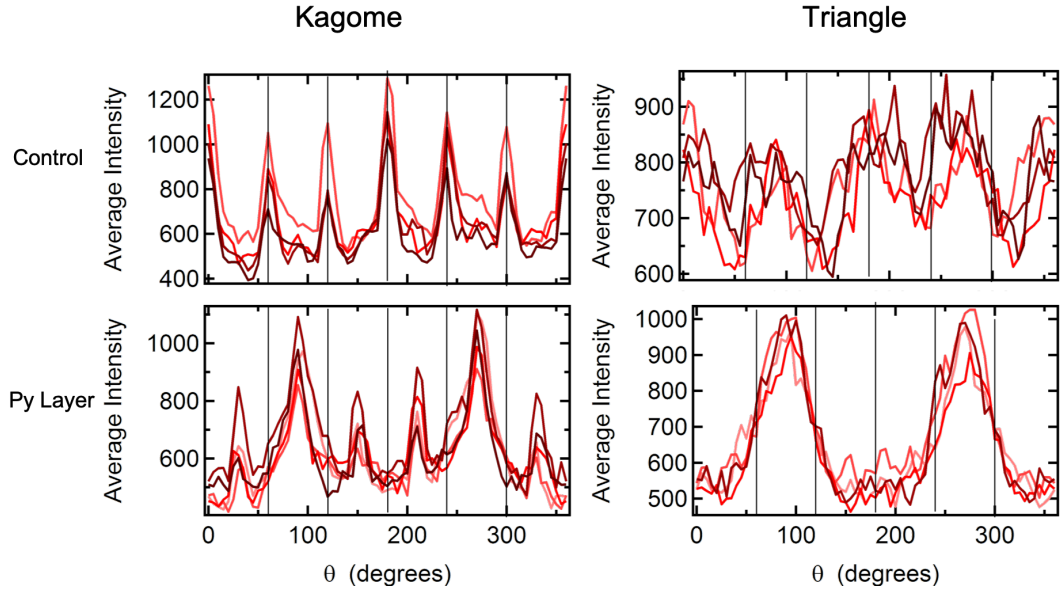


Figure 4.25. Directional Fourier Transforms in frustrated arrays (left: kag, right: tri) at 500 nm lattice spacing, for samples without (top) and with (bottom) Py underlayers. Each curve corresponds to a different demagnetized image.

5 and 5p are not pictured but show an average control coercivity of 700 G for the control sample and decrease of around 100 G. This is in line with our expectations; the influence of the Py layer should be slightly lower at lower fields because the canting is determined by the applied field. However, the original coercivities are similar enough that the offset should be similar.

Another indication of increased interaction strength, as introduced in section 4.2, is a broadening of the switching field distribution width. The measured values of σ for samples 4 and 4p are shown in Fig. 4.26b. Again, in line with our expectations, there is an increase in σ with the addition of a Py underlayer.

Finally, we consider the maximum correlation in the array throughout the quasi-dynamic switching process, as shown in Fig. 4.6. Data from unfrustrated samples with and without Py are shown in Fig. 4.27a and frustrated arrays are shown in Fig. 4.27b. We have previously observed no significant impact of frustration on the maximum correlation achieved during a hysteresis loop, and have also observed that the magnitude of the increase due to Py is different for frustrated and unfrustrated arrays in demagnetized states but in both cases is approximately equal to a doubling of the interaction strength. So it might be reasonable to expect the same increase in correlation for all arrays during hysteresis.

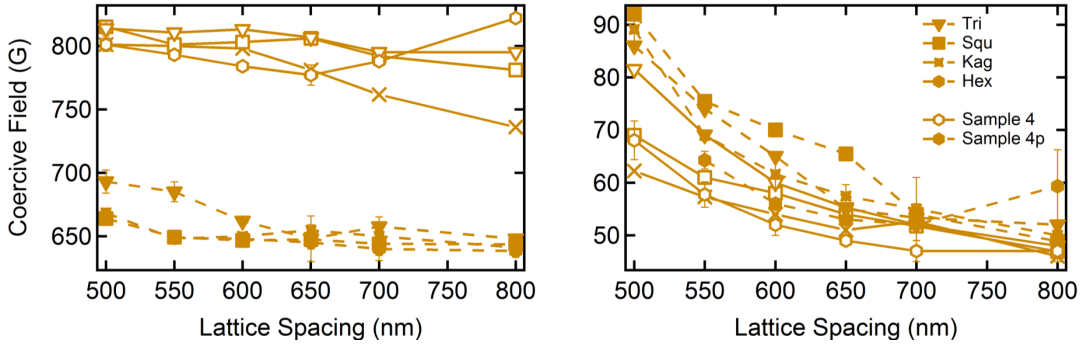


Figure 4.26. Left: Coercive field of arrays from samples 4 and 4p. Right: Width of switching field distributions for arrays from samples 4 and 4p.

Instead, what we observe is that the unfrustrated arrays show a stronger increase in correlation than the frustrated arrays, with the unfrustrated arrays still showing an approximate doubling of interaction strength. In a demagnetization protocol, the magnetization of the Py layer is repeatedly cycled between the $\pm\hat{z}$ directions, giving the magnetization more opportunity to reorient into an ideal state. Without this cycling, the Py is unable to help the frustrated arrays achieve the same level of increased correlation as the unfrustrated arrays because the Py is not able to reorient its magnetization effectively enough to approach the ground state and instead is limited to an intermediate state. Additional simulations and theory are in progress to understand this mechanism more clearly.

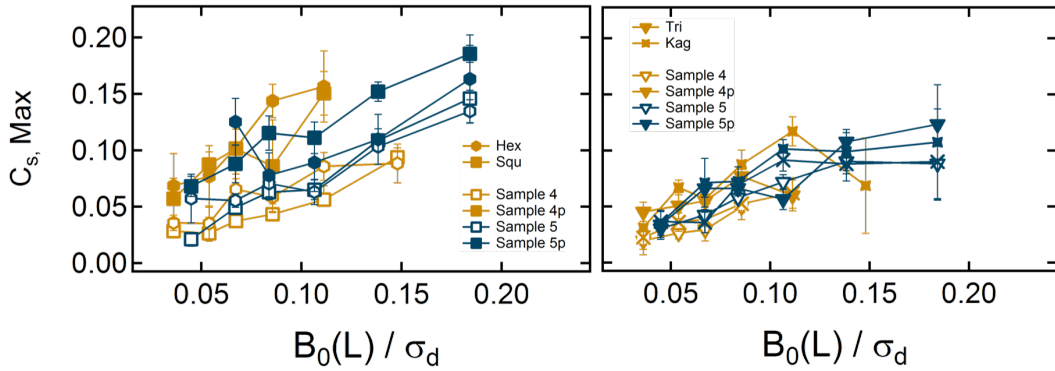


Figure 4.27. Left: Maximum correlation during a hysteresis loop for unfrustrated arrays from samples 4, 4p, 5, and 5p. Right: Maximum correlation during a hysteresis loop for frustrated arrays from these samples.

In conclusion, we have used Py underlayers to increase the coupling strength in

perpendicular artificial spin ice arrays by channeling the magnetic flux through the Py. This layer both quantitatively changes the correlation in the demagnetized state and qualitatively affects the structure of the state. The qualitative effect is much more apparent in frustrated lattices because they have more available microstates in the ground state. During hysteresis loops, the correlations are also enhanced by the Py layer, and more strongly for unfrustrated lattices than frustrated ones. This initial work suggests more comprehensive micromagnetic studies would be beneficial in elucidating the nature of the Py coupling, in particular throughout a quasi-dynamic process. It also suggests that using Py coupling is a reasonable avenue toward fabricating perpendicular artificial spin ice arrays that can be placed in the ground state. The samples presented in this dissertation have relatively high levels of static disorder, so tuning the fabrication process could significantly increase the correlations achieved without making additional changes to the system. Finally, this data suggests that for samples with Py underlayers, we may be able to control the preferred microstate of the array using intentionally applied in-plane fields, opening another avenue to study frustration and the frustrated ground state. These results are preliminary; this project has many interesting questions to be pursued from here.

Chapter 5 |

Magnetic Metalattices

Note: Sections of this chapter were taken from reference [38]. This work was supported by the Penn State Center for Nanoscale Science, an NSF-sponsored Materials Science and Engineering Center under award DMR-1420620.

5.1 Introduction

This chapter shifts focus from two dimensional patterned thin films to three-dimensional structures called metalattices. These are fully interconnected, confined systems, and much like the patterned films discussed previously are expected to have interesting emergent properties due to geometrical considerations. Magnetic properties of metalattices are studied using SQUID magnetometry. As described in Chapter 2, this technique gives us access to magnetic information over a wide range of temperatures and fields. Because this is a bulk measurement technique and not an imaging technique, we do not have microstate information for these systems. Instead, we must make inferences about the local magnetic behavior based on global characteristics. First, we will discuss metalattice infiltrated with a ferromagnetic material, and then we will discuss induced magnetism in non-ferromagnetic metals.

5.2 Nickel Metalattices

Ni metalattice samples were fabricated using high pressure confined chemical fluid deposition by collaborators in the Badding research group at Penn State. An overview of the deposition process is given in Chapter 2 and explained in detail in ref. [38]. Ni metalattices were fabricated using 100 nm and 30 nm periodicity

templates and a continuous Ni film to use as a control was fabricated using the same system. A TEM image of two different infiltrated Ni lattices is shown in Fig. 5.1, with yellow EDS highlighting where there is Ni present in the image.

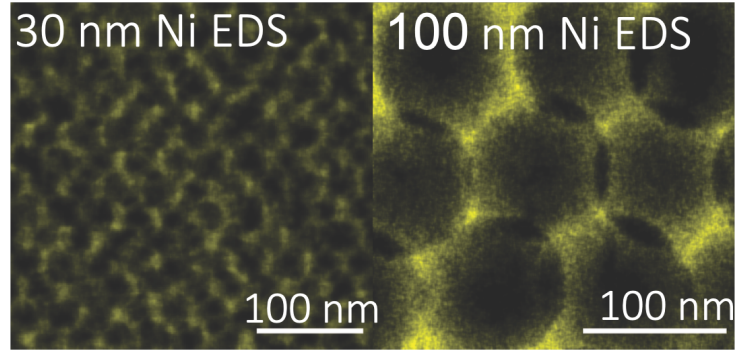


Figure 5.1. TEM image of 30 nm (left) and 100 nm (right) infiltrated Ni metalattices, with yellow EDS highlighting the areas where Ni is present.

We investigated the magnetic properties of metalattices by SQUID magnetometry, after removing the top Ni layer using hydrochloric acid (HCl) spin-etching. The silica sphere templates that define the nickel metalattices could in principle have fcc (abc stacking), hexagonal close-packed (hcp) (ab stacking) or other stacking patterns. However, we found that 30 nm nonmetallic metalattices were fcc by an analysis of TEM images at different angles (unpublished). Although we did not check the structure of the nickel metalattices, they are likely also fcc as the templates were synthesized under identical conditions. For any of the close-packed structures, the electron microscopy images reveal that the sphere layers are largely parallel to the substrate, as would be expected. For fcc metalattices, the [111] metalattice crystal direction will be normal to the substrate plane. While synthesis of single crystal silica sphere templates may be possible, thus far it is reasonable to expect some variation in the orientation of different domains in films millimeters across such that the domain orientation rotates around [111]. A lower bound of tens of microns on the size of these domains is evident from SEM images of their top surfaces (at longer length scales associated with lower magnifications it becomes difficult to resolve individual spheres). Modeling suggests that the easy axis of magnetization of fcc permalloy metalattices (neglecting crystalline anisotropy and magnetostriction) lies in the [001] direction, which is 54.7° from [111] and thus not in the plane [40]. Topological transitions are predicted to occur along the easy axis

as well as in other directions.

There have been multiple reported studies of magnetically infiltrated inverse opal structures in literature. However, the magnetic properties of nickel inverse opal metalattices, which have periodicities of 100 nm or less and associated meta-atoms with diameters less than 50 nm, should differ from those of larger nickel inverse opals as the magnetic confinement increases. Previous studies have shown that the coercive field required to reverse the magnetization of a nickel inverse opal depends strongly on both its periodicity [41] and the film thickness [91]. Nickel inverse opals with periodicities longer than 100 nm have octahedral sites about the same size as or larger than the exchange length and can support complex magnetic structures such as curling domain modes for which the magnetization tends to form closed loops [40]. They also support more spatial variation in neck magnetization, so the octahedral and tetrahedral sites are predominantly coupled by longer range dipolar interactions between adjacent sites [40]. These interactions can couple isolated nanoparticles as well as interconnected tetrahedral and octahedral sites in inverse opals, forming a system that seeks to minimize its magnetostatic energy. As the inverse opal periodicity decreases to that of metalattices, around 100 nm, the magnetic structures become too small to support curling domain modes. The coercive field in this regime should decrease with decreasing sphere size, the nanostructures should behave as single domain elements, and the dominant coupling mechanism should become exchange mediated through the metabonds [40, 41, 92]. Metabond mediated exchange is a defining characteristic of a magnetic metalattice that allows for the diversity of topologically distinct magnetic structures.

5.2.1 Hysteresis

As one of the interesting properties of magnetic metalattice systems is the potential for abrupt topological transitions [40], we measured field sweeps at low temperature to minimize thermal effects. Field sweeps were taken at 3 K after cooling the sample in a field. The field was swept from 5 T to -5 T and back, using a fine step size of 20 Oe in the switching region and a coarser step size elsewhere. Both samples and empty templates were measured. Data is shown from measurements with the field aligned in the plane of the metalattice. As can be seen from Fig. 5.2, the substrate and template contribution is diamagnetic, and only adds a linear

slope to the data from the metalattice. Any features in the background are at least an order of magnitude smaller than the sample signal. This confirms the dominant magnetic signal from is from the infiltrated Ni rather than the template or substrate. Of course, there is additional noise in the substrate measurement. To avoid introducing this additional noise into the measurement, we use a linear fit to the slope at high field of the sample as the background to be subtracted. The continuous Ni film has a magnetic signal several orders of magnitude higher than the metalattice samples, and the diamagnetic slope contribution is minor even in the raw data.

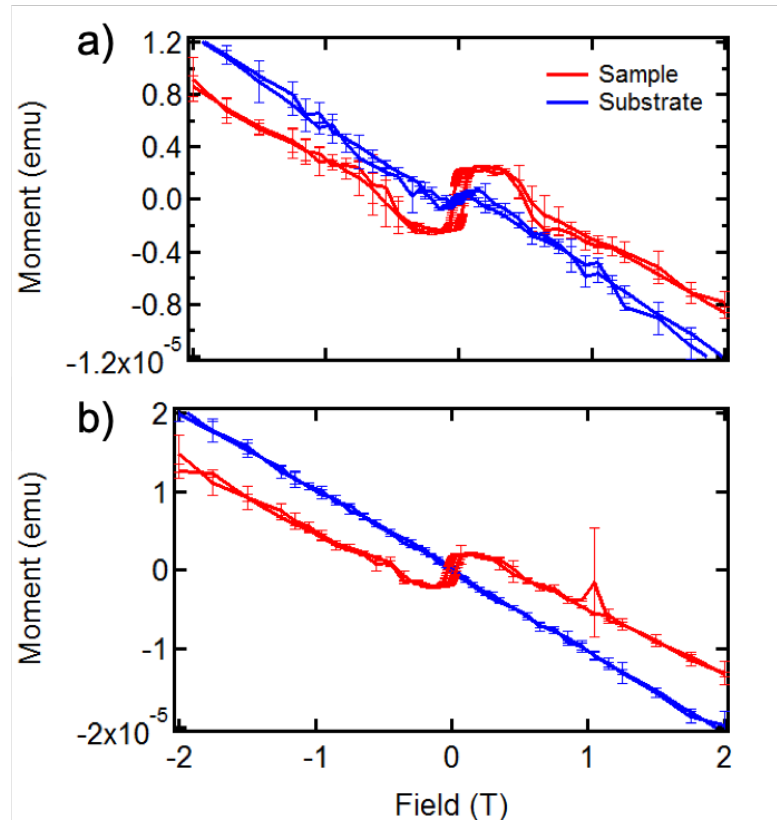


Figure 5.2. SQUID measurements of magnetization v. magnetic field from a) 30 nm and b) 100 nm samples in red and associated templates in blue, showing that the templates do not contribute significantly to the overall observed signal.

We first consider the characteristics of the hysteresis in our samples (Table 5.1). As stated in Chapter 1, 30 nm and 100 nm metalattices consist of 6.8 and 22.5 nm tetrahedral and 12.4 and 41.4 nm octahedral meta-atoms, respectively. The meta-atoms are interconnected by metabonds as small as 2.3 nm in 30 nm

	Thickness (nm)	H_C (T)	M_R (A/m)	M_S (A/m)	Squareness	$M_S/M_{S, film}$
Film	230	0.018	0.0112	0.038	0.29	1
100 nm	600	0.029	0.000070	0.00035	0.20	0.00921
30 nm	1500	0.035	0.000037	0.00011	0.034	0.00289

Table 5.1. Magnetic properties of a continuous Ni film, a 100 nm periodicity Ni metalattice, and a 30 nm periodicity Ni metalattice

metalattices and 7.8 nm in 100 nm ones. Previous studies on inverse opal Ni structures show that the 100 nm and 30 nm metalattice sizes lie in the single domain regime [41]. This was deduced from the dependence of the coercive field (H_C) on the periodicity of the inverse opal: As predicted by theory [40], H_C reaches a maximum value when the length scale of the system becomes too small to support curling domain modes [93]. Below this transition, H_C decreases as the length scales decrease, in qualitative agreement with the behavior of single domain Ni nanoparticles [44]. Film thickness also strongly influences H_C for magnetic inverse opal structures [41, 91]. As our films are different thicknesses, we cannot directly observe a trend in coercivity. However, the coercivity for both metalattice samples shows a significant enhancement over the coercivity of the continuous Ni film (Fig 5.1) because domain walls cannot easily move through their structure. The saturation field (H_S) at which the saturation magnetization is reached for the metalattice is also much larger than that of the bulk film.

Considering the shape of the hysteresis curves, we observe an increase in squareness (defined as the ratio of the remnant magnetization (M_R) to the saturation magnetization (M_S)) as the size is decreased from 100 to 30 nm, in agreement with observations of larger inverse opals [41, 93]. For the 30 nm metalattices, the thin necks give a strong constraint on the magnetization direction, and we expect a one-step transition with no intermediate states. As the metabonds increase in size, their magnetic moments soften and allow for more spatial variation in magnetization [40]. These more complex domain patterns allow for intermediate states thus resulting in a decrease in squareness. Theoretical models predict an intermediate state in the 100 nm metalattices, in which adjacent layers of the metalattices are antiferromagnetically coupled, which we do not observe. The neglect of the magnetocrystalline anisotropy of Ni in these models could change the lattice constant required for the onset of intermediate states. Also, the Ni

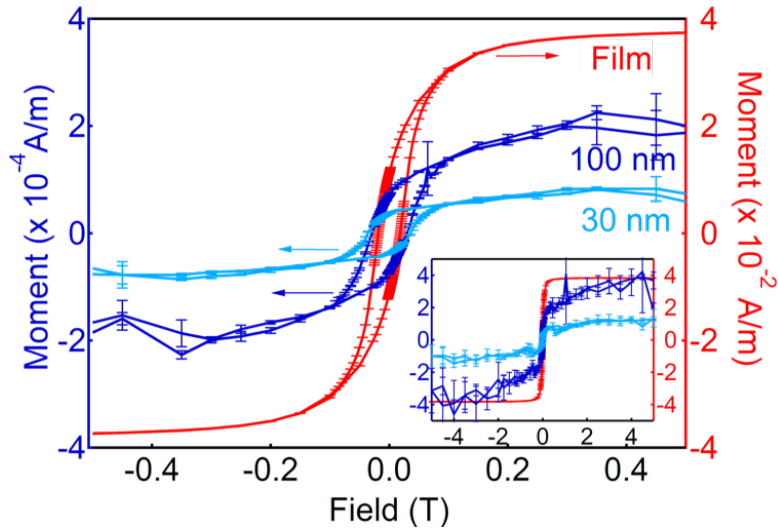


Figure 5.3. SQUID measurements of magnetization vs. magnetic field on Ni film (red, right axis) and metalattices (blue, left axis)

metalattice consists of multiple crystal domains formed from template sphere packings. The different orientations of these domains might smooth out sharp features in the hysteresis. Further increase in the size of the metalattices would allow for the onset of significant curling in the octahedral sites, which leads to additional topological transitions and the development of discrete jumps in the magnetization during the reversal process [40]. The sphere sizes considered are too small to expect this behavior. The metalattice Ni is polycrystalline, but studies on single crystal nanowires suggest that single crystal Ni could show further enhanced coercivity and squareness [94]. High-resolution TEM (HRTEM) reveals that the polycrystalline Ni grains have sizes on the order of 5 to 10 nm, smaller than the magnetic exchange length. Grains this small are in the random anisotropy regime, in which the magnetic anisotropy should be reduced as the exchange coupling averages it out over several grains [48]. As the modeling predictions of a series of topological phases did not account for anisotropy [40], reduction of anisotropy might make the actual magnetic behavior follow the simulations more closely.

Finally, nanoscale samples often show a decrease in saturation magnetization with increasing surface-area-to-volume ratio, attributed to magnetic dead layers at surfaces, oxidation layers, or changes in cohesive energy [44, 94]. We also observe a strong decrease in the magnetic signal at 5 T from the metalattices relative to

the bulk film. The decrease is stronger than usually observed for nanoparticles. Metalattices have a very high surface-area-to-volume ratio, so it is reasonable for surface effects to be very important. Alternatively, the system might be incompletely saturated at 5 T and instead be in a stable intermediate state due to strong domain pinning, where domain walls become “stuck” in local energy minima because of the complicated metalattice geometry. We also cannot rule out the presence of higher field dynamics. This question could potentially be more thoroughly addressed using small angle neutron scattering or higher field studies.

5.2.2 Temperature Dependence

Because the Ni metalattices are in the single domain size regime, we expect that magnetic domain walls will be confined to the necks and that the meta-atoms will behave as single domain particles. Disconnected single domain Ni nanoparticles and superlattices coupled by dipolar interactions show magnetic ordering at low temperatures [44, 95]. However, as the thermal energy is increased, thermal fluctuations rather than applied fields dominate the magnetization direction of the particles. Above this transition temperature (T_B), the particles are said to be “unblocked” and display superparamagnetic behavior [96]. To understand the impact of increasing thermal energy, we measure the magnetic response as a function of increasing temperature. Samples were cooled from 305 K to 3 K in either a 5 T field (FC) or in a 1.3 Oe field (ZFC). 1.3 Oe is chosen to balance the approximate remanence in the magnet after demagnetization. The magnetization was measured in a 50 Oe field as the temperature was increased from 3 K to 305 K. Small step sizes were used at low temperatures, and larger step sizes were used at higher temperatures. Sweeps were measured on both the magnetic samples and the silica templates and Si substrates. For the bulk Ni film, we observe constant behavior, at a high value for the FC data and remaining near zero for the ZFC data. This is in agreement with what we expect for a ferromagnet below T_C . For the metalattice samples, we see a slight relaxation in the magnetization with an increase in temperature for the FC sweep. Again, the ZFC data remains approximately zero. Data is shown on the 30 nm metalattice (Fig. 5.4), but the 100 nm metalattice behaves similarly.

T_B is observed as the temperature at which field-cooled (FC) and zero-field-

cooled (ZFC) temperature sweeps converge, accompanied by a peak in the ZFC scan, and is below room temperature for nanoparticles in our size ranges [44,95]. Granular Ni nanotubes and larger cobalt (Co) inverse opals consisting of agglomerated particles also display superparamagnetism [43,97]. However, for Ni metalattices, we observe no such blocking transition (Figure 5.4). The absence of this transition is evidence for the neck-mediated exchange coupling expected in this system and that the metalattices are behaving as a truly interconnected system. Nickel exhibits itinerant magnetism, so the presence of grain boundaries within the metalattices should not have a major impact on the exchange as long as there are no gaps or significant oxide in them (polycrystalline Ni behaves as a ferromagnet, for example).

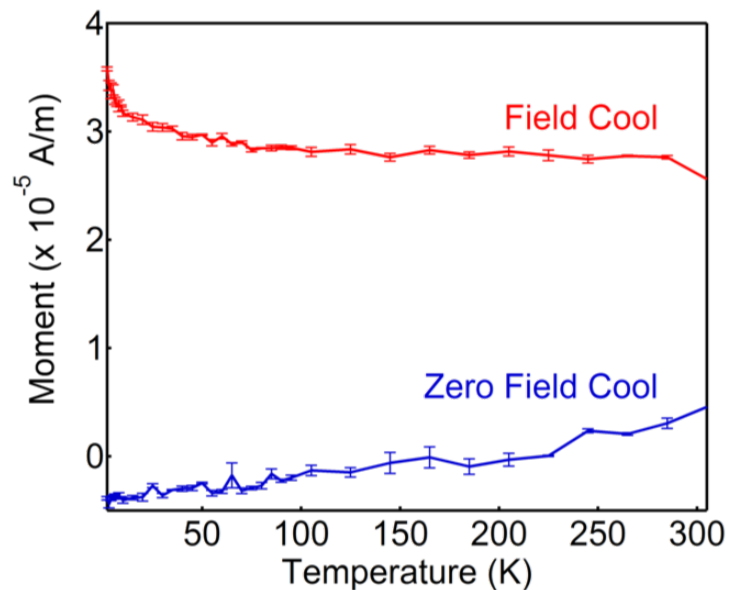


Figure 5.4. Temperature dependent magnetization after field cooling and zero field cooling a 30 nm Ni metalattice sample.

5.2.3 Exchange Bias

After the Ni metalattices are annealed in flowing nitrogen with the silica spheres remaining inside them, electron diffraction and EDS mapping reveal the formation of an antiferromagnetic NiO surface. Hysteresis loops measured after the formation of this oxide layer are shifted to the left from zero, indicative of an exchange bias effect (Figure 5.5) [98]. When hysteresis measurements are repeated after field

cooling in a negative field rather than a positive one, the loop shift is reversed to the right from zero. This confirms the source of the loop shift is exchange bias. The decrease in M_S after annealing is because some of the previously ferromagnetic Ni has been converted to antiferromagnetic NiO. This exchange bias effect between ferromagnetic nickel and antiferromagnetic nickel oxide has also been observed in Ni core/NiO shell nanoparticles [99], as well as in Co inverse opals with grains that are coated with cobalt oxide [97]. The absence of an exchange bias effect in the as-grown metalattice samples suggests minimal surface oxidation occurs during deposition. It is also possible to etch out the silica spheres, which allows for a nanoporous metalattice that could be chemically functionalized or otherwise modified to control magnetic, thermal, or electronic properties or make new metalattices. Thus, it seems likely that the 3D ordered nanostructured metalattices can be modified while largely keeping their structure and order intact. In contrast, nanoparticles chemically modified in solution phase generally are assembled after functionalization. This, in combination with the variety of available templates of different symmetries, could allow for an extremely diverse set of possible 3D ordered nanostructured magnets.

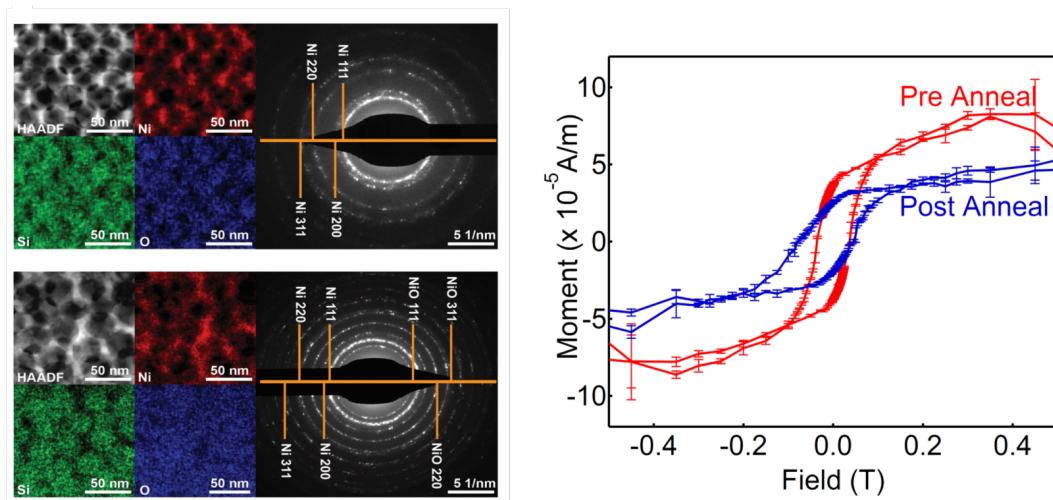


Figure 5.5. Left: TEM with EDS before (top) and after (bottom) annealing, showing that oxygen has migrated to be evenly dispersed and Ni oxide peaks appear in the diffraction after annealing. Right: 3 K hysteresis loops after cooling in a positive field before and after annealing.

In conclusion, magnetic measurements on metalattice systems are in agreement with TEM that these are fully interconnected systems, and characteristics of the

hysteresis data suggest we observe effects of the geometry on the magnetization. Initial measurements indicate that we are able to modify the surface and induce a significant exchange bias effect, which further studies are necessary to characterize completely. This suggests that other, intentional surface modifications may have a strong impact on the behavior of metalattice systems. Other further studies using imaging techniques such as Lorentz TEM to investigate the magnetic microstates in magnetic metalattices could help shed light on the magnetic response of these samples. In the remaining sections, we consider metallic metalattices for which the magnetism is not only affected by geometry but rather is itself an effect of the geometry.

5.3 Platinum Metalattices

While Ni is naturally ferromagnetic at room temperature, there are other metals such as Pt which are “not-quite-ferromagnetic” and are interesting materials to study magnetism. Pt is a heavy metal with strong spin-orbit coupling and is often used in heavy metal-ferromagnet heterostructures for spin transport [4]. As introduced in Chapter 1, Pt nanostructures have been shown to exhibit ferromagnetic behavior [52, 54, 100]. We believe our 3D, interconnected structures are another useful system to look for both magnetic effects and unusual transport by inducing ferromagnetism in Pt. I will focus here on the magnetic properties of the Pt metalattices. Other efforts at Penn State have focused on the associated transport properties. []

Pt metalattice samples were fabricated using the same techniques used to create Ni metalattices, using 14 nm, 30 nm, 60 nm, and 100 nm periodicity. Unlike the Ni samples, in which the top layer was removed by chemical etching, for Pt metalattices, the top layer was physically removed using ion milling. One 30 nm periodicity sample was measured before cap removal, to serve as a control sample. As the signal is completely dominated by the cap, this gives an indication of the behavior of a continuous Pt film. As mentioned in the previous section, it is necessary to check that the templates are not contributing to the measured magnetic signal. In this series of templates, some of the templates are subject to contamination, so while two samples of each size were measured, only one piece is believed to show an accurate representation of the Pt metalattice signal. As described in Chapter 1, metalattice samples larger than 30 nm are likely in close-packed arrangements but there is

some experimental evidence (unpublished) that the 14 nm samples deviate from this close-packed structure into a bcc structure. This change of lattice structure has a significant impact on the topology of the infiltrated magnetic material and is expected to cause 14 nm samples to deviate from patterns found in the other sizes. Hysteresis and temperature sweeps carried out on these samples using SQUID magnetometry are identical to those described for Ni samples.

Hysteresis measurements were carried out at 3 K in the in-plane orientation for all samples considered, and diamagnetic backgrounds were approximated as fits to the high field slope of the measurement and subtracted. Data are normalized to M_S , as there were regions of the substrate that were not fully infiltrated, making an accurate estimation of the volume somewhat difficult. In the capped 30 nm sample that serves as our control, there is paramagnetic behavior, with artifacts around ± 100 Oe due to the underlying metalattice. We observe hysteresis in low temperature measurements for metalattices of 60 nm periodicities and below, but the signal from a 100 nm Pt metalattice is paramagnetic. Since continuous films of Pt are paramagnetic, it is expected that there is a maximum periodicity corresponding to the onset of ferromagnetic behavior. While most studies of Pt nanoparticles have been in extremely small size regimes, studies of Pd nanoparticles have shown ferromagnetism in nanoparticles as large as 14 nm [51]. The sizes of the octahedral/tetrahedral sites in a 100 nm metalattice are 41.4 and 22.5 nm respectively, while for a 60 nm metalattice they are 24.8 and 13.5 nm respectively. The onset of ferromagnetism somewhere between a periodicity of 60 nm and 100 nm, therefore, is in line with previous bounds on the size of features that exhibit ferromagnetic behavior.

The shape of the hysteresis loops we observe is also in line with previous studies. All hysteresis loops observed have narrow coercivities (< 100 Oe), and a low M_R/M_S ratio. Much like the Ni metalattices, we cannot directly measure trends in H_C because different samples have different thicknesses which likely affects H_C . Another characteristic of the hysteresis that we consider is how sharply the switching occurs. The samples all have an extended switching region, but the switching becomes increasingly sharp as we decrease the metalattice size. See Table 5.2 for a summary of hysteresis properties at 3 K for metalattices of different periodicities.

In addition to the low temperature hysteresis, we considered the magnetization of the Pt metalattices as a function of temperature. Like the Ni metalattices, these are

	H_C (Oe)	M_R/M_S
Film	-	0.00
100 nm	9	0.00
60 nm	41	0.07
30 nm	98	0.15
14 nm	40	0.06

Table 5.2. Magnetic properties of Pt metalattices over a range of periodicities. Film data is measured on a capped 30 nm metalattice sample. All values are taken from data at 3 K.

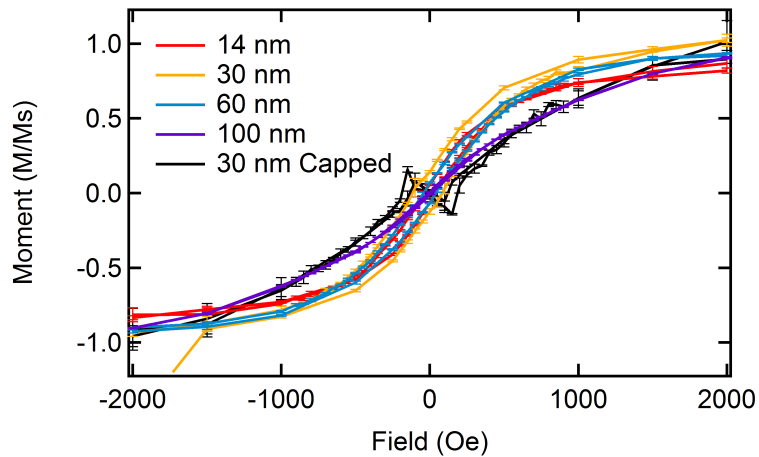


Figure 5.6. Hysteresis data for Pt metalattices over a range of periodicities. The 30 nm Capped data is indicative of Pt film behavior, with contributions from the underlying metalattice appearing as low field artifacts in the data. All curves were measured at 3 K in the in-plane orientation.

ferromagnetic over the entire temperature range considered, showing no indication of either a Curie temperature or a superparamagnetic blocking temperature. This is the same behavior observed for Pt nanoparticle and nanowires. Temperature curves are shown in Fig. 5.12, and have global offsets removed, determined for each sample such that the ZFC data has a zero magnetization. The 100 nm and Capped 30 nm samples show very little temperature dependence, which is unexpected since a paramagnet should decrease in magnetization with increasing temperature. It is likely that because the signal from these samples is quite low that the decrease in magnetization is indistinguishable above the noise. The metalattice samples do show a slight relaxation with increasing temperature, but again it is difficult to discern any trends from the small signals present.

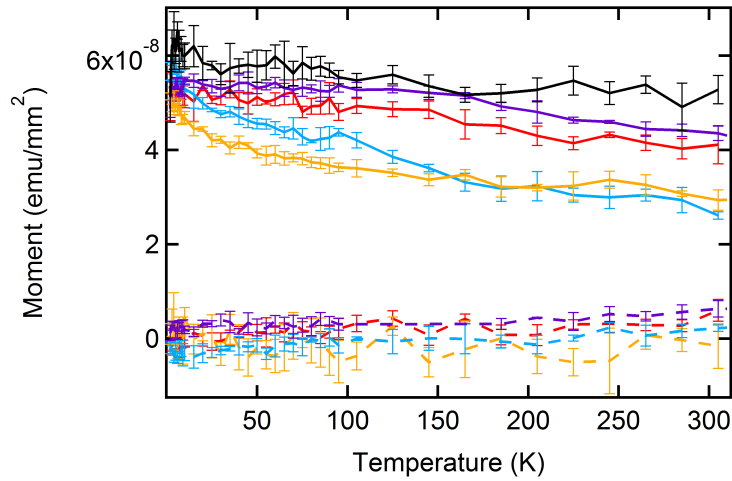


Figure 5.7. Temperature dependence for Pt metalattice samples measured both using an FC (solid line) and ZFC (dashed line) initialization. Global offsets are removed such that the ZFC data starts at zero magnetization, and FC curves are offset by the same value. As we did not measure a ZFC curve on the capped 30 nm sample, this data is offset is estimated such that the FC data begins at roughly the same value as the other samples.

We measured hysteresis loops at a variety of temperatures to confirm that the magnetization is temperature independent as indicated by the temperature data. We do not observe any significant decrease or change in hysteresis as a function of temperature from 3 K to 305 K. Hysteresis curves for a 60 nm Pt metalattice normalized to M_S at 3 K are shown in Fig. 5.8.

In summary, metalattices infiltrated with Pt match previous observations of ferromagnetism in Pt reported in literature. Hysteresis loops have $H_C < 100$ Oe with a low M_R/M_S ratio, and the magnetization is temperature independent up to room temperature. The size of metalattice necessary for the onset of ferromagnetism is also in agreement with observations of nanoparticles. Since these are fully interconnected systems, measurements such as magneto-transport can be performed that would be impossible on isolated nanoparticles. The spheres could be etched out and the surfaces could be functionalized to study interface effects. Additionally, measurements in different sample orientations could be performed to study anisotropic effects due to the metalattice geometry. These samples could provide an interesting platform to study many facets of magnetism in Pt nanostructures.

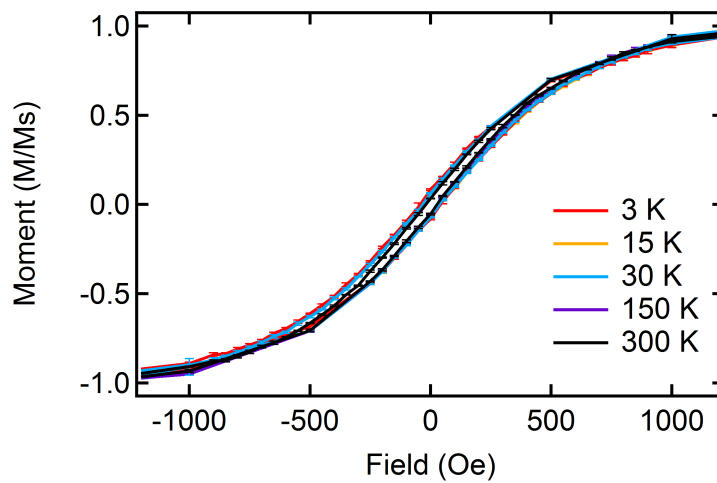


Figure 5.8. Hysteresis data for a 60 nm Pt metalattice sample taken at different temperatures ranging from 3 K to 300 K, showing little to no variation with temperature.

5.4 Palladium Metalattices

As discussed in Chapter 1, another metal that shows induced ferromagnetism in nanostructures is Pd [51,54], located between Ni and Pt on the periodic table. Previous studies on magnetism in Pd nanoparticles with twin defects [53] show no significant difference from the magnetism in Pt nanoparticles with similar defects [52]. This leads us to expect our Pd metalattices to have the same qualitative characteristics as similarly prepared Pt metalattices. As the magnetism in Pd structures is theoretically understood to be either due to defects in the nanoparticles or due to surface effects, there have been multiple investigations of the effect of altering the surfaces of Pd nanoparticles as well. It has been shown for Pd nanoparticles that the magnetism can be tuned from ferromagnetism to superparamagnetism by capping the nanoparticles and that by using different capping layers the T_C can be lowered slightly below room temperature [101].

Pd metalattices are fabricated in the same way as Pt metalattices, using template periodicities of 14 nm, 30 nm, and 60 nm. Multiple lattices of each size were fabricated, so to distinguish different depositions samples will be referred to as 60a, 60b, and 60c for 60 nm samples, 30a and 30b for 30 nm samples, and 14c for 14 nm sample. Samples with the same letter designation were deposited around the same time in similar conditions. The Pd depositions place more strain

on the templates than the Pt depositions, which can cause the Pd metalattices to peel off of the substrates if the deposition rate is not carefully controlled by the temperature and hydrogen concentrations used. It is also more difficult to remove the Pd layer by ion milling, so some measured samples (60a, 30a) may have nanoparticles remaining on the surface. We also fabricated and measured control samples consisting of a continuous Pd film and Pd nanoparticles dispersed on a Si substrate. Hysteresis and temperature sweeps are measured using SQUID magnetometry in the same way as for previous samples.

We first consider the low temperature hysteresis. The control Pd film shows a paramagnetic signal, similar to the capped 30 nm Pt. The control Pd nanoparticles dispersed on a Si substrate show hysteresis at low temperature. Compared to previously reported hysteresis of Pd nanoparticles, we observe a relatively high M_R/M_S value, or squareness value. H_C is still low, around 64 Oe. We observe two distinct regimes of magnetic behavior in the Pd metalattice samples. Samples 60b and 60c show the same qualitative hysteresis behavior observed in the Pt samples, with low H_C and squareness (See Fig. 5.9, right). This matches our original expectation of little deviation between the behavior in Pt and Pd samples. However, samples 60a and 30a show distinct hysteresis patterns. Like the Pd nanoparticle sample, these samples have a higher squareness value and more sharpness in the switching. They also show an increase in coercivity over the nanoparticle sample. This makes it unlikely that the signal we observe is due solely to nanoparticles that may have been left behind during the cap removal process. The increase in coercivity indicates some kind of ordering or interaction between magnetic elements. Finally, samples 30b and 14c show what appears to be a mixture of these two phases, with a temperature independent component that shows a low squareness and H_C , and an additional low temperature component with higher squareness and sharper switching that decreases with temperature. Fig. 5.9, left panel, shows the low temperature hysteresis for samples 60a, 30a, and 14c. Since 14c showed a mixture of the two phases, we subtracted the signal at 300 K from the signal at 3 K to remove the temperature independent component of the signal, leaving the curve shown as the temperature dependent, square component. Coercivity and squareness values for these samples are summarized in Table 5.3.

To more clearly justify this background subtraction, consider the data presented in Fig. 5.10. The saturation magnetization of the 14 nm sample decreases with

	Thickness (nm)	H_C (Oe)	M_R/M_S	$H_C, 2$ (Oe)	$M_R/M_S, 2$
Film	-	0	0.00	-	-
Nanoparticles	-	64	0.27	-	-
60a	-	157	0.35	-	-
60b	-	40	0.07	-	-
60c	150	43	0.05	-	-
30a	-	142	0.37	-	-
30b	-	104	0.47	58	.08
14c	200	16	0.14	69	.08

Table 5.3. Magnetic properties of Pd metalattices over a range of periodicities. H_C and M_R/M_S represent the low temperature, temperature dependent portion of the magnetization. $H_C, 2$ and $M_R/M_S, 2$ represent the temperature independent portion of the magnetization, measured at 300 K.

temperature until reaching a stable value by around 30 K. The 300 K measurement that we use as a background is plotted with the narrow hysteresis loop of sample 60c to demonstrate the similarities between the curves, supporting our assertion the temperature independent component of 14c has similar origins to the magnetization in 60c.

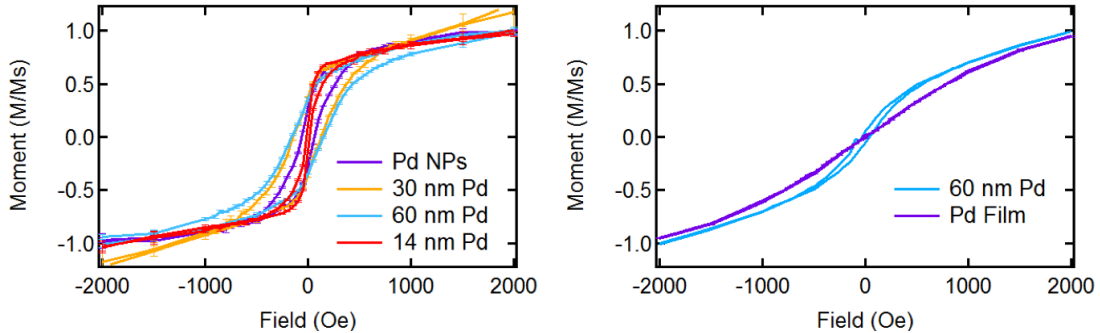


Figure 5.9. Low temperature hysteresis on Pd metalattices showing two distinct regimes of magnetic behavior. The right plot shows a 60 nm sample and continuous Pd film with behavior matching the Pt samples. The left plot shows various samples with higher squareness and sharper switching in the hysteresis.

When considering hysteresis curves over a range of temperatures, samples 60b and 60c do not show significant temperature dependence beyond a slight decrease in coercivity and squareness with increasing temperature. There is also a temperature independent component in samples 30b and 14c, as demonstrated in Fig. 5.10. This temperature independent component matches the behavior observed in Pt

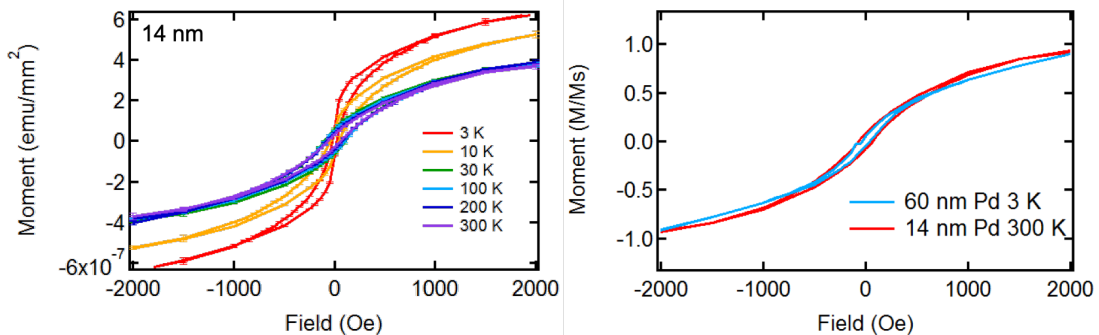


Figure 5.10. Left: Hysteresis of sample 14c measured at a variety of temperatures. Right: Hysteresis of sample 14c at 300 K in red and 60c at 3 K in blue.

samples. Samples 60a, 30a, 30b, and 14b show an additional temperature dependent component, strongest at low temperature and decreasing to zero between 30 and 60 K, depending on the sample. The temperature dependence of 60a and 30a using a linear background subtraction, and the 14c sample using the magnetic response at 300 K as a background subtraction, are shown in Fig. 5.11. M_S decreases with increasing temperature, as does H_C . The 3 K curve for sample 14c is similar to higher temperature measurements of the other samples. The relative narrowness of the 14c hysteresis at 3 K is because this sample has a lower transition temperature, so 3 K is closer to the transition temperature for 14c than it is for the larger periodicity metalattices.

Temperature curves for samples 60b and 60c are not shown here but match the temperature dependence shown in Fig. 5.7. Magnetic measurements of the temperature response of samples 60a, 30a and 14c are shown in Fig. 5.12. Unlike previously presented data, these samples show a marked decrease in magnetization in the FC temperature sweeps, and corresponding peaks in the ZFC temperature sweeps. This temperature dependence agrees with the temperatures at which the hysteresis vanishes in Fig. 5.11. The transition temperature decreases with decreasing metalattice periodicity. For individual nanoparticles, various transition temperatures often decrease with decreasing particle size. This is because smaller particles take less energy to reverse magnetization and as such are more susceptible to thermal effects than larger particles at the same temperatures.

The peaks in the ZFC temperature sweeps combined with the temperature dependence in the hysteresis suggest superparamagnetic behavior in these samples. However, both of these could also be due to disordered ferromagnetism. To confirm

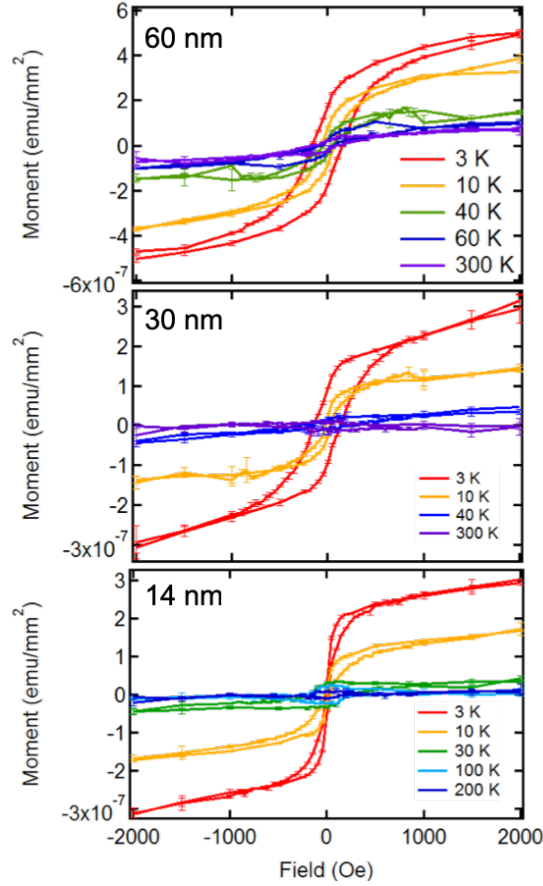


Figure 5.11. Temperature dependent hysteresis curves for 60 nm, 30 nm, and 14 nm metalattice samples. 60 nm and 30 nm samples use a diamagnetic background subtraction, and 14 nm sample uses the 300 K hysteresis as a background subtraction.

superparamagnetism, it is necessary to perform a thermoremanent magnetization (TR) measurement [102]. First, the system is carefully demagnetized to minimize unintended magnetic fields in the system. Then, the sample is cooled from room temperature to 3 K in the presence of a saturating external field (2 T). Like the FC temperature sweeps, this initializes the sample in an aligned magnetic state at low temperature. Unlike the FC temperature sweeps, the measurement field is then set to a low value (< 2 Oe) to minimize the influence of the measurement field on the system. The temperature is increased to some value T_{lim} and then decreased back to 3 K. Then it is increased again to a larger T_{lim} and again decreased. This process is repeated for successively larger values of T_{lim} until the system has been brought to a sufficiently high temperature to completely randomize the magnetization. This

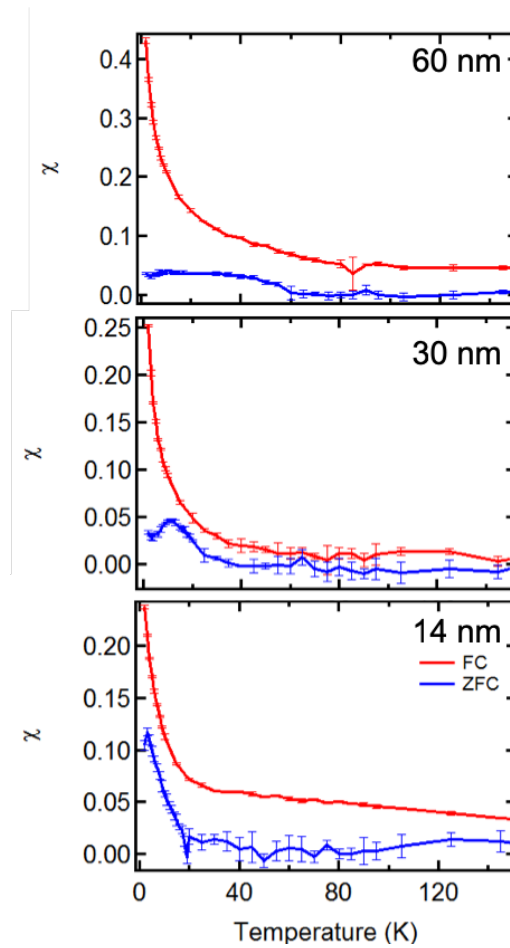


Figure 5.12. FC (red) and ZFC (blue) temperature curves for 60 nm (top), 30 nm (middle), and 14 nm (bottom) Pd metal lattice samples.

type of measurement lets us distinguish between thermally reversible magnetization mechanisms like ferromagnetism, and thermally irreversible magnetization mechanisms like superparamagnetism. For a superparamagnet, the magnetization decreases as we increase the temperature, and remains approximately constant as we then decrease the temperature. Once the blocking temperature has been exceeded, the small measurement field is insufficient to provide a preferred alignment to the superparamagnetic moments, leading to a randomized net magnetization. Thus the effective blocking temperature for a superparamagnetic sample, in addition to appearing as a peak in a ZFC temperature sweep, will also appear as the point in a TR sweep where the magnetization becomes repeatable through successive temperature cycles. For a ferromagnet, the magnetization would remain

approximately constant as we increase and decrease the temperature until the Curie temperature is exceeded, at which point the magnetization would go to zero above the Curie temperature but follow the same path when cooled back below the Curie temperature.

TR data for samples 60a and 30a are shown in Fig. 5.13. These curves qualitatively match our expectations for superparamagnetic samples, with the measured blocking temperatures matching the peaks found in the ZFC temperature sweeps. This supports that this additional phase in the Pd samples is due to superparamagnetism. The source of this phase is unclear. It could be due to isolated nanoparticles forming in the template due to incomplete infiltration. It could be from an interconnected metalattice with a granular structure. It could also be an effect from how the magnetism is induced in the metalattice. Further characterizations are necessary to fully determine the source of this behavior.

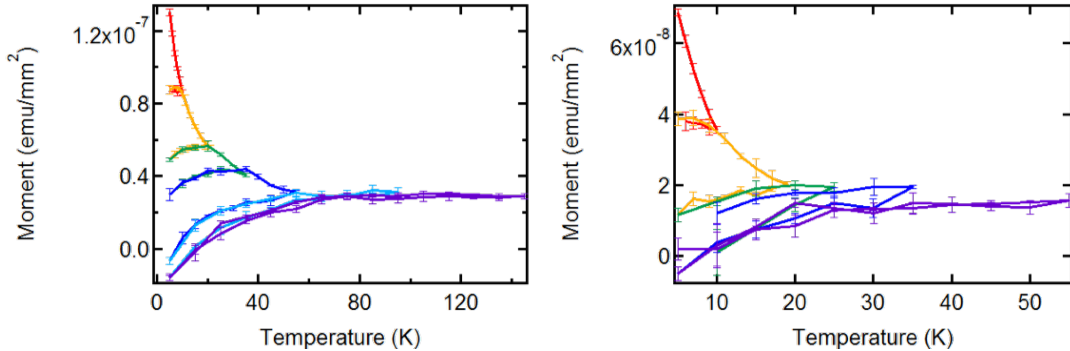


Figure 5.13. TR curves for 60 nm (left) and 30 nm (right) Pd metalattice. Red is for the first round of increasing and decreasing temperature, yellow for the second, and so on.

In conclusion, we have fabricated and measured Pt and Pd metalattices to explore confinement-induced magnetic effects. We observe two distinct regimes of magnetic response. A narrow, ferromagnetic response is observed in Pt and some Pd samples. This phase persists to room temperature and matches previous observations of Pt and Pd nanoparticles and nanowires. A superparamagnetic response with a low T_B is observed in some Pd samples, and still other Pd samples show a coexistence of the two responses. The source of this superparamagnetic response is as of yet undetermined, but it is qualitatively different from observed behavior from Pd nanoparticles reported in literature. Further investigations into these systems are required to characterize this behavior. Other useful additional

investigations include studying anisotropy and surface functionalization of Pt and Pd metalattices.

Appendix A | Details of Fabrication

A.1 Introduction

Chapter 2 introduced the basic process of creating the lithographically defined squares and artificial spin ice arrays studied in Chapters 3 and 4. This appendix describes the detailed procedures used for sample fabrication in the Penn State nanofabrication facilities, for samples fabricated using bilayer resist stacks.

A.2 Lithography

As these samples were fabricated using shared user facilities, it is important to be aware of contamination in shared equipment. In particular, shared glassware made available by the fab used for wet chemistry has likely been used for a number of different chemicals and may still contain trace contaminants. While the samples in this dissertation were fabricated using shared glassware, in the ideal scenario one would have glassware specifically designated for each specific chemical used in the fabrication process. This would minimize the chances of cross contamination.

The first step in sample fabrication is appropriate preparation of the substrates. Any dust or debris on the substrate will prevent the deposition of a smooth layer of resist, which is necessary for good lithography. We begin by cleaving approximately 1" to 2" squares of Si wafer for substrates. Before continuing, we set the temperatures for three hot plates to ensure they are at the correct temperatures when needed. The plates are set to 186°C, 216°C, and 107°C, which should result in surface temperatures of 180, 210 and 100. To prepare the substrate:

1. Rinse wafer with Acetone and then soak for 60 s.

2. Rinse wafer with Isopropanol and then soak for 60 s.
3. Rinse wafer with distilled water and then soak for 60 s.
4. Remove wafer from water bath and dry using compressed Nitrogen gas. Sample should be placed face up on a cleanroom wipe to absorb water from the back of the sample. Hold an edge of the sample with a pair of blunt metal tweezers. During the drying process, release the sample from the tweezers, dry the tweezers, and pick of the sample from a different edge to ensure the entire sample is dried.
5. Place the dried wafer on a hot plate at 100°C for one minute to fully dehydrate the sample surface.
6. Allow the wafer to cool to room temperature before proceeding.

Once the wafer is cleaned, the next step is to spin on the resist. This step is carried out using a spinner bench. We begin by placing the substrate on the vacuum chuck and spinning it at a low speed to check that it is properly centered. If the substrate is not well centered, the resist film will not be uniform. Any adjustments to centering are made, and the sample is revolved again at a low speed. This process is repeated until the sample is well centered.

The first layer of resist is PMGI SF2:

1. Fill a pipette with resist to be dispersed on sample
2. Spin the wafer slowly (500 rpm) and disperse the resist on the sample. After the pipette has been emptied, the lid of the resist bottle may be placed over the hole on the spinner bench.
3. Increase the speed to 4000 rpm to allow the resist to form into a thin film. Hold for 45 sec at this speed.
4. Ramp the spin speed to 0 at 5000 rpm/min
5. Ensure that there is no resist on the back of the sample. Any resist on the back of the sample should be removed before baking.
6. Place the wafer on the hot plate at 210°C for 5 min

7. Remove wafer and allow to cool 1 min

The second layer of resist is PMMA A2:

1. Fill a pipette with resist to be dispersed on sample
2. Spin the wafer slowly (500 rpm) and disperse the resist on the sample. After the pipette has been emptied, the lid of the resist bottle may be placed over the hole on the spinner bench.
3. Increase the speed to 4000 rpm to allow the resist to form into a thin film. Hold for 60 sec at this speed.
4. Ramp the spin speed to 0 at 5000 rpm/min
5. Ensure that there is no resist on the back of the sample. Any resist on the back of the sample should be removed before baking.
6. Place the wafer on the hot plate at 180°C for 5 min
7. Remove wafer and allow to cool 1 min

At this point the resist is complete, and the sample is ready for thermal gold deposition. We deposit a thin layer of gold using the Kurt J. Lesker Lab-18 evaporator. Details of evaporation will be covered later. The specific parameters used for this deposition are 100 Å of gold deposited at a rate of 1 Å/s while rotating the substrate.

After the gold layer has been deposited, the sample is ready for e-beam exposure. The first step in creating an e-beam pattern is to design the pattern in the computer using the L-Edit software. Once the pattern has been designed in the computer, it must be fractured. Fracturing is the process by which the pattern is translated into a form that the e-beam instrument can use to expose the pattern. It removes overlaps in the pattern, translates curves into straight lines, and so forth. Appropriate beams are also selected; small beams for small features and large beams for large ones. This allows a significant improvement in write time over using a small beam for all features. In the artificial spin ice samples, a small beam is used for the actual arrays and a large beam is used to write a set of finder bars around the arrays to help locate them in the microscopy set up. Once the fractured pattern is

prepared, the sample is loaded. Metal clips are used to attach the sample to the sample holder. The Faraday cup in the corner of the sample holder is used as the reference point for location. Before loading the sample into the e-beam instrument, the location of the center of the desired area for the pattern relative to the Faraday cup is measured. This will be entered as a parameter in the software to ensure the pattern is exposed on the most optimal location of the sample. The sample is loaded into the e-beam instrument and exposed. After multiple tests, we settled on an e-beam dose of $600 \mu\text{C}/\text{cm}^2$.

Once the pattern has been exposed, the sample must be developed to remove the polymer that was exposed using lithography and finish creating the mask for deposition. There are three layers currently on the sample (PMGI, PMMA, and Au), each of which requires a different process to remove (Au) or develop (PMGI/PMMA). The gold layer is removed in the wet chemistry bay, while the development steps are carried out in the lithography bay.

To remove the gold layer:

1. Soak the wafer in TFA Gold Etch for 10 - 15 s. When placing the wafer in the bath, make sure that the wafer actually sinks under the surface. It is best to insert it at a slight angle. Try not to agitate the wafer at this point.
2. Place the wafer into a bath of distilled water, then rinse with distilled water.
3. Dry the wafer with compressed nitrogen.

At this point, all remaining chemical baths should be prepared before starting the development process. Once the process is started, it is best to move through quickly and smoothly without the extra downtime required to prepare additional chemical baths. Chemicals required for development are MIBK 1:3, Isopropanol, Distilled Water, Developer 101A, and a second bath of Distilled Water. Take care throughout development to minimize physical agitation of the samples. For small features such as those created for these projects, agitation can destroy the pattern quality. Development time can be adjusted to tune the final feature size, but the parameters used for the samples in this dissertation are as follows.

To develop the PMMA:

1. Soak wafer in MIBK 1:3 for 90 s.

2. Soak wafer in Isopropanol for 60 s.
3. Soak wafer in Distilled Water for 60 s. This stops the development process of this layer and helps ensure that it will not be overdeveloped.
4. Dry wafer with compressed nitrogen before beginning the next development step.

To develop the PMGI:

1. Soak wafer in Developer 101A for 60 s.
2. Soak wafer in Distilled Water for 60 s.
3. Dry wafer with compressed nitrogen.

At this point, development is complete and samples are ready for film deposition. Samples should now be inspected with an optical microscope to ensure that the pattern is well developed and there is no residual resist or debris on the sample surface. In the case of residual resist or debris, rinse samples with water and dry samples until debris appears removed. To ensure sample quality, it is necessary to perform all of these steps as quickly as possible, preferably within a 24 hour time period. Extended periods of time between steps can cause resist to degrade and affect characteristics such as edge roughness of features.

Details of film deposition will be covered in the next section. The last step in the lithography process is lifting off the samples, leaving only the desired pattern. As with the development step, it is best to prepare all chemical baths before beginning the lift off process. Required chemicals are Acetone, PRS - 3000, Isopropanol, and Distilled Water. Unlike the development process, it is best to mildly agitate the sample throughout the lift off process, to ensure that the resist is fully removed from the samples.

To lift off the sample:

1. Begin warming up a water bath to 80°C. Do not let the temperature exceed 90°C as this is nearing the flash point of PRS and PG remover.
2. Soak sample in Acetone for 5 min, with mild agitation
3. Place sample in a bath of PRS-3000 at room temperature

4. Place container of PRS-3000 in hot water bath for 55 min. For these samples, the water bath was at approximately 76°C when the PRS was placed in the bath. It is also possible to pre-warm the PRS in the water bath before inserting the sample.
5. Remove the PRS from the hot water bath and place into bath sonicator.
6. Sonicate for 30 to 60 s in 15 s intervals, checking after each sonication whether the sample appears to be fully lifted off. Samples used in this dissertation were sonicated for 45 s.
7. Check the quality of lift off using an optical microscope. If residual resist remains, the sample can be returned to the sonicator for additional time.

A.3 Evaporation

The Kurt J. Lesker Lab-18 evaporator at Penn State is used for multiple steps in the fabrication process. It is used to deposit the 10 nm gold layer before e-beam as well as Py films. Evaporation can also be used to deposit multilayer samples, but none of the samples used in this dissertation were deposited that way. Multilayer samples deposited using evaporation have higher coercivities than those deposited using sputtering. To deposit quality multilayers using evaporation, the shutter must be manually closed at the end of each layer because the layers are too thin for the automatic shutter control to be sufficiently accurate. While this leads to better quality samples, we have found it is difficult to be consistent between depositions and it is not worth the extra time required.

Operation of the evaporator is a straightforward process. We begin by using Kapton tape to secure the sample to a holder wafer. The sample is placed close to the center of the wafer, and minimal tape is used. Two small strips on the corners of the sample are sufficient. Using excessive amounts of tape can lead to outgassing and increase the time it takes for the load lock to pump down.

Begin by venting the load lock of the evaporator. Once it is vented, place the sample face down in the holder ring in the load lock. Be sure the lid is well seated, and pump the load lock back down to vacuum. At this point, the sample can be transferred into the process chamber.

Once the sample is loaded in the process chamber, the appropriate deposition sequence can be selected for the desired element. The deposition rate and target thickness should be entered. Also, stage rotation should be selected or unselected depending on the situation. For continuous films, stage rotation helps to ensure a uniform deposition. For small features, stage rotation negatively affects the edge profile and should be turned off. Finally, the deposition temperature must be verified. Film samples are deposited at 20°C. For deposition of patterned features, the stage temperature should be set to 0°C, to minimize damage to the resist by the deposition of hot material.

Evaporation parameters used for Py underlayers are a target thickness of 150Å deposited at a rate of .5Å/s at a deposition power of 32 - 42 mA (the power varies based on what is necessary to achieve the target deposition rate).

After the film has been deposited, the sample is removed from the process chamber back to the load lock, the load lock is vented, and the sample is unmounted. At this point, the sample is ready for whatever the next step in the process is. For gold layers, that is e-beam exposure, for Py underlayers that is spinning on resist, and for multilayers that is lift off. It is a good idea to clean the sample surface before proceeding, to ensure there is no dust or debris on the sample.

A.4 Sputtering

Sputtering of multilayer samples is carried out at Argonne national lab. Deposition rates for each element were Pt 0.7Å/sec, Co 0.3Å/sec, and Ti 0.7Å/sec. Attempts to deposit multilayers at Penn State by sputtering led to inconsistent results.

Appendix B | Computational Documentation

B.1 Introduction

This appendix describes the different computational methodologies used to analyze the data in this dissertation, as well as to generate the micromagnetic simulations. Code is written in a number of programming languages including LabVIEW, Go, and python. Descriptions of the programming language, basic algorithms, relevant parameters, and order of analysis are included in more detail by section. At the time of writing this dissertation, all current LabVIEW programs are saved in directory ModularMoke Analysis_180911 and are in process of being backed up in the Samarth Group git repository. All micromagnetics code is saved in the Kempinger_S folder on the lab computer specifically set aside for micromagnetics simulations. Python code is saved on Box.

Describing the entire existing database of code would be worthy of a dissertation on its own. This appendix is not meant to provide an exhaustive list, but rather an introduction to the most used programs; namely, those that allow us to go from an image to a database of switching fields. Once the database is generated, all subsequent analysis consists of fairly straightforward numerical calculations based on island locations and states. This could be carried out in any programming language in a variety of ways. The algorithms to find nearest neighbor correlations are included in this appendix but other analyses are excluded for brevity.

B.2 Location Finding and Datastream Generation

Arguably the most critical step in the analysis process is accurately locating the islands in an image. If accurate locations are not found, the rest of the analysis will be inaccurate and incorrect. There are three steps to analysis and datastream generation. Finding the locations, finding the shifts, and extracting the data to create the datastreams. Steps 2 and 3 are actually run as sub-programs within the program that controls step 1. To run these programs more efficiently, there are parent programs labeled Auto_1-3_Demag only and Auto_1-3_HystOnly that will run through all previously analyzed demagnetization or hysteresis datasets within the selected parent folder. There is also a program called Auto_1-6_FullAnalysis that will find not only the datastreams but also the database of switching fields for the hysteresis data. This structure was designed to efficiently analyze large amounts of data. In general, throughout the programs designed, any program XXX that needs to be run with identical parameters on many sets of data will have a corresponding parent program entitled Auto_XXX.

Filename: 1.0_IslandLocationGenerator_160922

Relevant parameters: File Directory, Slice Thickness, UpperThresh, LowerThresh, Thresh (fit), Use Background?, HystBackground, DemagBackground

Description: This is the initial location finding program. *File Directory* is the directory in which data is saved during the data collection. The first step is to subtract the background, which is an image taken on a bare area of substrate with identical parameters to the experimental image. This subtraction removes inhomogeneity in the image due to inhomogeneity in the beam profile, which makes the thresholding in a later step more accurate. The background subtraction can be turned on and off using *Use Background?*, and the directories containing the background data are listed in *HystBackground* and *DemagBackground*. The background subtracted images are divided into row and column slices with thickness *Slice Thickness* and a peak finding algorithm is used to find potential island locations in each slice. The slice thickness is set to 5 for small lattice spacing arrays but can be increased for arrays with larger lattice spacings, up to 18 for 800 nm lattice spacing arrays. Larger slice thicknesses make the program run faster. *Thresh (fit)* controls the minimum height a peak must have to be considered a potential location.

This is usually set to zero, except for on samples with Py layers. The difference in reflectivity due to the Py layer leads to islands appearing darker and so the fit threshold is set to -300. The potential locations are all listed, and potential islands within a certain distance are averaged together to represent the actual location of the island. Finally, the maximum intensity value in a 5 pixel box around the island location is found and background islands are filtered out by setting *UpperThresh* and *LowerThresh* to an appropriate range to only include islands in the array. Usually, with our background subtraction, this range is approximately 600 on the lower end and 5000 on the upper end. This does not work for arrays on Py because the background reflectivity is too high.

Filename: 2.0_AssignShifts_150616

Relevant parameters: Slice Thickness, StartCol, StartRow, length

Description: After finding the locations, the shift between sequential images is found to track islands throughout an entire data set. This and all other programs also have a file directory parameter to tell the program which data to analyze. *Slice Thickness* should be the same value as used for the location finding program and is tied to the same control since this program is run as a subprogram in the location finding program. Only a small subsection of the array is used to find the shifts, to save time on location finding. Since the islands are fixed to a substrate, finding the shifts of a small section is sufficient to find the shifts of the entire array. The small section used is determined by *StartCol*, *StartRow*, and *length*, which control the location and size of the region respectively. By default, these are set to 400, 400, and 100 as we have found those parameters consistently work well. However, these could be adjusted if necessary for future samples. The locations of the islands are found in the small subset in the same way as for the whole array, without the need for the final intensity filtering step since we are restricting our search to an area that does not include large sections of substrate. The shifts from the previous image are found by subtracting the new locations from the previous locations, and this process is repeated throughout the sweep. Shifts from image to image are summed to find shifts from the original locations.

Filename: 3.0_Compiled_Updated_DATE_CHARACTERISTICS

Relevant parameters: Box Size, Adjustment

Description: Once the locations and shifts have been found, the data is converted to datastreams. The two important parameters in this process control how large of a box we are looking for the islands in and what kind of fine adjustment we apply. A box around each island location with a size of twice the input parameter *Box Size* is drawn. We use square boxes for simplicity but in some ways box size corresponds to the radius of our area. To ensure the most accurate value and minimize noise, especially due to errors in the location finding, we then extract a smaller box with the side length decreased by *Adjustment* pixels. We raster this box through every possible position in the box size area, and take the location with the highest average value as our data point because the center of an island should be the brightest area. We use a box size of 5 and an adjustment of 4, leading to a final box size of 6 pixels on a side. This is carried out for every island in every image to create the data stream. Because of the time it takes to load a new image, this process can become incredibly time-consuming depending on the order in which steps are carried out. We load 50 images at a time, apply the shifts to each one, and then go through an island location in all 50 images, repeating until we cover all islands. We continue this process 50 images at a time until the datastream for the entire sweep is created.

The notation of *DATE* and *CHARACTERISTICS* in the title are because there are multiple versions of this program depending on what additional location finding algorithms have been applied. These include things like locations from filtering out the extra islands in a different program for the Py (denoted threshold) or locations created from averaging locations between multiple runs to create one indexed set of locations per physical array (denoted mask). The program with the desired characteristic and the most recent date should be selected.

B.3 Hysteresis

The following programs complete the process of finding the switching fields and the nearest neighbor correlation in the hysteresis data. This covers the computational process for the basic characterizations in this dissertation. Additional analysis programs all use the database of locations and switching fields as a starting point.

Filename: 4.75_View_HystFinal_Recheck or 4.75_View_HystFinal_CHARACTERISTICS

Relevant parameters: Comparison Island Size, Comparison Island Dist, Higher, Lower, threshold, NumIter, x

Description: This program is the main program for finding island switching fields. It selects islands to use as a comparison set. These islands are taken always from the center of the array. *Comparison Island Size* islands are chosen, at a radius up to *Comparison Island Dist* from the center of the array. The data streams for each island are subtracted from every island in this set, derivatives are taken of these differences, and then the derivatives are summed. This should lead to a curve with a single sharp peak at the switching field. Of course, real data is not always so clean, so it is insufficient to simply pick the highest peak. Instead, we start by normalizing the data to the highest peak height. Then, starting in a range of *Lower* to *Higher*, the program looks for a peak of at least *threshold* in height. *Lower* and *Higher* are close to the bounds of the switching region, which allows us to disregard erroneous peaks from random fluctuations far away from reasonable island coercivities. If no peak is found in this original region, the size of the region is expanded by *x* in either direction and the search is repeated. This expansion is repeated *NumIter* times before an island is marked as having no certain switching field, denoted by a switching field value of zero. Ideally, this program should find accurate switching fields for all islands in an array but in the event that it does not, we have other programs that provide secondary checks.

Filename: HystFinalStates_Recheck_CHARACTERISTICS

Relevant parameters: Bound

Description: This program finds estimated switching fields for all islands that fail the initial switching field finding location. Islands that either have a switching field of zero or a switching field greater than *Bound* (set high enough that switching fields larger than this value are clearly erroneous). The switching field is estimated by first taking a linear fit to the high field data at positive and negative fields. The point at which the intensity transitions from being closer to the positive field fit to being closer to the negative field fit is considered the switching field for a down sweep, and vice versa for an upsweep. This is less accurate than the previous algorithm, which is why it is only used for a secondary check.

Filename: 0_Auto_6.0_OffsetSwitchingFields_CHARACTERISTICS

Relevant parameters: MaxField, MinField, StepSize

Description: This program converts the switching fields found into hysteresis loops centered at zero. First, the program is given a range over which to find the states of the array, beginning at *MinField* and going to *MaxField* in steps of *StepSize*. The program then calculates how many islands are “up” and “down” at each field in the defined range, which generates a hysteresis loop by considering what fraction of the islands are “up” as a function of applied field. The program also finds at what field the hysteresis loops passes 50% switching, the coercive field, and saves a new set of offset switching fields which are adjusted to $H - H_C$. This recenters the switching field distribution at zero so comparisons can be more easily made between different lattice spacings and geometries.

Filename: NNAnalysis_CHARACTERISTICS_DATE

Relevant parameters: NeighborNumber, Noise, Index, MaxField, MinField, StepSize, T-UP F-DOWN, Save?

Description: Much like the offset program, this program is designed to carry out analysis over a specific region from *MinField* to *MaxField* in steps of *StepSize*. This can be carried out for both up sweeps and down sweeps using the *T-UP F-DOWN* control. Data needn't be saved while optimizing parameters, so there is also a *Save?* control so that saving can be easily turned on and off. The program is designed to be used for first, second, third, or even farther neighbors using the *NeighborNumber* control. For first nearest neighbors, this is set to zero. For second to one, and so on. An island selected from the array at index *Index* and used to calculate the number and distance of nearest neighbors. This is typically accurate up to about 5 neighbors. This can be adjusted to select an island that is not too close to the edge of the array and is not missing any neighbors. The calculated neighbor distance is used, plus or minus some threshold *Noise* to find the neighbors of each island in the array. We usually use a two pixel tolerance value. Once we have the neighbor indexes of each island, we go through each field in our specified range, find the microstate of the array based on the calculated switching fields, and calculate the correlation value using the states and locations of the nearest neighbors. We also calculate the magnetization again (a straightforward matter of counting how many islands are in each state) and use this to consider the correlation as a function of magnetization. We also find the maximum value of the correlation

curve in the auto program that is used to run the correlation program through multiple runs, to consider how the correlation changes as a function of geometry and lattice spacing.

B.4 Demag

This program finds the final state of a demagnetized array, along with the nearest neighbor correlation.

Filename: 5. View_DemagFinalStatesV3_CHARACTERISTICS_DATE

Relevant parameters: Normalization, HighestPeaks?, LowerNorm, UpperNorm, UpperField, LowerField, MinX, MaxX, MinY, MaxY, NeighborNumber, Noise Index

Description: This program uses either all data at high fields or just the ending saturation based on the selection of *Normalization*. The field range used for normalization is set by *LowerNorm* to *UpperNorm*. Then data between *LowerField* and *UpperField* is averaged together and placed into histograms. A peak finding algorithm is used to find the centers of the populations. We can either select simply the highest two peaks or, if this does not correctly select the two distributions because two peaks are found in one distribution, we go through an algorithm to ensure that we are selecting peaks that are sufficiently far apart to represent the two distributions. This choice of algorithm is controlled with *HighestPeaks?*. If there are regions of the sample that failed to find the island locations properly such as in the samples with Py underlayers, they can be excluded from the analysis using the *MinX*, *MaxX*, *MinY*, and *MaxY* commands. Finally, we find the correlation in this calculated state in the same way as described for hysteresis measurements.

B.5 Micromagnetics

In this section, I will go through one example of a micromagnetic simulation code with commentary explaining the different parts of the process. The code is shown in a different font to distinguish code from commentary. This particular simulation relaxes the magnetization of a triangle of islands in a low energy configuration (two up, one down) on a square of Py initialized in a random magnetization configuration. The initial magnetization, location and number of islands, lattice spacing, and

more can be adjusted to perform simulations but all simulation code used in this dissertation has this same basic format. The language used is specific to MuMax3 but is based on the go programming language.

```
iSize := 450e-9
latSpac := 500e-9
pyThick := 15e-9
```

Parameters that might need to be frequently tuned and are used repeatedly throughout the code are defined as variables at the top of the code. This makes it easier to quickly modify the code to run the same simulation say as a function of lattice spacing. For our simulations, we have island size (*iSize*), lattice spacing (*latSpac*), and Py layer thickness (*pyThick*) as easily accessible variables at the beginning of the code.

```
// start by setting grid and cell size
totalSize_x := latSpac*2+1e-6
totalSize_y := latSpac*2+1e-6
totalSize_z := pyThick+22e-9
gridSize_x := ceil(totalSize_x*1e9/4)
gridSize_y := ceil(totalSize_y*1e9/4)
gridSize_z := ceil(totalSize_z*1e9/4)
SetCellsize(4e-9, 4e-9, 4e-9)
SetGridsize(gridSize_x, gridSize_y, gridSize_z)
OutputFormat = OVF2_TEXT
```

The first step to any micromagnetic simulation is to define the simulation area and the mesh size. We choose a total simulation size large enough to cover whatever area the islands take up plus a 1 micron buffer to try to minimize the edge effects from simulating a finite size of Py while not making the system so computationally expensive that it never relaxes. The vertical size is set using the input Py thickness and the known island thickness (which we leave constant based on an 8 layer stack with a 10 nm Pt buffer). This is defined in the *totalSize* parameters. The *gridSize* parameters tell the system how many squares we are going to be breaking the system in to, which we get by dividing the total desired size by the desired grid size. This needs to be an integer value, hence the *ceil* command. We use the calculated grid size and our chosen cell size to set the parameters in the program. The cell size chosen should be small enough that it doesn't average out important features

but large enough that it doesn't take prohibitively long to relax the magnetization. A good rule of thumb is that this needs to be smaller than the magnetic exchange length. We use cell sizes between 4 and 8 nm depending on the simulation.

```
// define the geometry
EdgeSmooth=8
island := cylinder(iSize,10.4e-9)
island1 := island.Transl(0, latSpac*(sqrt(3)/4),
pyThick/2+5.8e-9)
island2 := island.Transl(-latSpac/2, latSpac*(sqrt(3)/4),
pyThick/2+5.8e-9)
island3 := island.Transl(latSpac/2, latSpac*(sqrt(3)/4),
pyThick/2+5.8e-9)
pyLayer := cuboid(totalSize_x, totalSize_y, pyThick)
.Transl(0,0,-11e-9)
islandsPy := pyLayer.add( island1 ).add( island2 ).add( is-
land3 ).add( island4 )
SetGeom(islandsPy)
saveas(geom, "islandPair")
snapshot(geom)
```

Once the grid has been defined, we need to define the geometry. We create an example island and then create as many instances of it as are necessary to define the desired shape (2 for a pair, three for a triangle, and so on). These are translated so that they lie in the top of the designed area and are as centralized as possible. Some simple geometrical calculations are necessary to find the optimal translations for each island. The Py is defined to extend through the entire lateral area and the input thickness and is offset slightly to make room for the islands above it in the simulation. Once the geometry is defined, an image is saved to check that it appears as expected.

```
//split into py(1) and Pt/Co(2,3) regions
defregion(1,pyLayer)
defregion(2,island1)
defregion(3,island2)
defregion(4,island3)
```

Part of the reason for defining the geometry in the way we do is that it is then

easy to assign a number to each geometric component (the Py layer and each island) which can then be used throughout the program to do things like set parameters and extract aspects.

```
//set materials parameters py
Msat.setregion(1,8e5)
Aex.setregion(1,1.3e-11)
alpha.setregion(1,6.3e-3)
//set materials parameters Pt/Co
Msat.setregion(2,3.5e5)
AnisU.setregion(2, vector(0,0,1))
Ku1.setregion(2,94e3)
Aex.setregion(2,1e-11)
Msat.setregion(3,3.5e5)
AnisU.setregion(3, vector(0,0,1))
Ku1.setregion(3,94e3)
Aex.setregion(3,1e-11)
Msat.setregion(4,3.5e5)
AnisU.setregion(4, vector(0,0,1))
Ku1.setregion(4,94e3)
Aex.setregion(4,1e-11)
```

Necessary materials parameters are saturation magnetization (Msat), exchange stiffness (Aex), and anisotropy directions (AnisU) and values (Ku1). For Py, these values were taken from standard values used in literature. For Pt/Co these values were measured for a witness film corresponding to our particular Pt/Co. The values used correspond to sample 3 as that was the most fully characterized film at the time we began running simulations. The actual islands deposited on Py layers would have a slightly larger value of Msat. However this still gives us an idea of the change in behavior introduced by adding a Py underlayer.

```
// set initial magnetization
m.setregion(1,randomMag())
m.setregion(2,uniform(0,0,-1))
m.setregion(3,uniform(0,0,-1))
m.setregion(4,uniform(0,0,1))
saveas(m,"m_initial")
```

```
snapshot (m)
```

The initial magnetization can also be set on a region by region basis. This allows us to do things like initialize islands in aligned and anti-aligned states to see how the energy differs, or to initialize the Py layer in any number of states to see how it affects the final magnetization in the Py layer. In this example, the Py region is started with a random initial magnetization.

```
// relax the system and save outputs
relax()
saveas (m, "m_relaxed")
snapshot (m)
separationPoint := gridSize_z - 4
m_py := CropZ (m, 0, separationPoint)
snapshot (m_py)
saveas (m_py, "m_py")
m_PtCo := CropZ (m, separationPoint, gridSize_z)
snapshot (m_PtCo)
saveas (m_PtCo, "m_PtCo")
tableAdd (m.Comp (0).Region (1))
tableAdd (m.Comp (1).Region (1))
tableAdd (m.Comp (2).Region (1))
tableAdd (m.Comp (0).Region (2))
tableAdd (m.Comp (1).Region (2))
tableAdd (m.Comp (2).Region (2))
tableAdd (m.Comp (0).Region (3))
tableAdd (m.Comp (1).Region (3))
tableAdd (m.Comp (2).Region (3))
tableAdd (m.Comp (0).Region (4))
tableAdd (m.Comp (1).Region (4))
tableAdd (m.Comp (2).Region (4))
tableAdd (B_eff.Region (1))
tableAdd (B_eff.Region (2))
tableAdd (B_eff.Region (3))
tableAdd (B_eff.Region (4))
tableAdd (E_total)
```

```
tableSave()
```

Finally, the system is relaxed from our starting condition to a reasonable physical state representing the magnetization in the Py and the islands. There are three parts to this last set of code. First the system is relaxed using the `relax()` command. This is the most accurate way to find the magnetic state. Next, images are saved of the full relaxed state, the relaxed state of just the Py layer, and the relaxed state of just the islands. Finally, desired parameters are extracted and saved in a table. For this simulation we save all components of the magnetization as well as the effective magnetic field in each region, as well as the total energy in the simulation.

Bibliography

- [1] S. Kempinger, R. Fraleigh, S. Zhang, P. Lammert, V. Crespi, P. Schiffer, and N. Samarth. Imaging the stochastic microstructure and dynamic development of domains in perpendicular artificial spin ice. *arXiv:1904.06625*, 2019.
- [2] B. G. Sumpter, R. K. Vasudevan, T. Potok, and S. V. Kalinin. A bridge for accelerating materials by design. *Npj Computational Materials*, 1:15008 EP–, 11 2015.
- [3] National Research Council. *Beyond the Molecular Frontier: Challenges for Chemistry and Chemical Engineering*. The National Academies Press, Washington, DC, 2003.
- [4] F. Hellman, A. Hoffmann, G. S. D. Beach, E. E. Fullerton, A. H. Macdonald, D. C. Ralph, D. A. Arena, H. A. Dürr, and P. Fischer. Interface-induced phenomena in magnetism. *Reviews of Modern Physics*, 89(025006), 2017.
- [5] L. Nádvorník, M. Orlita, N. A. Goncharuk, L. Smrčka, V. Novák, V. Jurka, K. Hruška, Z. Výborný, Z. R. Wasilewski, M. Potemski, and K. Výborný. From laterally modulated two-dimensional electron gas towards artificial graphene. *New Journal of Physics*, 14, 2012.
- [6] D. A. Gilbert, B. B. Maranville, A. L. Balk, B. J. Kirby, P. Fischer, D. T. Pierce, J. Unguris, J. A. Borchers, and K. Liu. Realization of ground-state artificial skyrmion lattices at room temperature. *Nature Communications*, 6(8462), 2015.
- [7] R. F. Wang, C. Nisoli, R. S. Freitas, J. Li, W. McConville, B. J. Cooley, M. S. Lund, N. Samarth, C. Leighton, V. H. Crespi, and P. Schiffer. Artificial ‘spin ice’ in a geometrically frustrated lattice of nanoscale ferromagnetic islands. *Nature*, 439(7074), 2006.
- [8] S. Zhang, J. Li, I. Gilbert, J. Bartell, M. J. Erickson, Y. Pan, P. E. Lammert, C. Nisoli, K. K. Kohli, R. Misra, V. H. Crespi, N. Samarth, C. Leighton, and P. Schiffer. Perpendicular magnetization and generic realization of the ising model in artificial spin ice. *Physical Review Letters*, 109(8), 2012.

- [9] L. J. Heyderman and R. L. Stamps. Artificial ferroic systems: novel functionality from structure, interactions and dynamics. *Journal of Physics. Condensed Matter*, 25(36), 2013.
- [10] I. Gilbert, C. Nisoli, and P. Schiffer. Frustration by design. *Physics Today*, 54, 2016.
- [11] J. P. Morgan, C.J. Kinane, T. R. Charlton, A. Stein, C. Sánchez-Hanke, D. A. Arena, S. Langridge, and C. H. Marrows. Magnetic hysteresis of an artificial square ice studied by in-plane Bragg x-ray resonant magnetic scattering. *AIP Advances*, 2(022163), 2012.
- [12] G. M. Wysin, W.A. Moura-Melo, L. A. S. Mól, and A. R. Pereira. Dynamics and hysteresis in square lattice artificial spin ice Dynamics and hysteresis in square lattice artificial spin ice. 15(045029), 2013.
- [13] I. Gilbert, G.-W. Chern, B. Fore, Y. Lao, S. Zhang, C. Nisoli, and P. Schiffer. Direct visualization of memory effects in artificial spin ice. *Physical Review B*, 92(104417), Sep 2015.
- [14] Y. Li, G. W. Paterson, G. M. Macauley, F. S. Nascimento, C. Ferguson, S. A. Morley, M. C. Rosamond, E. H. Linfield, D. A. MacLaren, R. Macêdo, C. H. Marrows, S. McVitie, and R. L. Stamps. Superferromagnetism and domain-wall topologies in artificial 'pinwheel' spin ice. *ACS Nano*, 13(2), 2019.
- [15] L. Pauling. The structure and entropy of ice and of other crystals with some randomness of atomic arrangement. *Journal of the American Chemical Society*, 57(12), 1935.
- [16] S. T. Bramwell and M. J. P. Gingras. Spin ice state in frustrated magnetic pyrochlore materials. *Science*, 294(5546), 2001.
- [17] J. P. Morgan, A. Stein, S. Langridge, and C. H. Marrows. Thermal ground-state ordering and elementary excitations in artificial magnetic square ice. *Nature Physics*, 7:75 – 79, 11 2010.
- [18] S. Zhang, I. Gilbert, C. Nisoli, G.-W. Chern, M. J. Erickson, L. O'Brien, C. Leighton, P. E. Lammert, V. H. Crespi, and P. Schiffer. Crystallites of magnetic charges in artificial spin ice. *Nature*, 500(7464), 2013.
- [19] G. Möller and R. Moessner. Artificial square ice and related dipolar nanoarrays. *Physical Review Letters*, 96(23), 2006.

- [20] E. Mengotti, L. J. Heyderman, A. F. Rodríguez, F. Nolting, R. V. Hügli, and H.-B. Braun. Real-space observation of emergent magnetic monopoles and associated dirac strings in artificial kagome spin ice. *Nature Physics*, 7:68–74, 2010.
- [21] Y. Perrin, B. Canals, and N. Rougemaille. Extensive degeneracy, Coulomb phase and magnetic monopoles in artificial square ice. *Nature*, 540:410–413, 2016.
- [22] S. Ladak, D. E. Read, W. R. Branford, and L. F. Cohen. Direct observation and control of magnetic monopole defects in an artificial spin-ice material. *New Journal of Physics*, 13(063032), 2011.
- [23] C. Phatak, A. K. Petford-Long, O. Heinonen, M. Tanase, and M. De Graef. Nanoscale structure of the magnetic induction at monopole defects in artificial spin-ice lattices. *Physical Review B*, 83(17), 2011.
- [24] L. A. Mól, R. L. Silva, R. C. Silva, A. R. Pereira, W. A. Moura-Melo, and B. V. Costa. Magnetic monopole and string excitations in two-dimensional spin ice. *Journal of Applied Physics*, 106(6), 2009.
- [25] V. Kapaklis, U. B. Arnalds, A. Farhan, R. V. Chopdekar, A. Balan, A. Scholl, L. J. Heyderman, and B. Hjörvarsson. Thermal fluctuations in artificial spin ice. *Nature Nanotechnology*, 9:514–519, 2014.
- [26] A. Farhan, P. M. Derlet, A. Kleibert, A. Balan, R. V. Chopdekar, M. Wyss, L. Anghinolfi, F. Nolting, and L. J. Heyderman. Exploring hyper-cubic energy landscapes in thermally active finite artificial spin-ice systems. *Nature Physics*, 9:375–382, 2013.
- [27] Zoe Budrikis. *Disorder, edge, and field protocol effects in athermal dynamics of artificial spin ice*, volume 65. Elsevier Inc., 1 edition, 2014.
- [28] K. K. Kohli, A. L. Balk, J. Li, S. Zhang, I. Gilbert, P. E. Lammert, V. H. Crespi, P. Schiffer, and N. Samarth. Magneto-optical Kerr effect studies of square artificial spin ice. *Physical Review B*, 84(180412), 2011.
- [29] I. Gilbert, G.-W. Chern, S. Zhang, L. O’Brien, B. Fore, C. Nisoli, and P. Schiffer. Emergent ice rule and magnetic charge screening from vertex frustration in artificial spin ice. *Nature Physics*, 10:670 – 675, 2014.
- [30] J. Drisko, T. Marsh, and J. Cumings. Topological frustration of artificial spin ice. *Nature Communications*, 8(14009), 2017.
- [31] W. R. Branford, S. Ladak, D. E. Read, K. Zeissler, and L. F. Cohen. Emerging chirality in artificial spin ice. *Science*, 335(6076), 2012.

- [32] E. Mengotti, L. J. Heyderman, A. Bisig, A. Fraile Rodríguez, L. Le Guyader, F. Nolting, and H. B. Braun. Dipolar energy states in clusters of perpendicular magnetic nanoislands. *Journal of Applied Physics*, 105(11), 2009.
- [33] R. D. Fraleigh, S. Kempinger, P. E. Lammert, S. Zhang, V. H. Crespi, P. Schiffer, and N. Samarth. Characterization of switching field distributions in Ising-like magnetic arrays. *Physical Review B*, 95(14), 2017.
- [34] A. May, M. Hunt, A. Van Den Berg, A. Hejazi, and S. Ladak. Realisation of a frustrated 3d magnetic nanowire lattice. *Communications Physics*, 2(13), 2019.
- [35] G Hukic-Markosian, Y Zhai, D. E. Montanari, S. Ott, A. Braun, D. Sun, Z. V. Vardeny, and M. H. Bartl. Magnetic properties of periodically organized cobalt frameworks. *Journal of Applied Physics*, 116(013906), 2014.
- [36] A. A. Mistonov, N. A. Grigoryeva, A. V. Chumakova, H. Eckerlebe, N. A. Sapoletova, K. S. Napolskii, A. A. Eliseev, D. Menzel, and S. V. Grigoriev. Three-dimensional artificial spin ice in nanostructured Co on an inverse opal-like lattice. *Physical Review B*, 87(220408), 2013.
- [37] I. S. Dubitskiy, A. V. Syromyatnikov, N. A. Grigoryeva, A. A. Mistonov, N. A. Sapoletova, and S. V. Grigoriev. Spin-ice behavior of three-dimensional inverse opal-like magnetic structures: Micromagnetic simulations. *Journal of Magnetism and Magnetic Materials*, 441:609–619, 2017.
- [38] Y. Liu, S. Kempinger, R. He, T. D. Day, P. Moradifar, S. E. Mohny, N. Alem, N. Samarth, and J. V. Badding. Confined Chemical Fluid Deposition of Ferromagnetic Metalattices. *Nano Letters*, 18(1), 2018.
- [39] Robert C O’Handley. *Modern magnetic materials : principles and applications*. New York ; Chichester : Wiley, 2000. "A Wiley-Interscience publication."
- [40] J. E. Han and V. H. Crespi. Abrupt Topological Transitions in the Hysteresis Curves of Ferromagnetic Metalattices. *Physical Review Letters*, 89(197203), 2002.
- [41] Y. Hao, F. Q. Zhu, C. L. Chien, and P. C. Searson. Fabrication and Magnetic Properties of Ordered Macroporous Nickel Structures. *Journal of the Electrochemical Society*, 154(2), 2007.
- [42] E. O. Lachman, A. F. Young, A. Richardella, J. Cuppens, H. R. Naren, Y. Anahory, A. Y. Meltzer, A. Kandala, S. Kempinger, Y. Myasoedov, M. E. Huber, N. Samarth, and E. Zeldov. Visualization of superparamagnetic dynamics in magnetic topological insulators. *Science Advances*, 1(10), 2015.

- [43] A. Pereira, J. L. Palma, J. C. Denardin, and J. Escrig. Temperature-dependent magnetic properties of Ni nanotubes synthesized by atomic layer deposition. *Nanotechnology*, 27(34), 2016.
- [44] C. B. Murray, S. Sun, H. Doyle, and T. Betley. Monodisperse 3d (Co, Ni, Fe) Nanoparticles and Their Assembly into Nanoparticle Superlattices. *MRS Bulletin*, 26(12), 2001.
- [45] C.-J. Lin, G. L. Gorman, C. H. Lee, R. F. C. Farrow, E. E. Marinero, H. V. Do, H. Notarys, and C. J. Chien. Magnetic and structural properties of Co/Pt multilayers. *Journal of Magnetism and Magnetic Materials*, 93:194–206, 1991.
- [46] F. J. Himpsel, J. Ortega, G. Mankey, and R. Willis. Magnetic nanostructures. *Advances In Physics*, 47(4), 1998.
- [47] Chapter 5 ferromagnetism. Trinity College Dublin Teaching Material, 2018. <https://www.tcd.ie/Physics/research/groups/magnetism/teaching/>.
- [48] J. Löffler, P. Meier, B. Doudin, J.-P. Ansermet, and W. Wagner. Random and exchange anisotropy in consolidated nanostructured Fe and Ni: Role of grain size and trace oxides on the magnetic properties. *Physical Review B*, 57(2915), 1998.
- [49] F. M. Mueller, A. J. Freeman, J. O. Dimmock, and A. M. Furdyna. Electronic structure of palladium. *Physical Review B*, 1(12), 1970.
- [50] H Chen, N. E. Brener, and J. Callaway. Electronic structure, optical and magnetic properties of fcc palladium. *Physical Review B*, 40(1443), 1989.
- [51] T. Shinohara, T. Sato, and T. Taniyama. Surface Ferromagnetism of Pd Fine Particles. *Physical Review Letters*, 91(197201), 2003.
- [52] M. A. García, M. L. Ruiz-González, G. F. de la Fuente, P. Crespo, J. M. González, J. Llopis, J. M. González-Calbet, M. Vallet-Regí, and A. Hernando. Ferromagnetism in Twinned Pt Nanoparticles Obtained by Laser Ablation. *Chemistry of Materials*, 19(4), 2007.
- [53] B. Sampedro, P. Crespo, A. Hernando, R. Litrán, J.C. Sánchez López, López Cartes C., A. Fernandez, J. Ramírez, J. González Calbet, and M. Vallet. Ferromagnetism in fcc Twinned 2 . 4 nm Size Pd Nanoparticles. *Physical Review Letters*, 91(23), 2003.
- [54] X. Teng, W.-q. Han, W. Ku, and M. Hücker. Synthesis of Ultrathin Palladium and Platinum Nanowires and a Study of Their Magnetic Properties. *Angewandte Chemie*, 47:2085–2088, 2008.

- [55] MicroChem. *LOR and PMGI Resists*.
- [56] ZEON Corporation. Zep520a, 2003. <http://www.nanophys.kth.se/nanophys/facilities/nfl/resists/7-2.pdf>.
- [57] R. Fraleigh. *Direct Investigation of Collective Phenomena in Patterned Ising-like Arrays Using High-Resolution Kerr Microscopy*. PhD thesis, Pennsylvania State University, 2016.
- [58] AJA International Inc. Sputtering tutorial. <http://www.ajaint.com/what-is-sputtering.html>.
- [59] Kurt J. Lesker Company. Thin film deposition techniques and capabilities. <https://www.lesker.com/newweb/ped/techniques.cfm>.
- [60] M. McElfresh. *Fundamentals of Magnetism and Magnetic Measurements*.
- [61] J. Kerr. On rotation of the plane of polarization by reflection from the pole of a magnet. *The London, Edinburgh, and Dublin Philosophical Magazine and Journal of Science*, 3(19), 1877.
- [62] Newport Corporation. Glan-thompson calcite polarizers, 2019. <https://www.newport.com/f/glan-thompson-calcite-polarizers>.
- [63] J. Mccord. Progress in magnetic domain observation by advanced magneto-optical microscopy. *Physical Review D*, 48(333001), 2015.
- [64] S. Kempinger, R. Terry, A. Bowers, S. Abedi, R. Fraleigh, and N. Samarth. Mesoscopic size influence on domain wall motion in patterned perpendicular anisotropy magnetic films. *unpublished*.
- [65] R. Lavrijsen, M. A. Verheijen, B. Barcones, J. T. Kohlhepp, H. J. M. Swagten, and B. Koopmans. Enhanced field-driven domain-wall motion in Pt / Co₆₈B₃₂ / Pt strips. *Applied Physics Letters*, 98(13502), 2011.
- [66] P. J. Metaxas, J. P. Jamet, A. Mougin, M. Cormier, J. Ferré, V. Baltz, B. Rodmacq, B. Dieny, and R. Stamps. Creep and Flow Regimes of Magnetic Domain-Wall Motion in Ultrathin Pt/Co/Pt Films with Perpendicular Anisotropy. *Physical Review Letters*, 99(217208), 2007.
- [67] M. Kisielewski and A. Maziewski. Drastic changes of the domain size in an ultrathin magnetic film. *Journal of Applied Physics*, 93(6966), 2003.
- [68] S. Lemerle, J. Ferré, C. Chappert, V. Mathet, T. Giamarchi, and P. Le Doussal. Domain Wall Creep in an Ising Ultrathin Magnetic Film. *Physical Review Letters*, 1998.

- [69] F. Cayssol, D. Ravelosona, C. Chappert, J. Ferré, and J. P. Jamet. Domain Wall Creep in Magnetic Wires. *Physical Review Letters*, 92(107202), 2004.
- [70] M. Cormier, A. Mougin, J. Ferré, J. P. Jamet, R. Weil, J. Fassbender, V. Baltz, and B. Rodmacq. Fast propagation of weakly pinned domain walls and current-assisted magnetization reversal in He⁺-irradiated Pt/Co/Pt nanotracks. *Journal of Physics D: Applied Physics*, 44(21), 2011.
- [71] S. Emori, D. C. Bono, and G. S. D. Beach. Time-resolved measurements of field-driven domain wall motion in a submicron strip with perpendicular magnetic anisotropy. *Journal of Applied Physics*, 111(07D304), 2012.
- [72] J. Wunderlich, D. Ravelosona, C. Chappert, F. Cayssol, V. Mathet, J. Ferré, J. P. Jamet, and A. Thiaville. Influence of Geometry on Domain Wall Propagation in a Mesoscopic Wire. *IEEE Transactions on Magnetics*, 37(4), 2001.
- [73] V. Repain, J. P. Jamet, N. Vernier, M. Bauer, and J. Ferré. Magnetic interactions in dot arrays with perpendicular anisotropy. *Journal of Applied Physics*, 95(2614), 2004.
- [74] A. Kirilyuk, J. Ferré, V. Grolier, J.P. Jamet, and D. Renard. Magnetization Reversal in Ultra-Thin Films With Perpendicular Anisotropy. *Journal of the Magnetism and Magnetic Materials*, 171(1 - 2), 1997.
- [75] J P Attane, Y Samson, A Marty, J C Toussaint, G Dubois, A Mougin, and J P Jamet. Magnetic Domain Wall Propagation unto the Percolation Threshold across a Pseudorectangular Disordered Lattice. *Physical Review Letters*, 93(257203), 2004.
- [76] K. Fukumoto, W. Kuch, J. Vogel, F. Romanens, S. Pizzini, J. Camarero, M. Bonfim, and J. Kirschner. Dynamics of Magnetic Domain Wall Motion after Nucleation: Dependence on the Wall Energy. *Physical Review Letters*, 96(097204), 2006.
- [77] Y. Zhao, R. M. Gamache, G. C. Wang, and T. M. Lu. Effect of surface roughness on magnetic domain wall thickness, domain size, and coercivity. *Journal of Applied Physics*, 89(1325), 2001.
- [78] D. H. Kim, Y. C. Cho, S. B. Choe, and S. C. Shin. Correlation between fractal dimension and reversal behavior of magnetic domain in Co/Pd nanomultilayers. *Applied Physics Letters*, 82(3698), 2003.
- [79] R. Badea and J. Berezovsky. Mapping the Landscape of Domain-Wall Pinning in Ferromagnetic Films Using Differential Magneto-Optical Microscopy. *Physical Review Applied*, 5(064003), 2016.

- [80] S. B. Choe and S. C. Shin. Quantitative analysis of magnetization reversal based on time-dependent domain patterns. *Applied Physics Letters*, 70(3612), 1997.
- [81] I. A. Chioar, N. Rougemaille, A. Grimm, O. Fruchart, E. Wagner, M. Hehn, D. Lacour, F. Montaigne, and B. Canals. Non-universality of artificial frustrated spin systems. *Physical Review B*, 90(064411), 2014.
- [82] H. B. Braun. Thermally activated magnetization reversal in elongated ferromagnetic particles. *Physical Review Letters*, 71(3557), 1993.
- [83] Y. Telepinsky, V. Mor, M. Schultz, Y.-M. Hung, A. D. Kent, and L. Klein. Towards a six-state magnetic memory element. *Applied Physics Letters*, 108(182401), 2016.
- [84] A. Fraile Rodríguez, L. J. Heyderman, and F. Nolting. Permalloy thin films exchange coupled to arrays of cobalt islands. *Applied Physics Letters*, 89(142508), 2006.
- [85] A. Bollero, L. D. Buda-Prejbeanu, V. Baltz, J. Sort, B. Rodmacq, and B. Dieny. Magnetic behavior of systems composed of coupled ferromagnetic bilayers with distinct anisotropy directions. *Physical Review B*, 73(144407), 2006.
- [86] J. Sort, A. Popa, B. Rodmacq, and B. Dieny. Exchange-bias properties in permalloy deposited onto a Pt / Co multilayer. *Physical Review B*, 70(174431), 2004.
- [87] D. Litvinov, R. M. Chomko, L. Abelman, K. Ramstöck, G. Chen, and S. Khizroev. Micromagnetics of a Soft Underlayer. *IEEE Transactions on Magnetics*, 36(5), 2000.
- [88] J. van Ek, A. Shukh, E. Murdock, G. Parker, and S. Batra. Micromagnetic perpendicular recording model: soft magnetic underlayer and skew effect. *Journal of Magnetism and Magnetic Materials*, 235(1-3), 2001.
- [89] D. Litvinov, M. H. Kryder, and S. Khizroev. Recording physics of perpendicular media: soft underlayers. *Journal of Magnetism and Magnetic Materials*, 232(1-2), 2001.
- [90] A. Vansteenkiste, J. Leliaert, M. Dvornik, M. Helsen, F. Garcia-Sanchez, and B. Van Waeyenberge. The design and verification of mumax3. *AIP Advances*, 4(10), 2014.

- [91] A. A. Zhukov, A. V. Goncharov, P. A. J. de Groot, M. A. Ghanem, P. N. Bartlett, R. Boardman, H. Fangohr, V. Novosad, and G. Karapetrov. Oscillatory thickness dependence of the coercive field in magnetic three-dimensional antidot arrays. *Applied Physics Letters*, 88(062511), 2006.
- [92] M. Zheng, L. Menon, H. Zeng, Y. Liu, S. Bandyopadhyay, R. D. Kirby, and D. J. Sellmyer. Magnetic properties of Ni nanowires in self-assembled arrays. *Physical Review B*, 62(18), 2000.
- [93] K. Nielsch, R. B. Wehrspohn, J. Barthel, J. Kirschner, U. Gösele, S. F. Fischer, and H. Kronmüller. Hexagonally ordered 100 nm period nickel nanowire arrays. *Applied Physics Letters*, 79(1360), 2001.
- [94] H. Pan, B. Liu, J. Yi, C. Poh, S. Lim, J. Ding, Y. Feng, C. H. A. Huan, and J. Lin. Growth of single-crystalline ni and co nanowires via electrochemical deposition and their magnetic properties. *The Journal of Physical Chemistry B*, 109(8), 2005.
- [95] T. O. Ely, C. Amiens, B. Chaudret, E. Snoeck, M. Verelst, M. Respaud, and J.-M. Broto. Synthesis of Nickel Nanoparticles. Influence of Aggregation Induced by Modification of Poly(vinylpyrrolidone) Chain Length on Their Magnetic Properties. *Chemistry of Materials*, 11(3), 1999.
- [96] Q. Chen and Z. J. Zhang. Size-dependent superparamagnetic properties of mgfe₂o₄ spinel ferrite nanocrystallites. *Applied Physics Letters*, 73(3156), 1998.
- [97] I. N. Krivorotov, H. Yan, E. D. Dahlberg, and A. Stein. Exchange bias in macroporous Co/CoO. *Journal of Magnetism and Magnetic Materials*, 226 - 230(2), 2001.
- [98] J. Nogues and I. K. Schuller. Exchange bias. *Journal of Magnetism and Magnetic Materials*, 192, 1999.
- [99] Aaron C. Johnston-Peck, Junwei Wang, and Joseph B. Tracy. Synthesis and structural and magnetic characterization of ni(core)/nio(shell) nanoparticles. *ACS Nano*, 3(5), 2009.
- [100] X. Liu, M. Bauer, H. Bertagnolli, E. Roduner, J. van Slageren, and F. Phillipp. Structure and Magnetization of Small Monodisperse Platinum Clusters. *Physical Review Letters*, 97(253401), 2006.
- [101] R. Litrán, B. Sampedro, T. C. Rojas, M. Multigner, J. C. Sánchez-López, P. Crespo, C. López-Cartes, M. A. García, A. Hernando, and A. Fernández. Magnetic and microstructural analysis of palladium nanoparticles with different capping systems. *Physical Review B*, 73(054404), 2006.

- [102] M. Sawicki, D. Chiba, A. Korbecka, Y. Nishitani, J. A. Majewski, F. Matsukura, T. Dietl, and H. Ohno. Experimental probing of the interplay between ferromagnetism and localization in (Ga , Mn)As. *Nature Physics*, 6:22–25, 2009.

Vita

Susan Elizabeth Kempinger

Education:

B.S. Physics and Mathematics *University of Nebraska-Lincoln* 2013

Publications:

S. Kempinger, R. Terry, A. Bowers, S. Abedi, R. D. Fraleigh, and N. Samarth. “Mesoscopic size influence on domain wall motion in patterned perpendicular anisotropy magnetic films,” (*in prep*, 2019)

S. Kempinger, R. D. Fraleigh, P. E. Lammert, S. Zhang, V. H. Crespi, P. Schiffer, and N. Samarth. “Imaging the stochastic microstructure and dynamic development of correlations in perpendicular artificial spin ice,” arXiv:1904.06625 (2019)

S. H. Lee, Y. Zhu, Y. Wang, L. Miao, T. Pillsbury, **S. Kempinger**, D. Graf, N. Alem, C. -Z. Chang, N. Samarth, and Z. Mao. “Spin scattering and noncollinear spin structure-induced intrinsic anomalous Hall effect in antiferromagnetic topological insulator MnBi_2Te_4 ,” arXiv:1812.00339 (2018)

Y. Liu, **S. Kempinger**, R. He, T. D. Day, P. Moradifar, S.-Y. Yu, J. L. Russell, V. M. Torres, P. Xu, T. E. Mallouk, S. E. Mohny, N. Alem, N. Samarth, and J. V. Badding. “Confined Chemical Fluid Deposition of Ferromagnetic Metalattices,” *Nano Lett.* **18** 1 (2018)

R. D. Fraleigh, **S. Kempinger**, P. E. Lammert, S. Zhang, V. H. Crespi, P. Schiffer, and N. Samarth. “Characterization of switching field distributions in Ising-like magnetic arrays,” *Phys. Rev. B.* **95** 144416 (2017)

E. O. Lachman, A. F. Young, A. Richardella, J. Cuppens, H. R. Naren, Y. Anahory, A. Y. Meltzer, A. Kandala, **S. Kempinger**, Y. Myasoedov, M. E. Huber, N. Samarth, and E. Zeldov. “Visualization of superparamagnetic dynamics in magnetic topological insulators,” *Science Advances* **1** 1500740 (2015)

A. Kandala, A. Richardella, **S. Kempinger**, C.-X. Liu, and N. Samarth. “Giant anisotropic magnetoresistance in a quantum anomalous Hall insulator,” *Nat. Comm.* **6** 7434 (2015)